SOLID AND LIQUID OXYGEN UNDER HIGH MAGNETIC FIELD

by

Chiaki UYEDA

DISSERTATION IN PHYSICS

THE OSAKA UNIVERSITY

GRADUATE SCHOOL OF SCIENCE

TOYONAKA, OSAKA

SOLID AND LIQUID OXYGEN
UNDER
HIGH MAGNETIC FIELD

by

CHIAKI UYEDA

DISSERTATION IN PHYSICS

OSAKA UNIVERSITY
GRADUATE SCHOOL OF SCIENCE
TOYONAKA, OSAKA

CONTENTS

ABSTRACT

A systematic study of liquid and solid oxygens under high magnetic field is presented. High field magnetizations of three magnetic phases, α, β and γ in solid oxygen are measured in the pulsed high field up to 500kOe. The spin flop field and high field susceptibility of the α-phase are obtained and various magnetic parameters of the antiferromagnetic α-phase are determined. The α-phase is a two dimensional antiferromagnet with intrinsic Néel temperature of 30K. However, the structual phase transition occurs at 23.9K and the β-phase appears above this temperature. The β-phase consists of triangular spin short range order while the one dimentional short range order exists in the A-15 type of γ-phase which appears above 42.4K. The intermolecular exchange interaction J(r) is quantitatively evaluated as a function of the molecular distance r. The possibility of magnetically induced martensitic phase transition at the α- and β-phase boundary is discussed.

The liquid oxygen is systematically studied in the high magnetic field and two new phenomena are found. One of them is a large magneto-volume effect and another is the field-induced transparency effect. It turns out that the volume of liquid O_2 increases under external magnetic field with the volume expantion $\Delta V/V_0$ of 2.2×10^{-4} under the field of 80kOe. The effect is understood by the exchange repulsion between O_2 spins polarized by an external magnetic field.

The field-induced transparency is described in the following way. The blue color of liquid O_2 due to the bimolecular transition $2(^3\Sigma_g^-) - 2(^1\Delta_g)$, is reduced under high magnetic field.

It is noted that the total spin angular momentum should be conserved during the transition. As the state $^1\Delta_g$ has no spin angular momentum, spins of ground state molecules should be antiparallel from each other. In a strong magnetic field, however, most spins are parallel so that the transition becomes impossible. The experimental results are explained quantitatively by taking the contribution of the intermolecular exchange interaction J(r) and the magneto-volume effect into account. The results indicate that the dominant exchange effect responsible to the transition is the antiferromagnetic exchange coupling between two molecules rather than the average mean molecular field in liquid.

§1. INTRODUCTION

The study of oxygen molecule O_2 is one of the most basic subject in many fields of natural sciences. The ground state of O_2 is $^3\Sigma_g^-$ with spin S=1 and it also has become a fundamental element in the field of modern magnetism. In 1895, P.Curie showed that all materials can be magnetically classified into three types, namely ferromagnetic, diamagnetic and paramagnetic materials[1]. In this classifica ion, oxygen gas was introduced as a typical example of paramagnetic material. The so-called Curie law was also found by measuring the temperature dependence of the magnetic susceptibility of O_2 gas. In 1914, H.Kammerlingh Onnes measured the magnetic susceptibility of the liquid (90.2K>T>54.4K) and solid phase (54.4K>T)[2]. It became clear that the liquid phase shows paramagnetic temperature dependence, whereas the solid phase shows considerable deviation from the Curie-Weiss law. At that time, there was yet no idea of the antiferromagnetic long range order and this drop of susceptibility was explained by assuming the presence of a diamagnetic $(O_2)_2$ in the solid phase[3]. Afterwards, however, this dimer model turned out to be inadequate because the chemical binding energy of $(O_2)_2$ was found to be higher than that of the isolated atomic state.

In 1954, E.Kanda, T.Haseda and A.Otsubo carried out a systematic measurement on the magnetic susceptibility of polycrystalline solid O_2[4]. They found three crystallographic modifications under normal pressure called as α-(T<23.9K), β-(23.9K<T<42.4K) and γ- phase (42.4K< T<54.4K). It became

clear that the γ-phase shows a paramagnetic like temperature dependence while the susceptibilities of α- and β- phases increase with temperature and the possibility of the antiferromagnetic ordering was discussed. In 1981, DeFotis remeasured the susceptibilities of the three phases precisely and found a discontinuous drop of susceptibility at liquid-solid boundary.[5]

The crystallographic analysis was done by X-ray diffraction and the structures of the three phases are now well known[6-8]. The neutron diffraction study reveals that the α-phase is antiferromagnetic whereas no long range order is found in the β- and γ-phases[8),9)].

The antiferromagnetism of the α-phase is investigated by the antiferromagnetic resonance (AFMR) study[10,11]. The results show two resonance modes in the zero magnetic field reflecting the orthorhombic symmetry in the anisotropy energy. However, the whole nature of the magnetic properties is not so clear so far because the single crystal is difficult to obtain due to the structual phase transformations. Moreover, many data are scattered and no consistent picture has been obtained for the magnetic properties so far[5)].

Recently, magnetization of solid oxygen under extreme conditions were investigated by Meier et al.[12)] using high pressure and high magnetic field. One of their discoveries is an anomalous peak in the differential magnetization dM/dH in the α-phase at 4.2K. However, they could not find the correct value of the spin flop field H_c because of the lack of exact theory to evaluate H_c from the powder susceptibility.

The high field magnetism of solid oxygen is extended in the present paper using precise pulsed magnetic field at Osaka University up to 500kOe[13]. Pulsed high field measurement is effective to polycrystalline antiferromagnetic materials by two reasons. First of all, $\chi_\perp$ of a single crystal is measured directly from the high field susceptibility. This means that the value of J is obtained directly from high field magnetization data of a polycrystalline sample. The second point is that the peak in the dM/dH curve is substantially observed at H_c regardless of the anisotropy constant ratio K_2/K_1, so the H_c value is obtained much more precisely than the static measurements[14]. Details are discussed in section 4.

The obtained results give an important key to show the two dimentionality of the α-phase. Magnetism in the β- and γ-phases are then successively solved by connecting our results with previously published data as will be seen in section 5.

The volume expantion of O_2 liquid under magnetic field is investigated[15]. A large magneto-volume effect is found and it is explained by the antiferromagnetic repulsive force between the polarized spins under magnetic field. The volume change of liquid O_2 under external magnetic field is measured in the static field and the volume increase ratio of $\Delta V(H_0)/V_0=0.02\%$ was observed at 80kOe. The optical property of the liquid phase is systematically studied using the pulsed high magnetic field, and the field-induced transparency is found[16]. In 1964, V.I.Dianov-Klokov measured the pressure dependence of visible absorption coefficient at λ_0=6290A and λ_1= 5760A[17], which are the cause of the light blue color in liquid oxygen. He proved

that the color is due to the bimolecular transition $2(^3\Sigma_g^-)$-$2(^1\Delta_g)$. In the present work, it is found that the absorption coefficient of the blue color of the liquid is reduced with increasing the external magnetic field H_0. The quantitative field dependence of $\alpha(H_0)$ is calculated by considering the intermolecular exchange interaction between O_2 pair in liquid.[18]

It is noted that the mean field exchange model is not applicable to this case because the optical absorption occurs by the two-molecular interaction so that the mean field for an oxygen molecule does not have an important role for the optical process.

§2. REVIEW OF OXYGEN

(a) Electronic Energy State and Absorption Spectra of O_2 Molecule

O_2 is an exceptional paramagnetic molecule among the class of homonuclear diatomic molecules, such as H_2,N_2,O_2,F_2,Cl_2 and I_2. This paramagnetic property originates from the electronic ground state. According to LCAO-MO theory, the molecular orbital of O_2 is composed of two atomic $(1S)^2(2S)^2(2P)^4$ as is shown in Fig.1. The atomic orbital pairs of (1s),(2s),($2p_x$),($2p_y$)and ($2p_z$) from five sets of bonding and anti-bonding molecular orbitals. The orbitals with and without * stands for anti-bonding and bonding orbitals, respectively. The 16 electrons of O_2 molecule occupy these levels as follows. The atomic (1s),(2s) and ($2p_x$) orbital pairs form three sets of bonding and anti-bonding σ-orbitals, namely $\sigma 1s, \sigma^* 1s, \sigma 2s, \sigma^* 2s$ and $\pi_x 2p, \pi^*_x 2p$. The energy levels of these orbitals are shown schematicaly in Fig.1. 10 electrons fill the $\sigma 1s, \sigma^* 1s, \sigma 2s, \sigma^* 2s$ and $\sigma 2p_x$ orbitals. The atomic ($2p_y$) and ($2p_z$) orbital pairs form two sets of bonding and anti-bonding π-orbitals, namely $\pi_y 2p, \pi^*_y 2p$ and $\pi_z 2p, \pi_z^* 2p$, respectively. It is noted that $\pi_y 2p$ and $\pi_z 2p$ states degenerate and four electrons fill these states. The residual two electrons occupy the degenerated levels of anti-bonding $\pi_y^* 2p$ and $\pi_z^* 2p$ orbitals. Considering the Coulomb repulsion, two electrons are most stable when their spins are aligned parallel to each other, according to the Hund's rule. Thus the ground state of O_2 molecule will be S=1 and L=0 ($^3\Sigma_g^-$), and the magnetic moment is $2\mu_B$ per molecule[19]. The

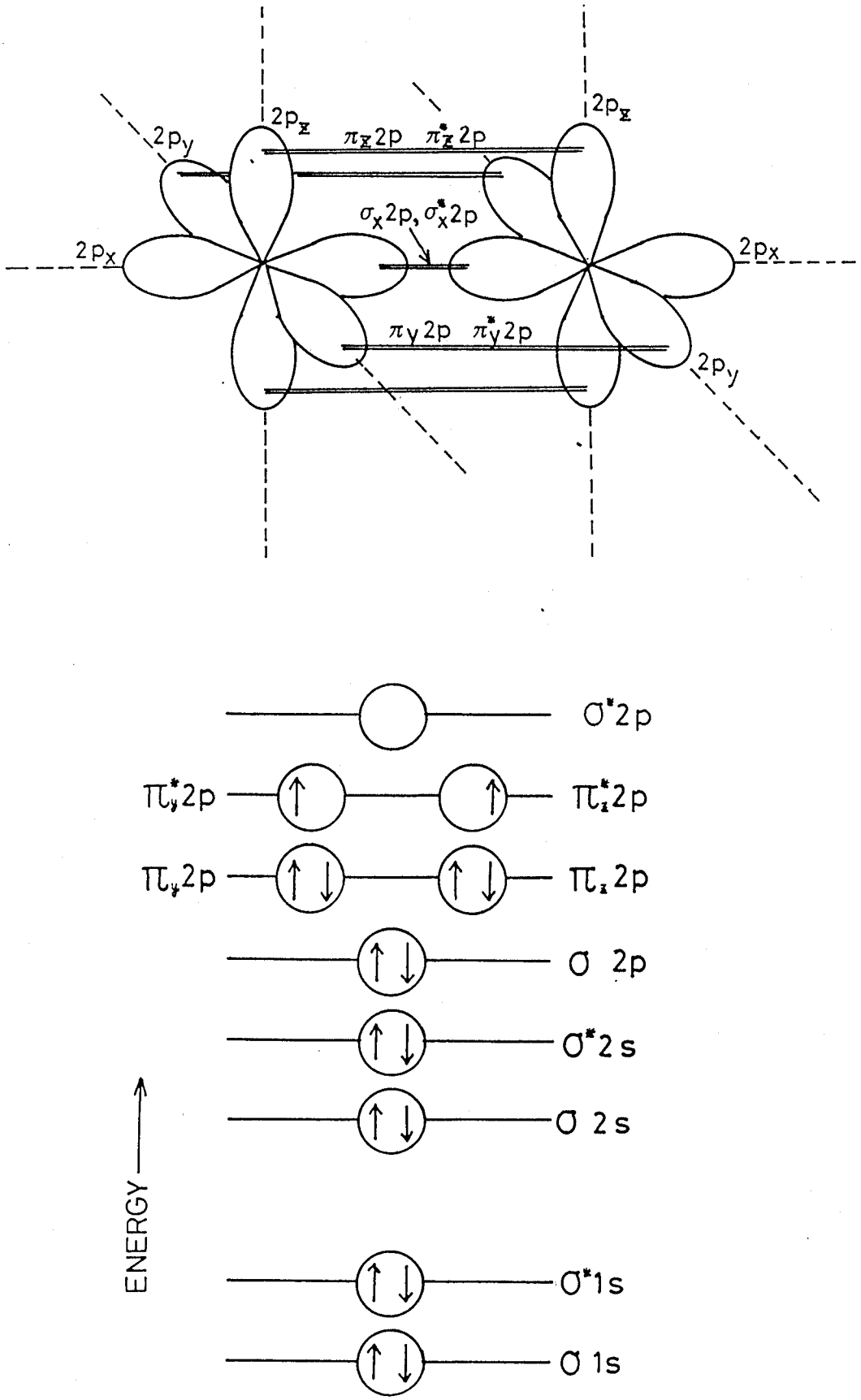

Fig.1 Schematic view of molecular orbitals in O_2 molecule.

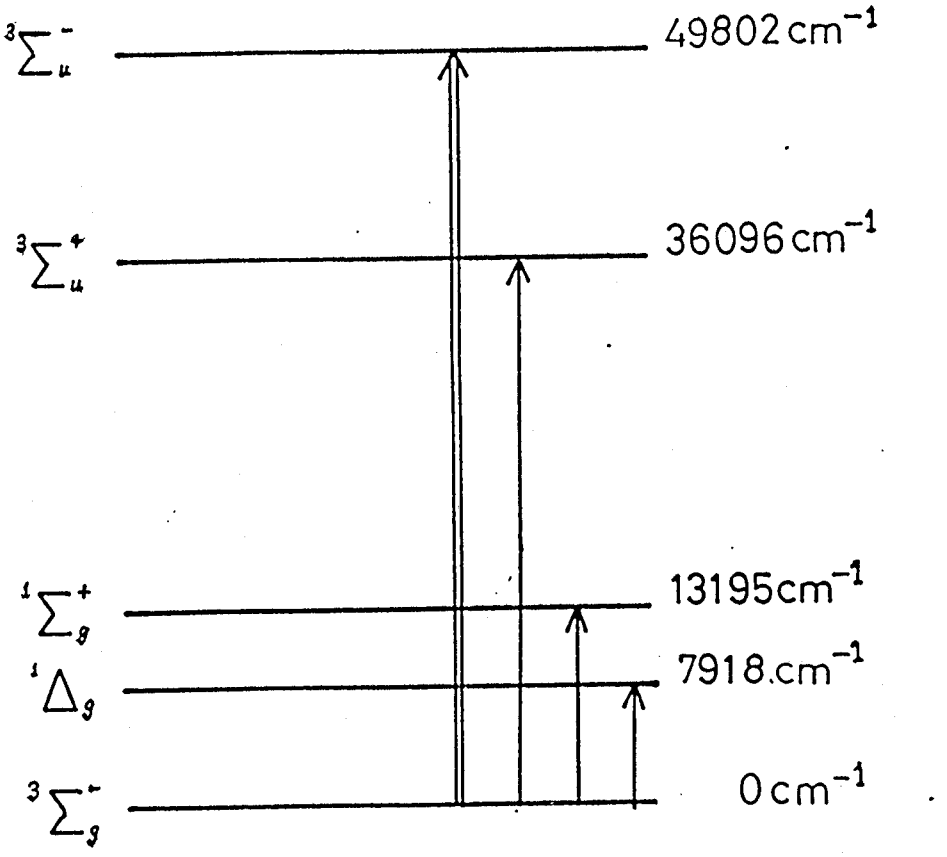

Fig.2 Energy levels of O_2 molecules. Broad line and fine line denote the quantum machanically allowed and forbidden transitions, respectively.

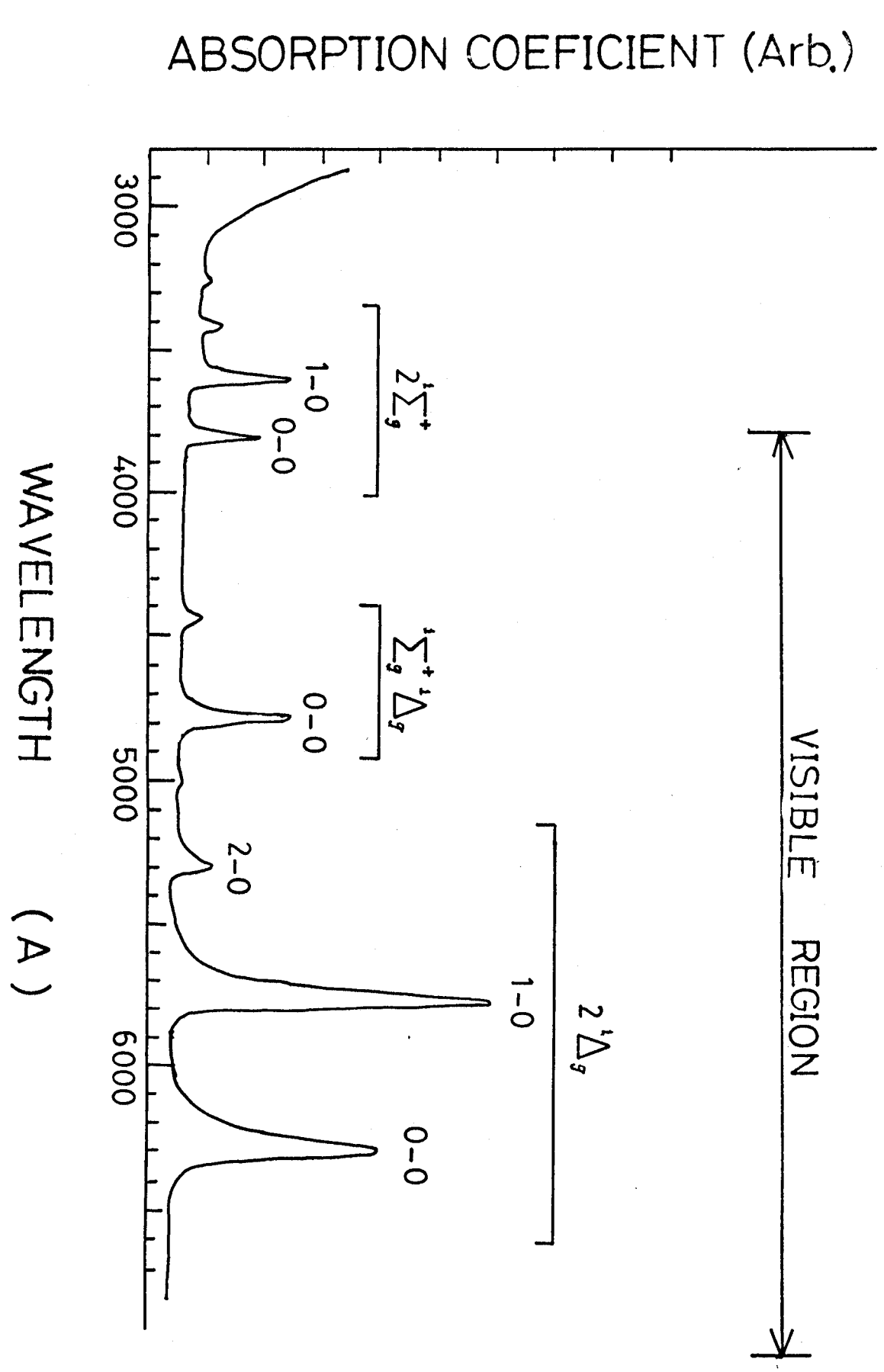

Fig.3. Absorption spectrum of O_2 molecule in the visible to ultra-violet region.

wave function of anti-bonding πy^*2p and πz^*2p orbitals extend outside and there is a direct antiferromagnetic exchange interaction between neighbouring molecular spins.

The first excited state of O_2 is $^1\Delta_g$ (S=0, L=2) which is separated 7918cm^{-1} from the ground state. The transition $^3\Sigma_g^-$ to the first, second and third excited levels are forbidden. Relatively weak absorption spectra due to these transitions are observed in the infra-red rigion. The first allowed transition is $^3\Sigma_g^- \rightarrow {}^3\Sigma_u^-$, which causes a very strong and broad absorption spectrum. The spectrum is vital to life on earth, because the peak wave length is around 1400A and hence cuts off the ultra-violet light from the sun which cause distructive effect on living creatures.

The absorption spectra observed in the 3000-6500A resions are due to one-photon-two-molecular transition, where two ground state molecules are excited to the upper levels by a absorption of a single photon. Absorption spectra due to transitions such as $2(^3\Sigma_g^-) \rightarrow 2(^1\Delta_g)$, $2(^3\Sigma_g^-) \rightarrow (^1\Sigma_g^+)(^1\Delta_g)$ and $2(^3\Sigma_g^-) \rightarrow 2(^1\Sigma_g^+)$ are observed as is seen in Fig.3. These spectra have fine structures due to the excitations of vibrational quantum number n. The absorption line noted as "1-0" in Fig.3 , for example, means that n changed from 0 to 1 in one of the paired molecules. It is obvious from Fig.3 that the visible resion of O_2 absorption spectrum overlaps with the $2(^3\Sigma_g^-) \longrightarrow 2(^1\Delta_g)$ absorption spectra. Particulaly, the 0-0 line and the 1-0 line has a relatively strong and broad peak at 6290A and 5760A, respectively. This is the reason why liquid oxygen visualy show a light blue color. It is quite satisfactory that the

absorption of these spectra are due two one-photon-two-molecular process because the wavelength of the spectrum correspond to the sum of energy separation of the two molecules . Diahov-Kovokov[17] examined this fact by showing that the absorption co-efficient of $2(^3\Sigma_g^-) \rightarrow 2(^1\Delta_g)$ spectrum is propotional to the square of the gas pressure of O_2..

(b) Crystallographic and Magnetic Properties of Solid O_2

Crystal structures of the three phases of solid O_2 are shown in Figs.4-6. Main lattice parameters and important neighboring oxygen distances are shown in these figures.

The high temperature phase, γ-phase is cubic with space group Pm3n and eight oxygen molecules are contained in a unit cell.[6] It is noted that the structure is so-called A-15 type structure which is one of the basic form of the high-Tc superconductors. Two molecules occupying the corner and body-centered positions rotate randomly around the equilibrium position not freely but rather statistically disordered with the average direction of the molecular axis along the cubic threefold axes. Other six O_2 on the cube faces are statistically disordered with molecular axes along two of the three cubic axes so that the statistical form factor is disc-like[20] as is schematically shown in Fig.4. It is noticed that two O_2 molecules in a cube face form a linear chain along the cubic axis. There are three chains corresponding to three cubic axes. As the intrachain molecular distance d_1 is shortest, the linear chain spin correlation will be dominant in this phase. This problem will be discussed later in section 5.

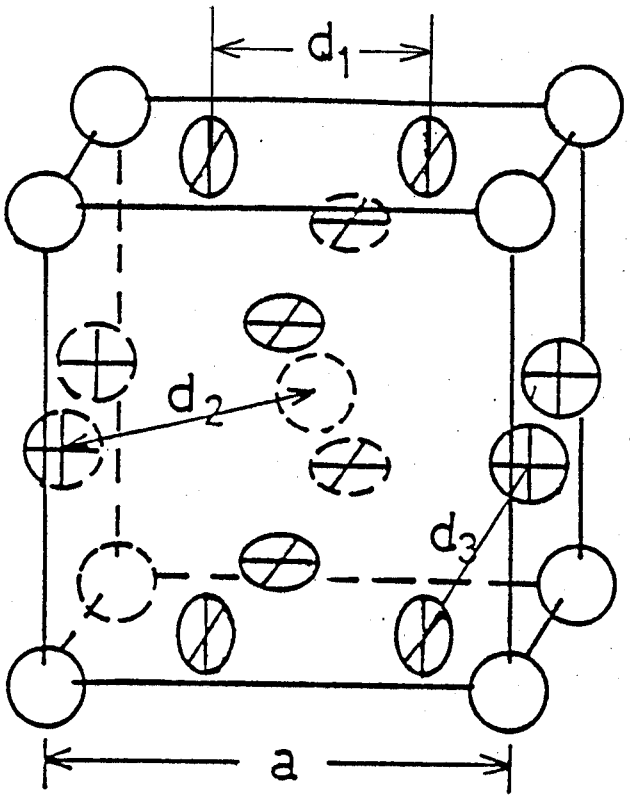

γ-Phase

a = 6.78 A
d_1 = 3.39 A
d_2 = 3.79 A
d_3 = 4.15 A

Fig.4. Crystal structure of γ-phase.

β-Phase

a = 3.30 A

c = 11.26 A

d_4 = 4.21 A

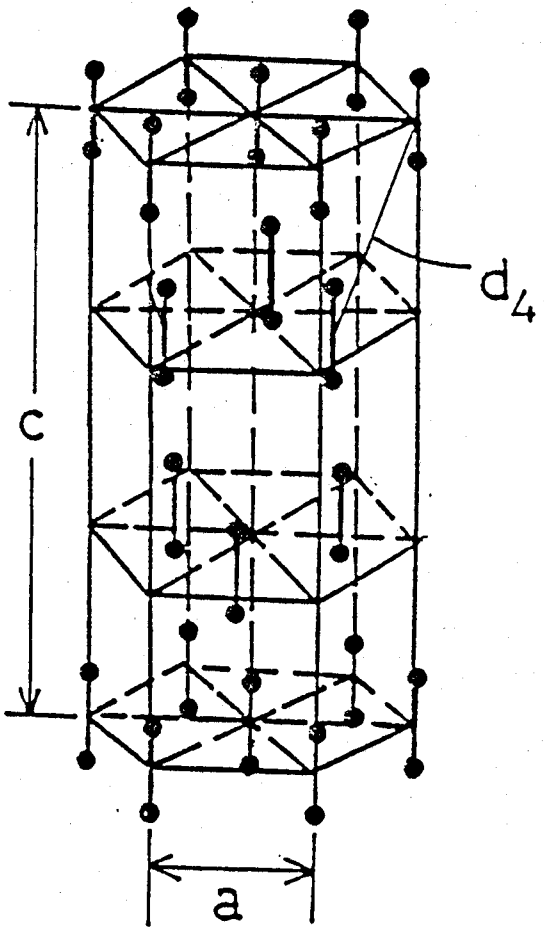

Fig.5. Crystal structure of β-phase.

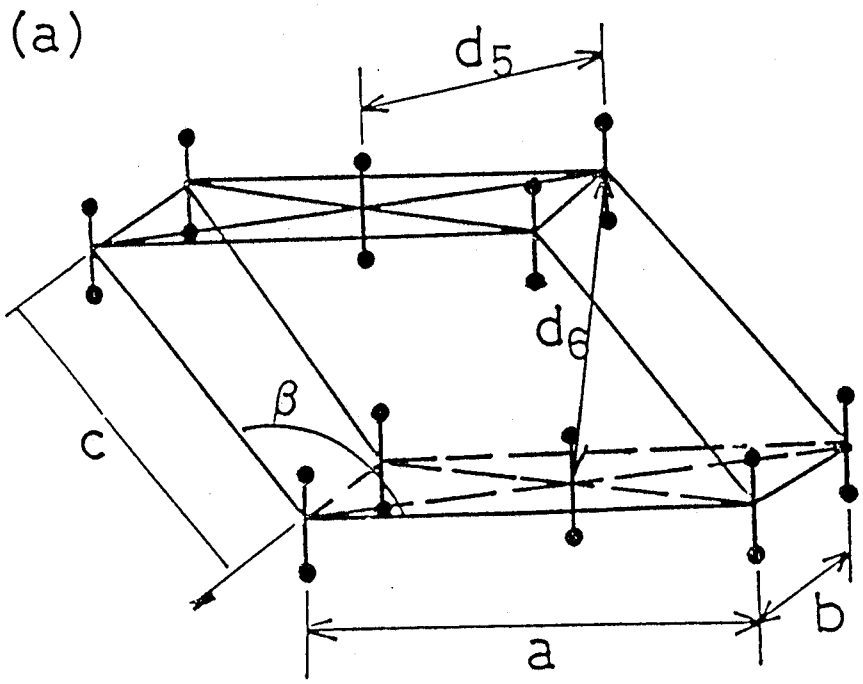

α-Phase

a = 5.40 A
b = 3.43 A
c = 5.09 A
β = 132.5°
d_5 = 3.20 A
d_6 = 4.19 A

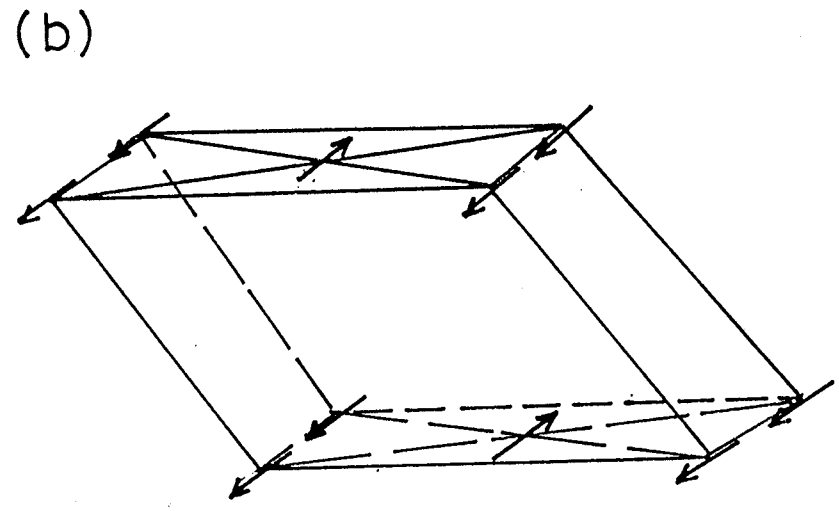

Fig.6. (a) Crystal structure of α-phase. (b) Spin alignment of α-phase.

The β-phase has rhombohedral structure with space group R3m[7] and is given in Fig.5. Black spot pair at the lattice points represents O_2 with average direction. The librational motion around the direction is considerably large . Spin correlations in this phase will be two-dimensional because the intraplane nearest neighbor distance is much smaller than the interplane distance.

The crystal structure of the α-phase is monoclinic with space group C2/m [8] as is shown in Fig.6. The structure of α-phase is obtained from the β-phase by a slight deformation of the hexagonal plane followed by alternating slip of the each plane keeping the volume to be nearly constant. The crystallographic relation between the α- and β-phases is illustrated in Fig.7.

The phase transformation at $T_{\gamma\beta}$ is of the first order with a considerable latent heat. Owing to a large decrease in volume from γ- to β-phases, single crystals in the α- and β-phases are difficult to obtain. The transition at $T_{\alpha\beta}$ is different from that at $T_{\beta\gamma}$. The transition at $T_{\alpha\beta}$ is believed to be martensitic and magnetically induced phase transformation based on the frustrating properties of the triangular lattice.

The neutron diffraction is studied for the three phases and no magnetic ordering is found in the γ-phase. Recently, Meier and Helmholdt[9] did a precise neutron diffraction study in β- and α-phases and suggested that the β-phase spins show the triangular short range order as is expected from the hexagonal plane structure.

The neutron diffraction[9] and ESR studies[10,11] show that

α-phase is a two sublattice antiferromagnet with orthorhombic ansotropic energy. The spin easy axis is the b-axis.

The magnetic susceptibility curves of three solid phases measured by Kammerlingh-Onnes[1], Kanda et al.[4], Defotis[5] and Meier et al.[12] are shown in Fig.8 by white squares, dash dotted line, broad solid line and broken line,respectively. The data measured in the present work is also shown in fine solid line. The data of Defotis and Meier et al. agree well with our data. The data measured by Defotis, which is the most intensive measurement done on the suscepitibility of solid oxygen so far will be used in the folllowing discussion because the data lie in the middle of the deviation range of other data.

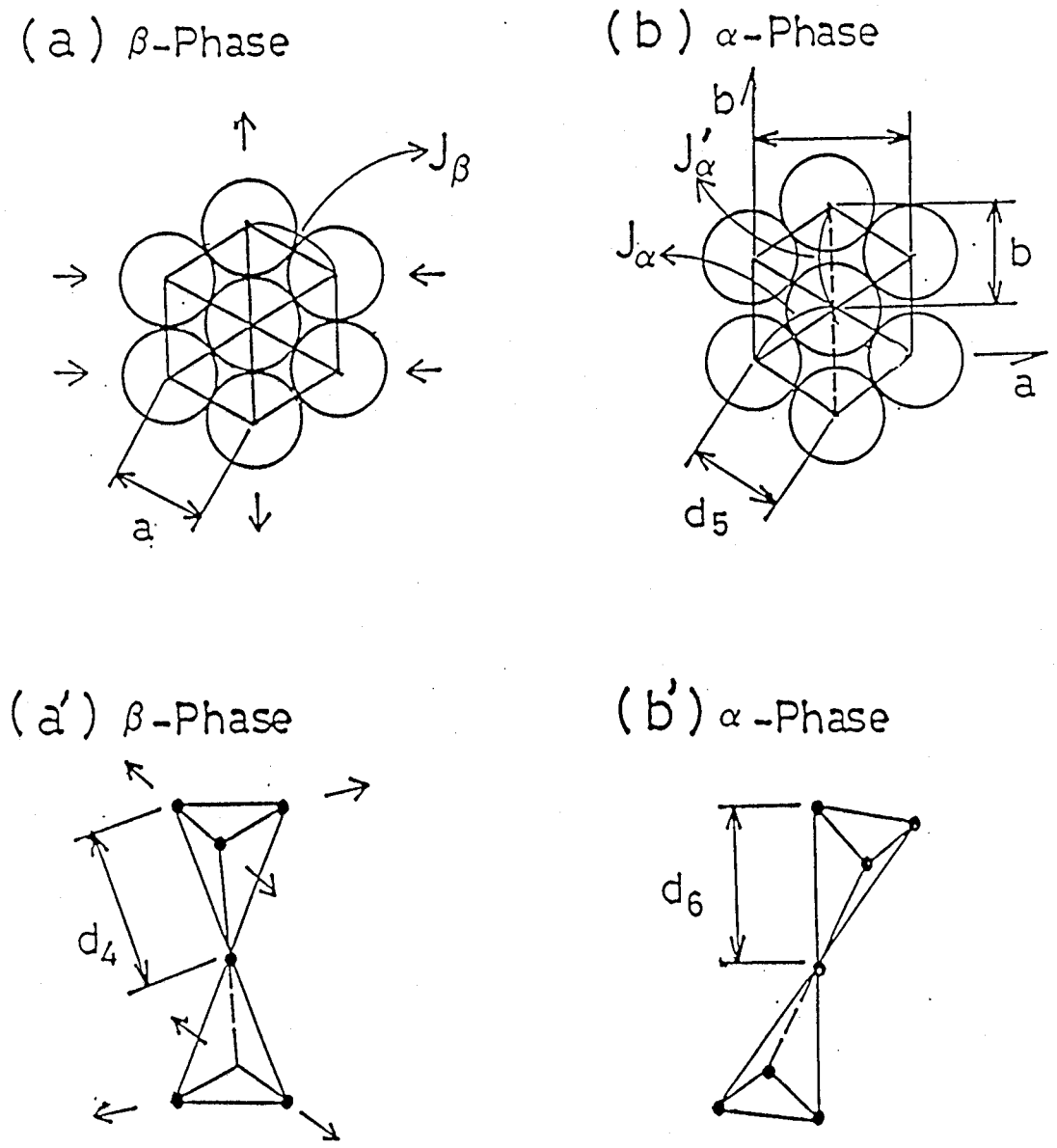

Fig.7. Molecular arrangement in the β- and α-phases. (a) is the hexagonal plane in the β-phase and arrows show directions of the deformation in the α-phase resulting in the structure in (b). Interplane deformation is illustrated in (a') and (b'). J_α, J'_α and J_β are exchange interactions discussed in Section 5.

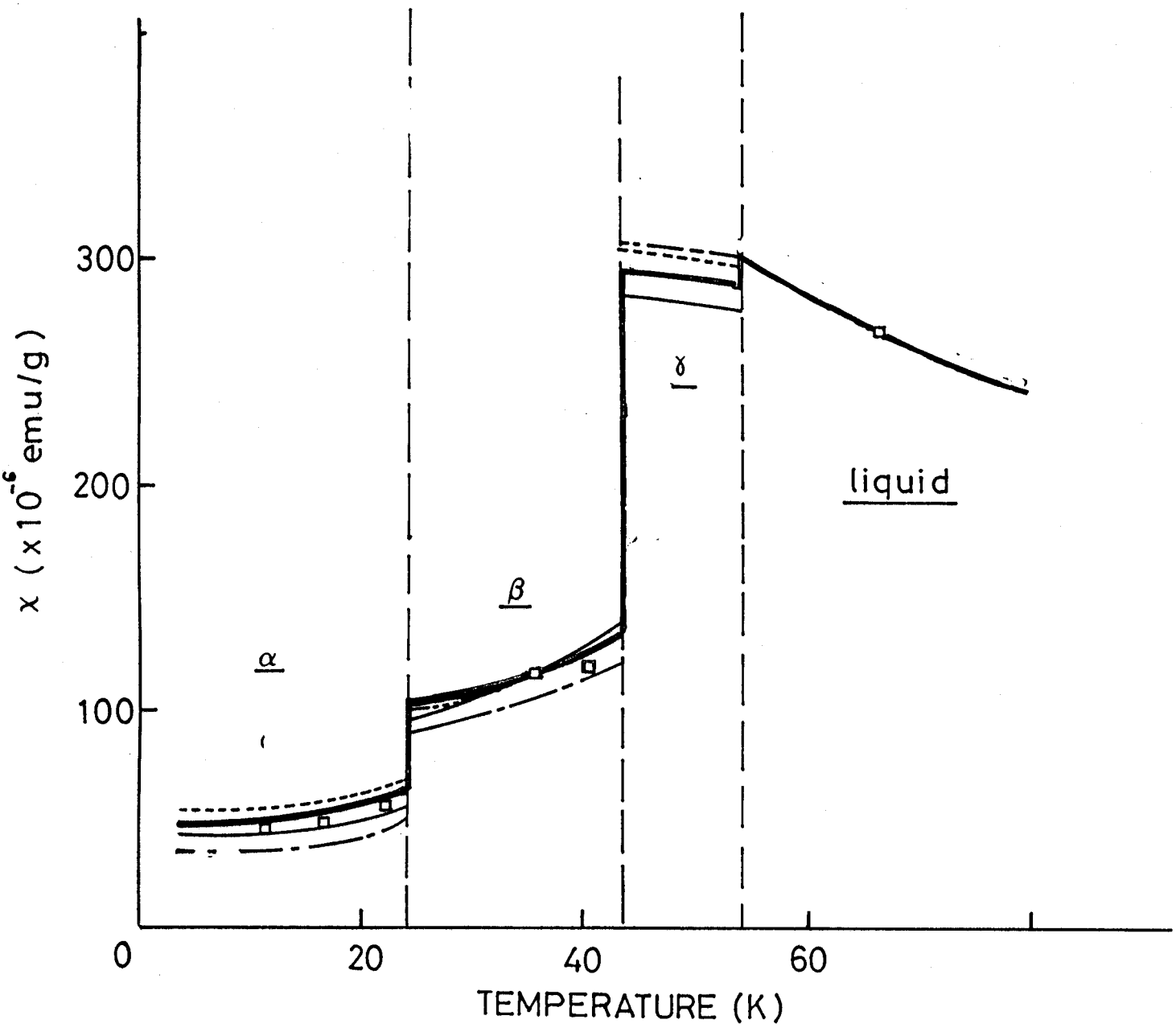

Fig.8 Magnetic susceptibility curves of three solid phases. Data measured by Kammerlingh-Onnes[1], Kanda et al.[4], Defotis[5] and Meier et al.[12] are shown in white squares, dash dotted line, broad solid line and broken line, respectively. The data measured in the present work is also shown in fine solid line.

§3. EXPERIMENTAL PROCEDURE

(a) High Field Magnetization Measurements

High field magnetization measurement was done at High Magnetic Field Laboratory, Osaka University[22]. Two types of magnets were used for the experiment. One of them is the large bore magnet 150(IL)60 with 60mm inner diameter which can produce the field up to 400kOe with the pulse width of 0.4 msec and the field accuracy is 0.3% within about 10cm³. One of the merit for using the large bore magnet is to be able to set a precise temperature control system. Another magnet 150(2L)20 is the standard two-layer magnet up to 700 kOe with 20 mm inner diameter and we used the magnet only at 4.2K when the field more than 400kOe was necessary.

The electrical circuit of the D-2 capitor bank system is shown in Fig.9. Discharge of the capacitor bank is attained by closing a pressurized spark-gap switch G_1. The same type switch G_2 is used as a crowber of diversion switch. Triggering pulse with small amplitude from pulse generators are amplified to trigger the main spark-gap switches G_1 and G_2 with small jitter time by passing through the two of three stages of spark-gap switch systems. In parallel with G_1, a mechanical switch MS is connected which should be operated with the charging voltage of the bank below 4 kV where the spark-gap switch does not operate effectively.

The cross-sectional view of the two-layer magnet 150(2L)20 is shown in Fig.10. The inner-layer coil-a and outer-layer coil-b are made of the maraging steel which is well known as one of the

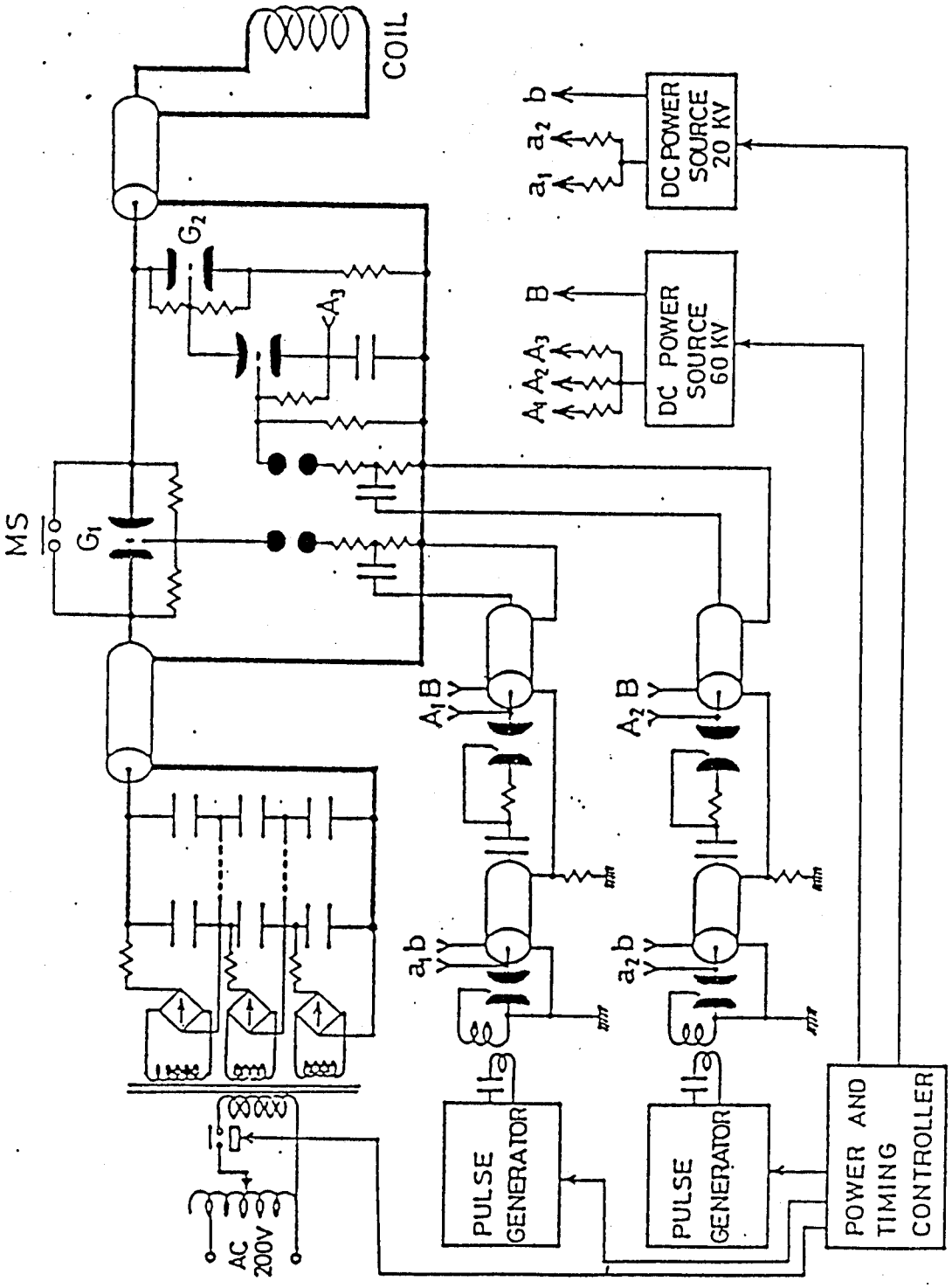

Fig.9 Electric circuit for the D-2 capacitor bank system. G_1 and G_2 are the pressurized air-gap switches and MS is the mechanical switch which is used in the range of low charging voltage (<4 kV). The spark-gap switch G_1 and G_2 work effectively in the voltage range higher than 6 kV.

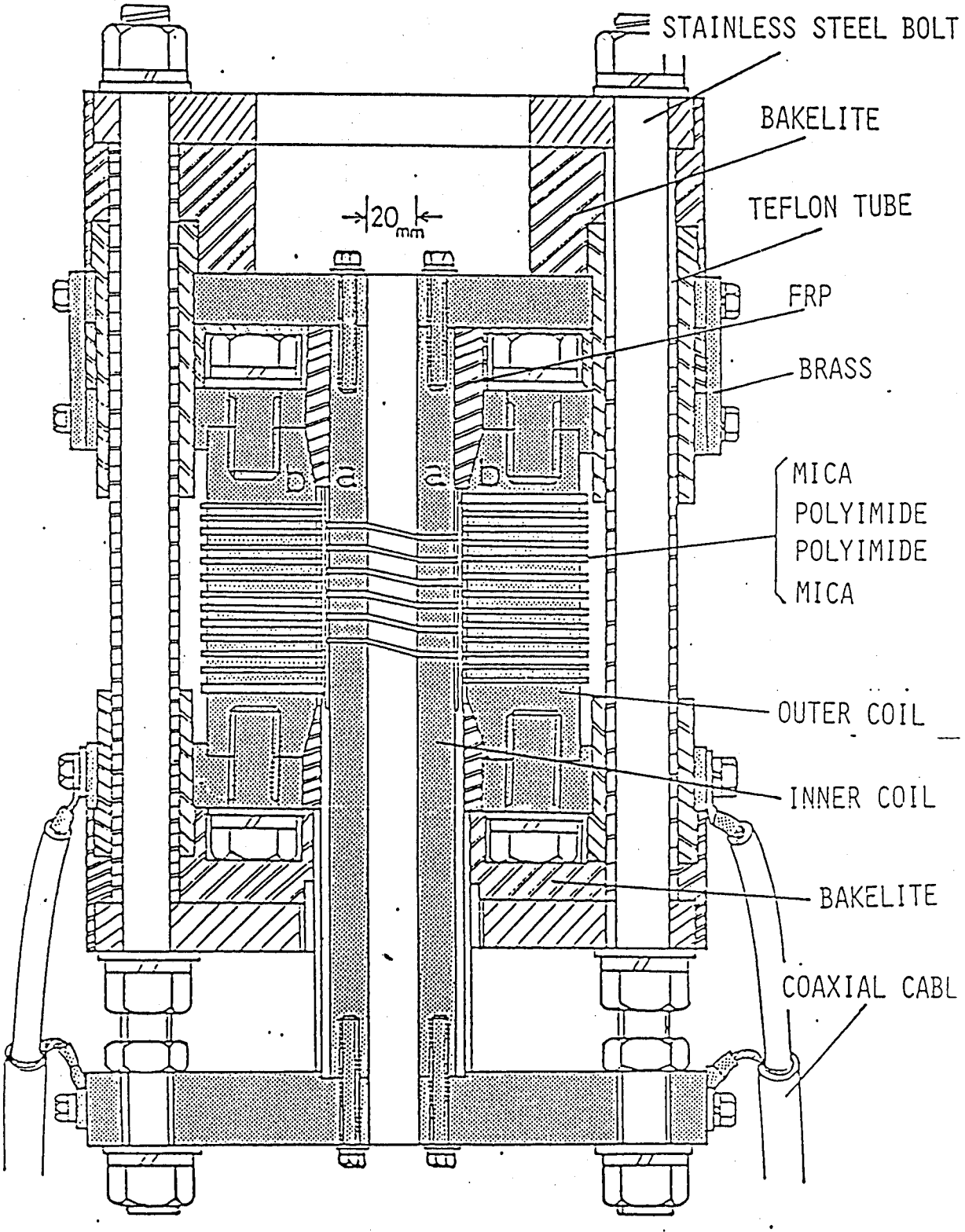

Fig.10 Cross-sectional view of the two-layer magnet.

strongest steel (hardness H_v=700, yield strength>200kg/mm^2). They are connected electrically in series and pulsed current flows through the shadowed area of the magnet. Combination of mica sheets and polyimide laminates are used for the insulation between the windings of the coil. They are strong enough against heat, compressive force and high voltage. Other insulaters used to construct a magnet is shown in the figure. During experiments the magnet is covered with a thick iron hood to avoid unexpected accidents. A dewar with a sample is inserted into the magnet through a hole at the top of the hood. In the case of the D2(1L)60 system, only the outer coil(coil b) is used. Other technical details are similar to the D2(2L)20 system.

The magnetization measurements[23] are done by using a balanced pick-up coil. The technically important point is how to compensate background flux change due to a transient field, which is usually 10^4-10^6 times larger than the flux change due to the magnetization of the specimen. This is usually done by setting three coils as are shown schematically in Fig.11-(a). Coil A picks up the magnetic flux change of the specimen while coil B is wound in the opposite direction to A in order to compensate the background flux change . Fine adjustment is done by one loop coil C taking a bridge balance as is shown in the figure.

Fig.11-(b) is the cut view of the standard pick-up coil which has been used in our laboratory. Considering the field duration and frequency response, coil A is wound with 100 turns. The coil B is coaxially wound on a with 50 turns oppositely. The cross section of coil B is twice as large as that of A so as to

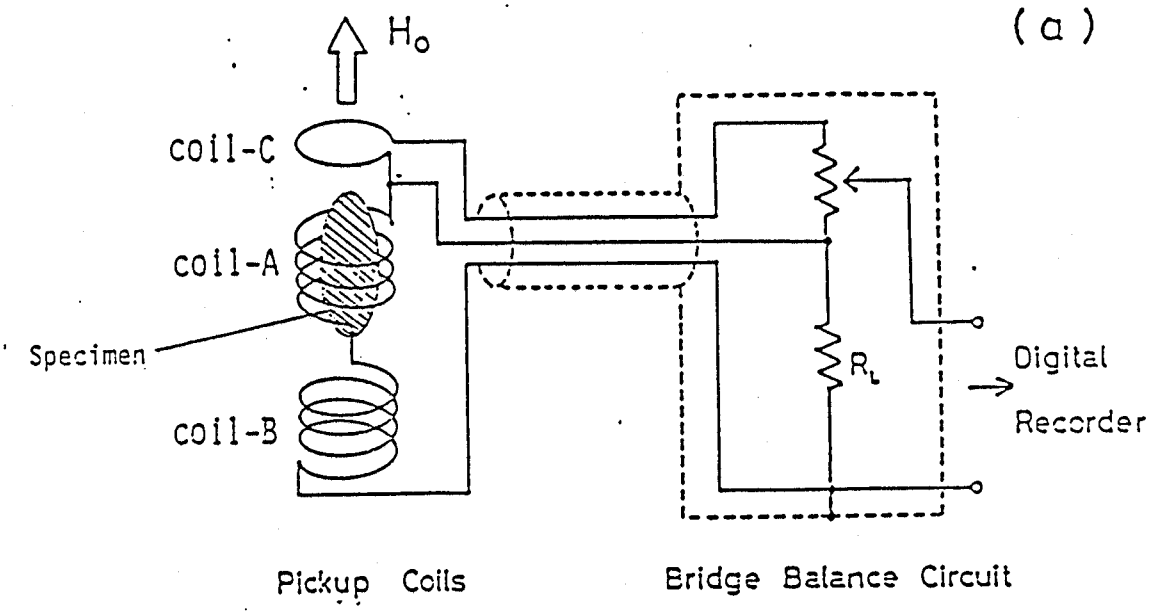

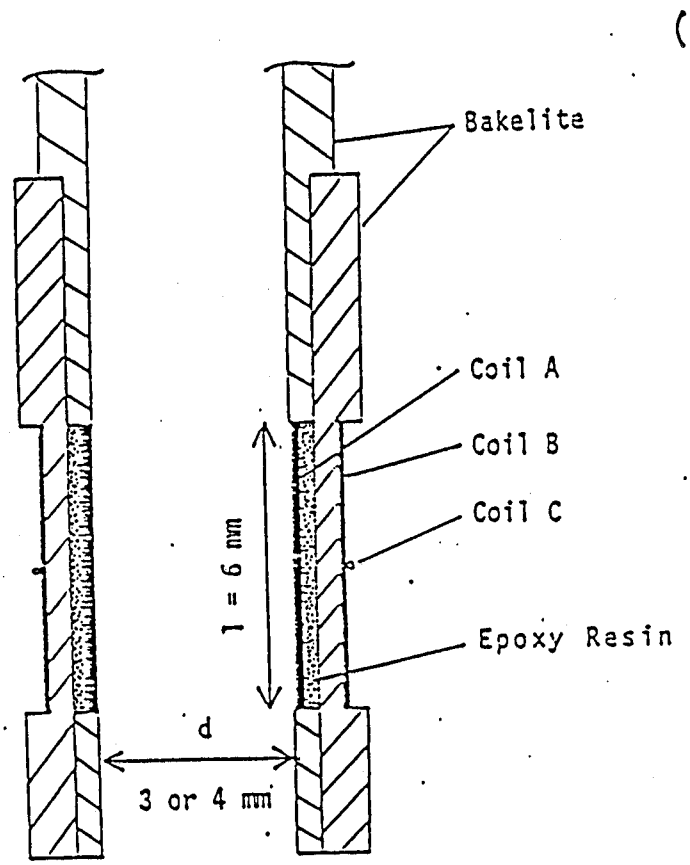

Fig.11 (a): Method of flux compensation. (b): Cut view of standard pick-up coil.

make the net flux in A equal to that in B. Fine adjustment coil C is wound on B. The coil wire material is urethane-coated 2 % tin-doped copper of 0.1 mmD. The wire has large residual resistivity (2.5$\mu\Omega$cm) and is effective to improve the flux compensation especially at liquid helium tempereture. The standard pick-up coil attains a flux compensation of 10^{-4}-10^{-5} at the signal output of the bridge balance circuit.

Fig.12 is a block diagram of the standard measurement system of high field magnetization. Three signal outputs of the pick-up coil (A) are shielded by a copper capillary (B) in the cryostat and are connected to double shield cable (C) and transmitted to the bridge balance circuit. The balnce signal is then stored in a digital recorder (IWATSU, DM-901). Usual measurements are done at the time resolution of 200~500 ns. A magnetic field is monitored by a single loop field pick-up coil (H). The output signal which is proportional to dH/dt is integrated by a high speed operational amplifier and also stored in the digital recorder. The time constant of the integrator is taken as 300 times longer than the field duration time.

The output signal of the bridge balance circuit is proportional to dM/dt but still contains background noise. Further noise reduction is done by Data Processor SM-1330, IWATSU. Using two shots of pulsed field generation, two sets of data with and without the specimen are taken. These are transferred to the Data Processor, where the subtraction of the background and the integration of dM/dt are done. In this manner, sufficiently high sensitive measurement can be done under the final effective flux compensation of 10^{-6}. Practically

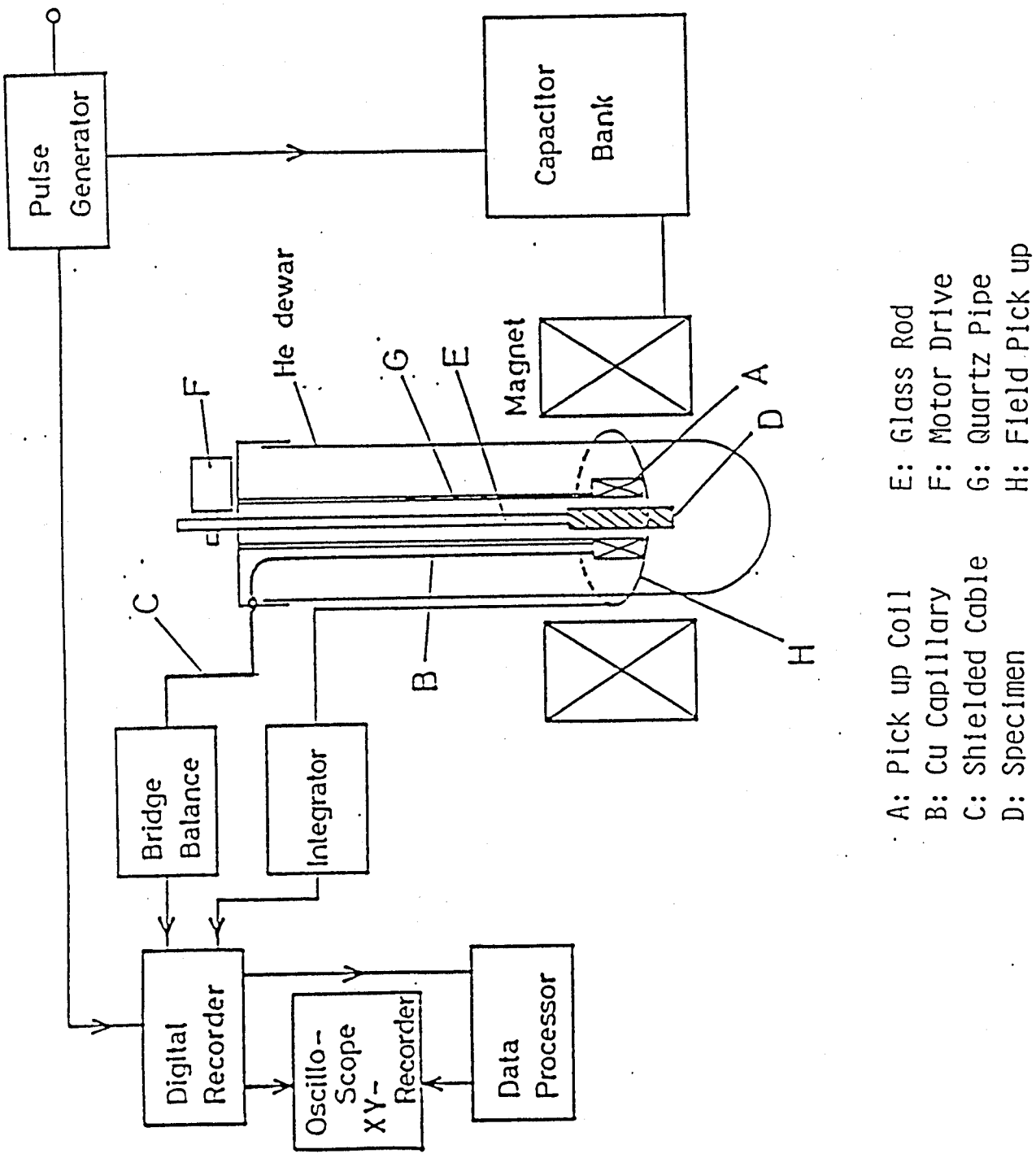

Fig.12 Block diagram of magnetization measurement system.

speaking, this coil can pick up the susceptibility of $5x10^{-6}$emu/cc with S/N~1.

The calibration of magnetization value is done by single crystalline $CuCl_2$ $2H_2O$ or MnF_2 as the standard specimen. An integrated output signal is proportional to a magnetization, cross sectional area and demagnetization correction factor of a specimen. Magnetization value is determind by comparing these values with those of the standard specimen.

A schematic view of the experimental set up added to Fig.12 for solid O_2 measurements is shown in Fig.13. Solid oxygen is condensed at the bottem of the Pyrex tube with an inner diameter of 2.7±0.2 mm by the standard way as is shown in the figure. The sample and the pick-up coil are located in the sample holder cell. Oxygen gas with 99.9% purity is liquified with automatic temperature control system[24]. The temperature control system is also effective to keep the sample temperature constant during the magnetization measurements.

(b) High-Field Optical Absorption Measurements

The measurement of the field induced transparency effect was done by observing the magnetic field dependence of the light absorption in liqid oxygen at the High Magnetic Field Laboratory, Osaka University[22]. Two kinds of experiments are done. In one experiment, monochromatic He-Ne laser was used as light source. This measurement was done in order to obtain a quantitative ratio of the reduction of absorption coefficient $\alpha(Ho)/\alpha(0)$[16]. In another experiment, the whole view of the field dependent absorption spectra is observed by using the optical multichannel analyzer (OMA) with flash lamp[25].

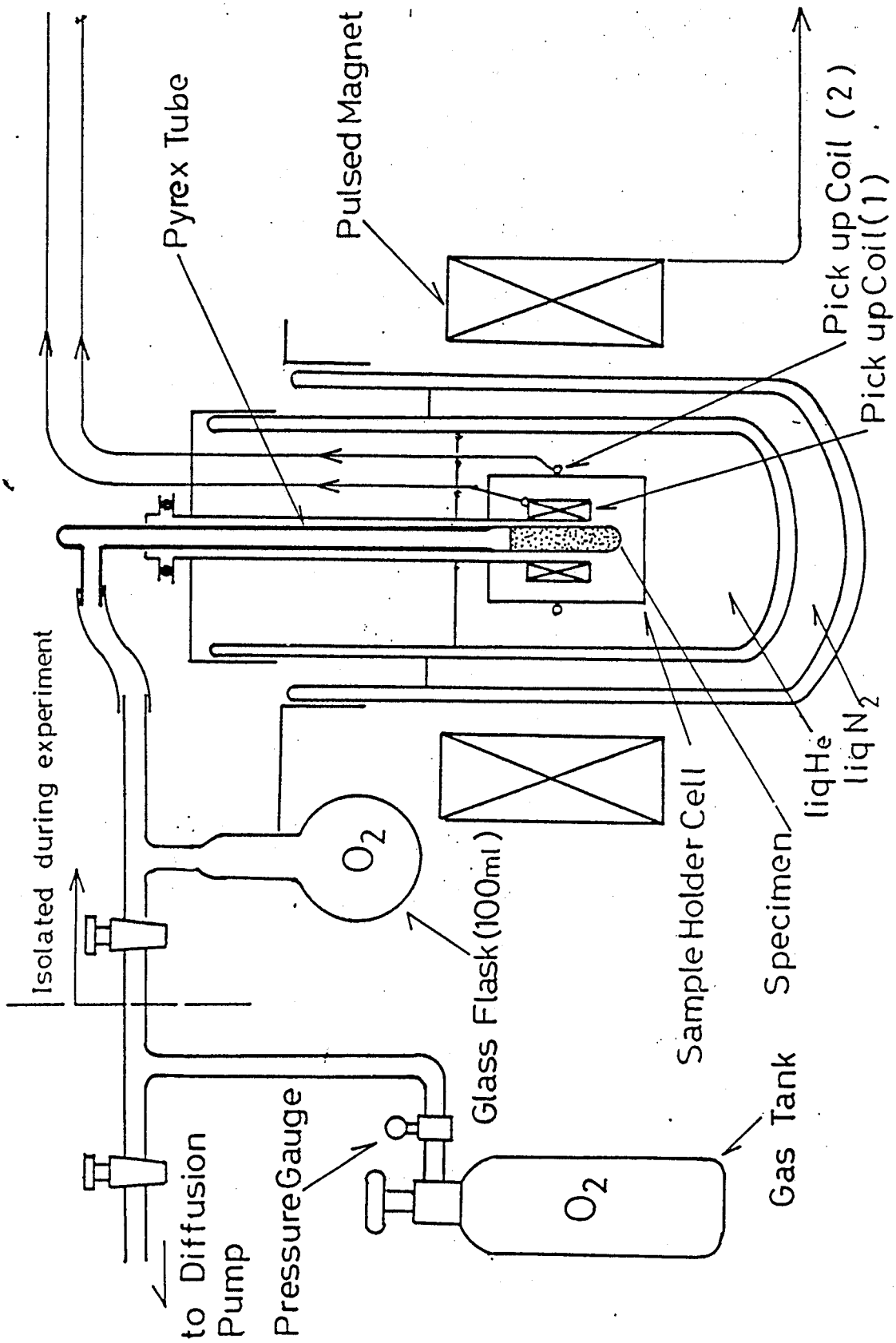

Fig.13. Schematic view of the magnetization measuring system of liquid and solid oxygen.

(b)-1 Measurements Using He-Ne Laser Light

The schematic view of the experimental set-up is shown in Fig.14. He-Ne laser with the wave length of 6328A is used as the light source because the energy is close to one of the absorption peak of 6290A. A sample cell with 1cm in optical length was placed at the center of the pulse magnet where the field inhomogenity is less than 0.3% for the specimen. Liquid oxygen is prepared in the cell which is cooled by liquid nitrogen. The experiments are performed down to 60K. The transmitted laser light is detected by the photodiode. The magnetic field intensity is measured by the standard pick-up coil. All data are recorded in the digital memories.

(b)-2 Measurements Using the OMA System

The block diagram of the experiment is shown in Fig.15. The light source is a Xe flash lamp, FX-132 produced by EG & G. The lamp is set under the magnet. The light from the source go through the sample which is in the center of the magnet. The light from the sample is introduced in to the optical fiber bundle and is transmitted to the spectrometer, Spex 1701. The spectra from the spectrometer are detected and recorded in OMA.

The OMA system (OMA-2) has 500 photo-detecting channels and the system is connected to the Spex 1701 spectrometer. Each channel of the OMA recives spectrum width of $0.5cm^{-1}$. The overall spectrum observed is $250cm^{-1}$ in one shot. The sensitivity is as well as that of a usual photomultiplyer.

A start pulse, which is generated by a master-pulser trigger excites both the magnet-power-supply and the delayed pulser of

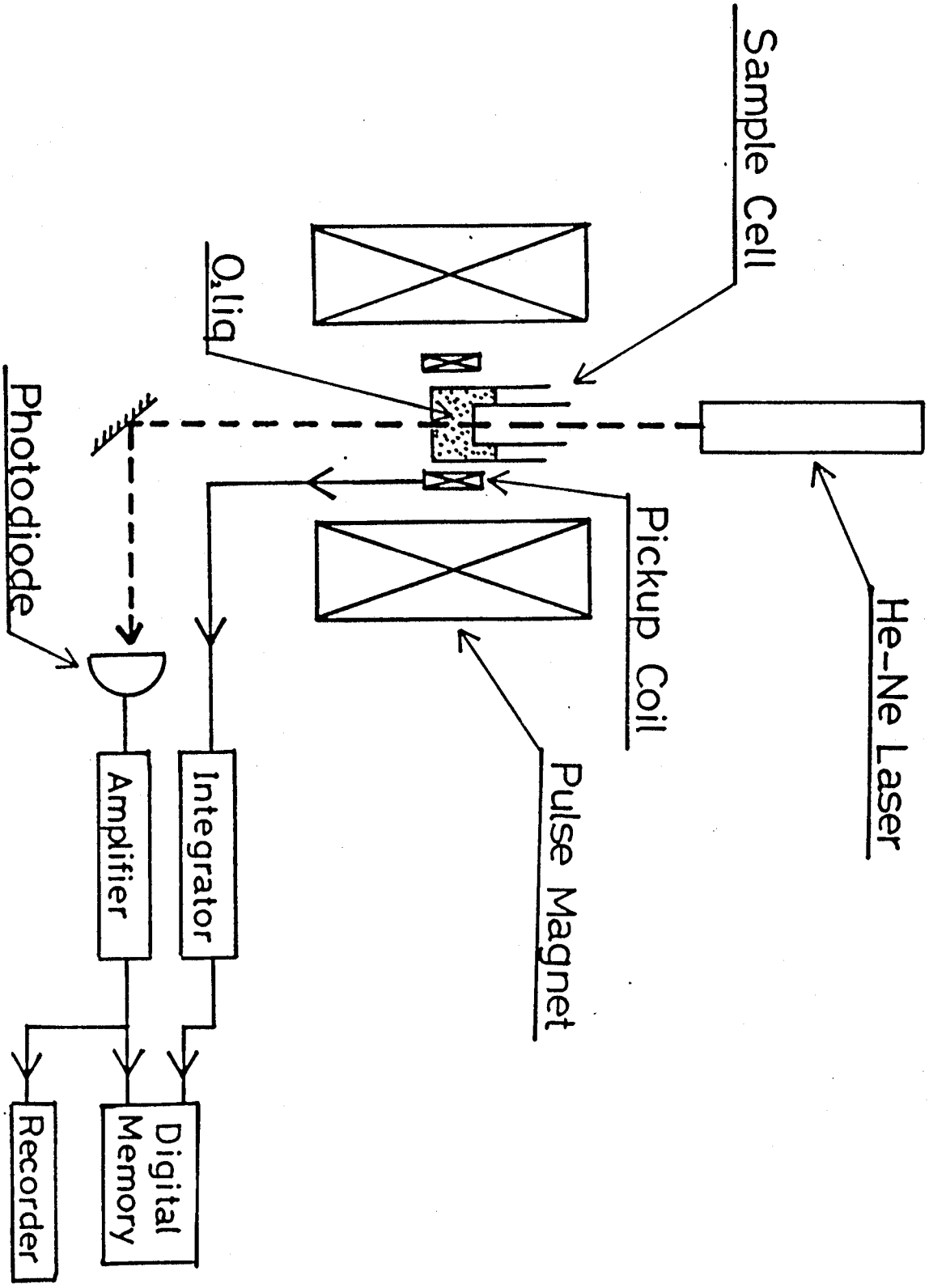

Fig.14 Schematic view of the experiment for He-Ne laser light absorption.

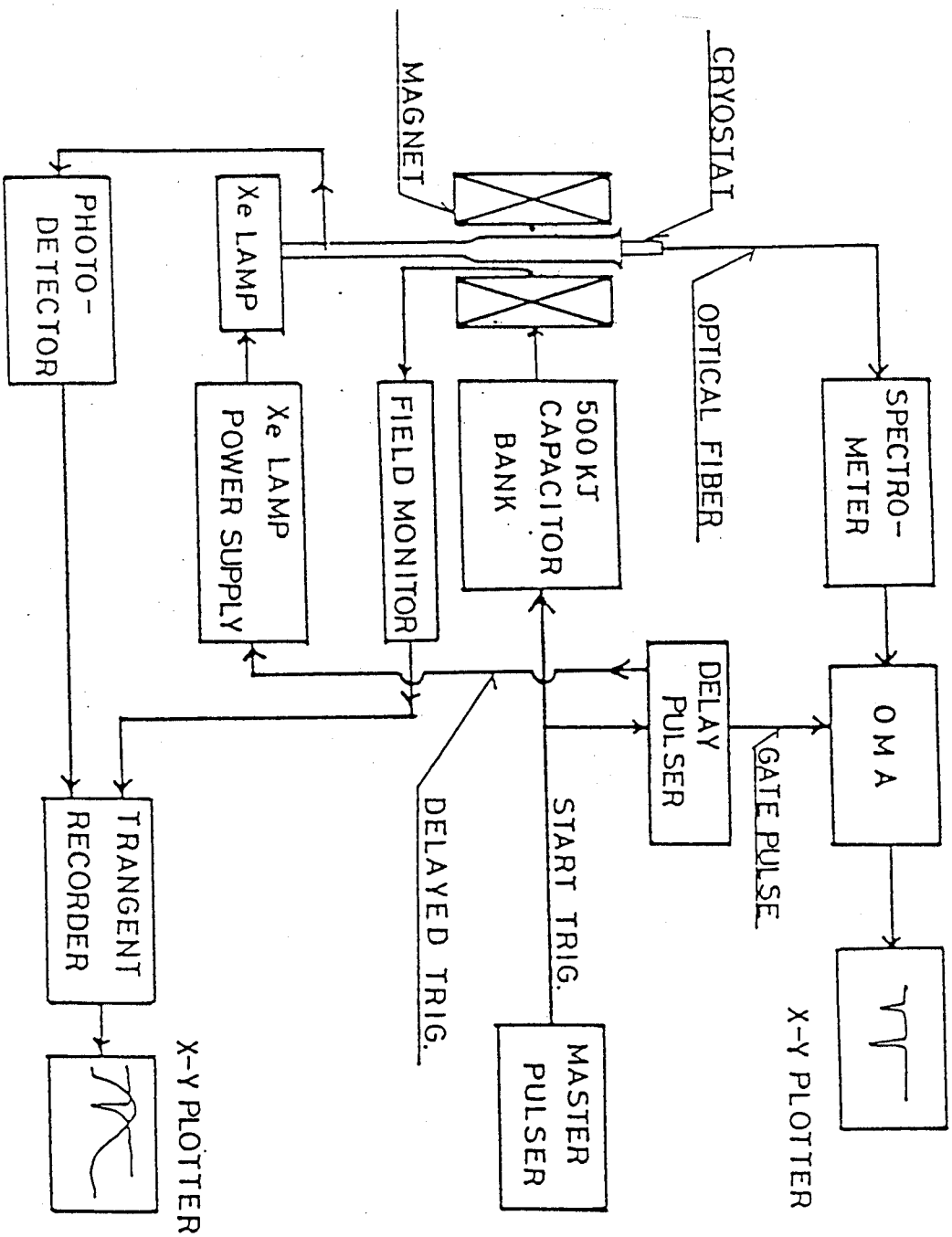

Fig. 15. Block diagram of the OMA measuring system.

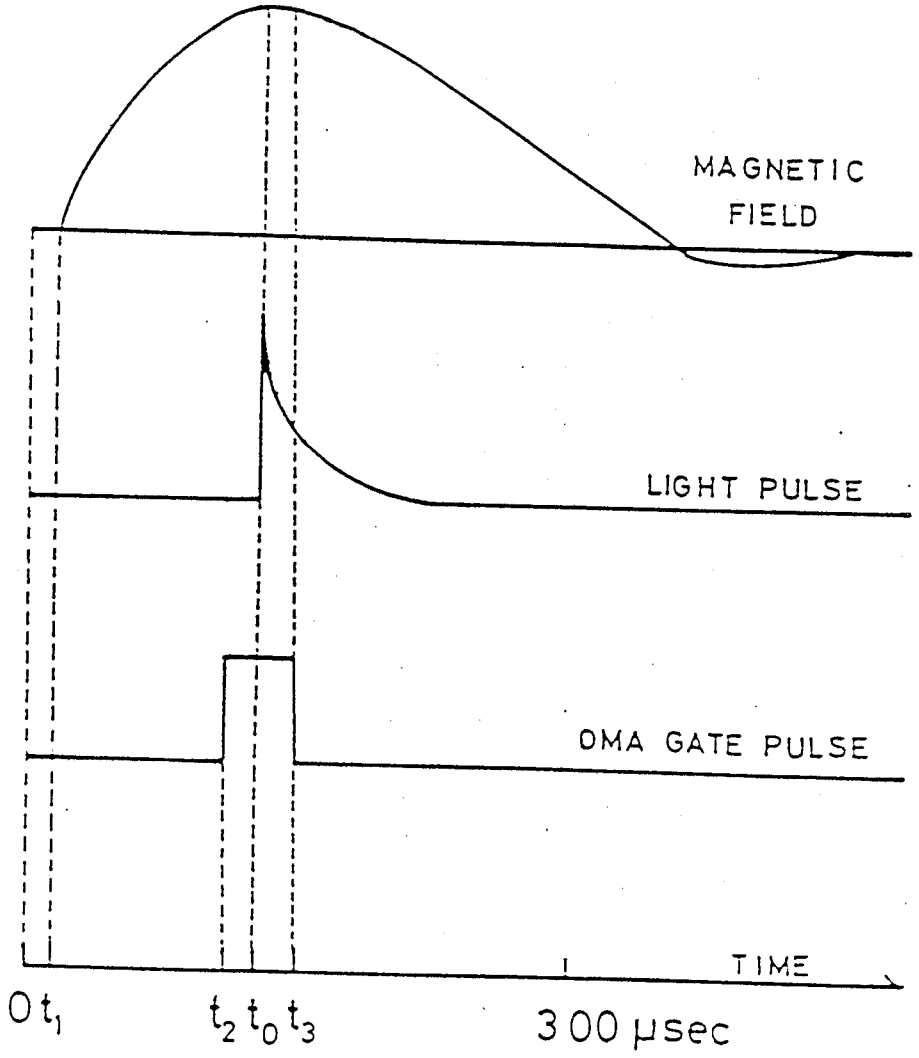

Fig.16 Time chart of pulsed magnetic field, pulsed light and gate pulse of OMA.

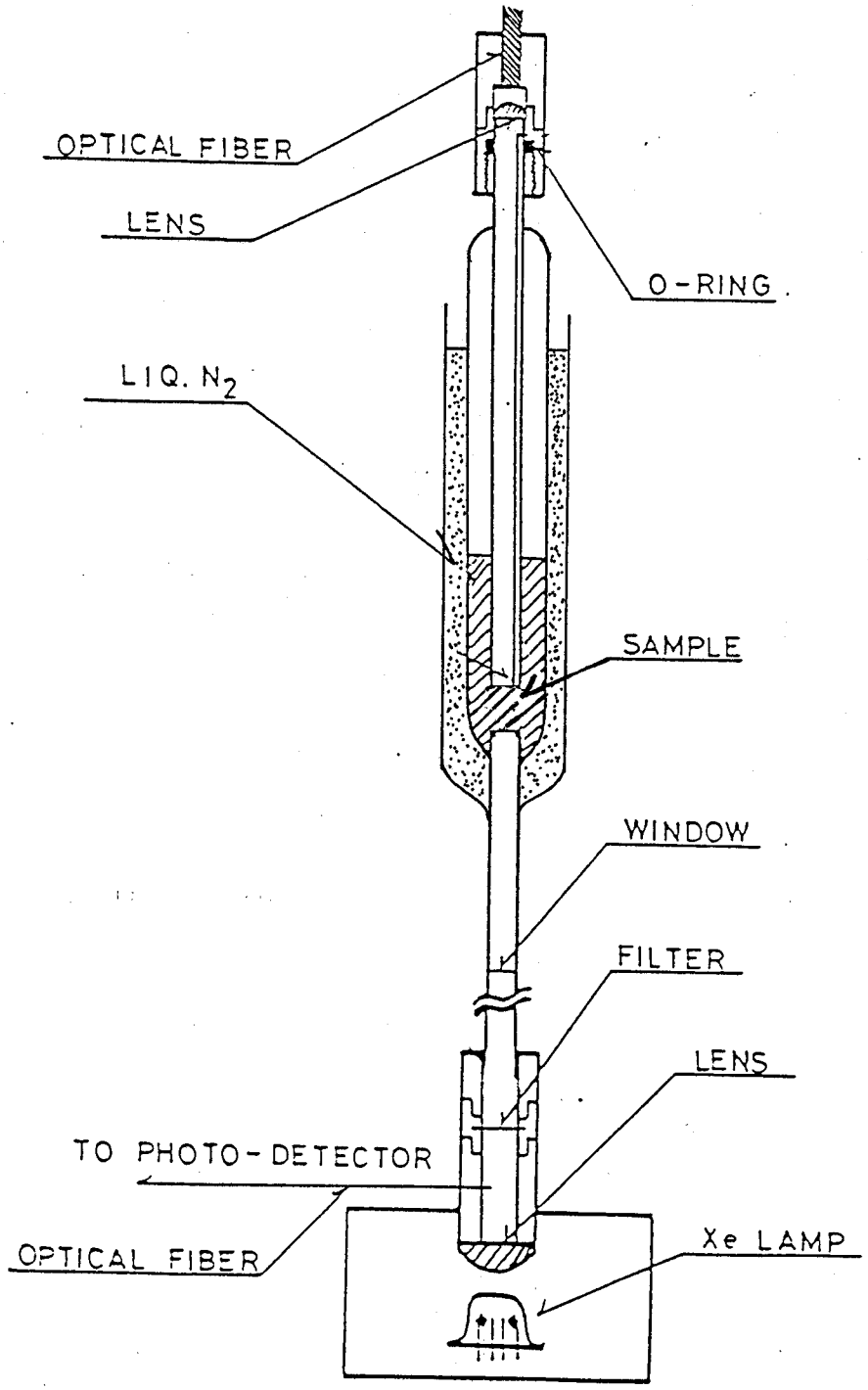

Fig.17 Cut view of the cryostat used in the OMA measurement.

OMA system as is shown in Fig.15. The delayed pulser generates two pulses. One of them is a trigger pulse of the Xe flash lamp and another one is the gate pulse of the OMA. The time chart of all triggers is shown in Fig.16. The master pulser starts at t=0 and the magnet system starts at t_1. The delay is not necessary for the present experiment and is used only for other special measurements. The OMA gate is open at t_2 just before the magnet shows the maximum field. t_2 is about 90μsec from t=0. The maximum field is obtained at t_0 after 10μsec of t_2 and the light pulse starts at t_0 with an intensity curve given in Fig.16. The OMA gate is closed at t_3 after 10μsec of t_0. The magnetic field change about 2% during t_0 and t_3. The observed data are recorded on an X-Y plotter after reducing a background noise by subtracting the OMA output signal without the Xe lamp.

The cut view of the cryostatis shown in Fig.17. Liquid oxygen is prepared at the bottom of an optical cell made of Pyrex glass and cooled by liquid nitrogen. Two condenser lenses and a window are used also for preventing air contamination.

(c) Measurements of Magneto-Volume Effect

The magneto-volume effect is investigated in a superconducting magnet up to 80kOe[15]. The magnet has an inner diameter of 60mm and the oxygen sample cell consisted of a liquid reservoir (12cc) with a capillary tube of 1mm in diameter are used as is shown in Fig.18. The field inhomogeneity is less than 0.013% inside the liquid cell. The set up of the experiment is shown in Fig.19. Small volume change of the liquid is magnified by the capillary tube and the liquid level in

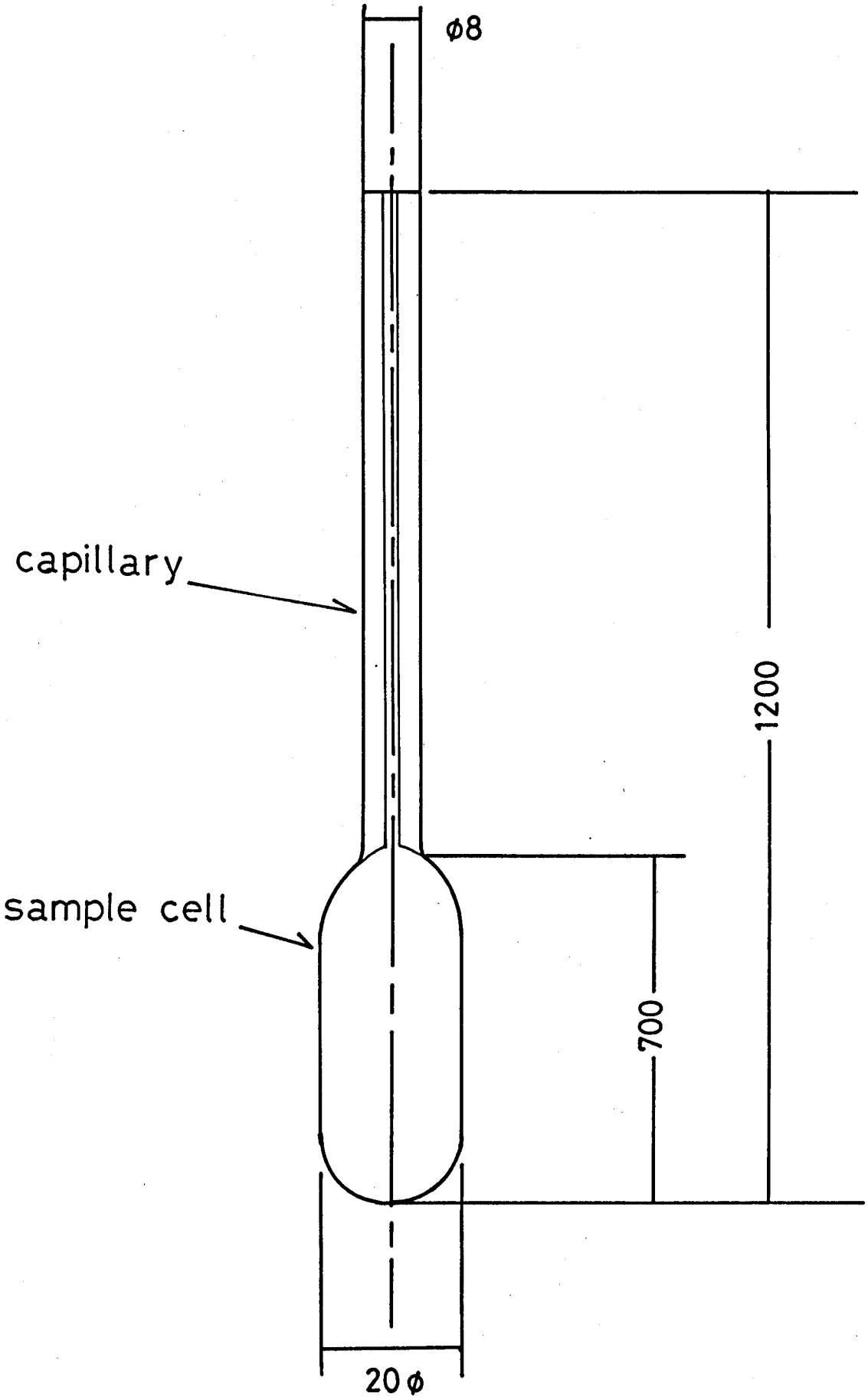

Fig.18 Cut view of the sample cell used in the measurement of the magneto-volume effect.

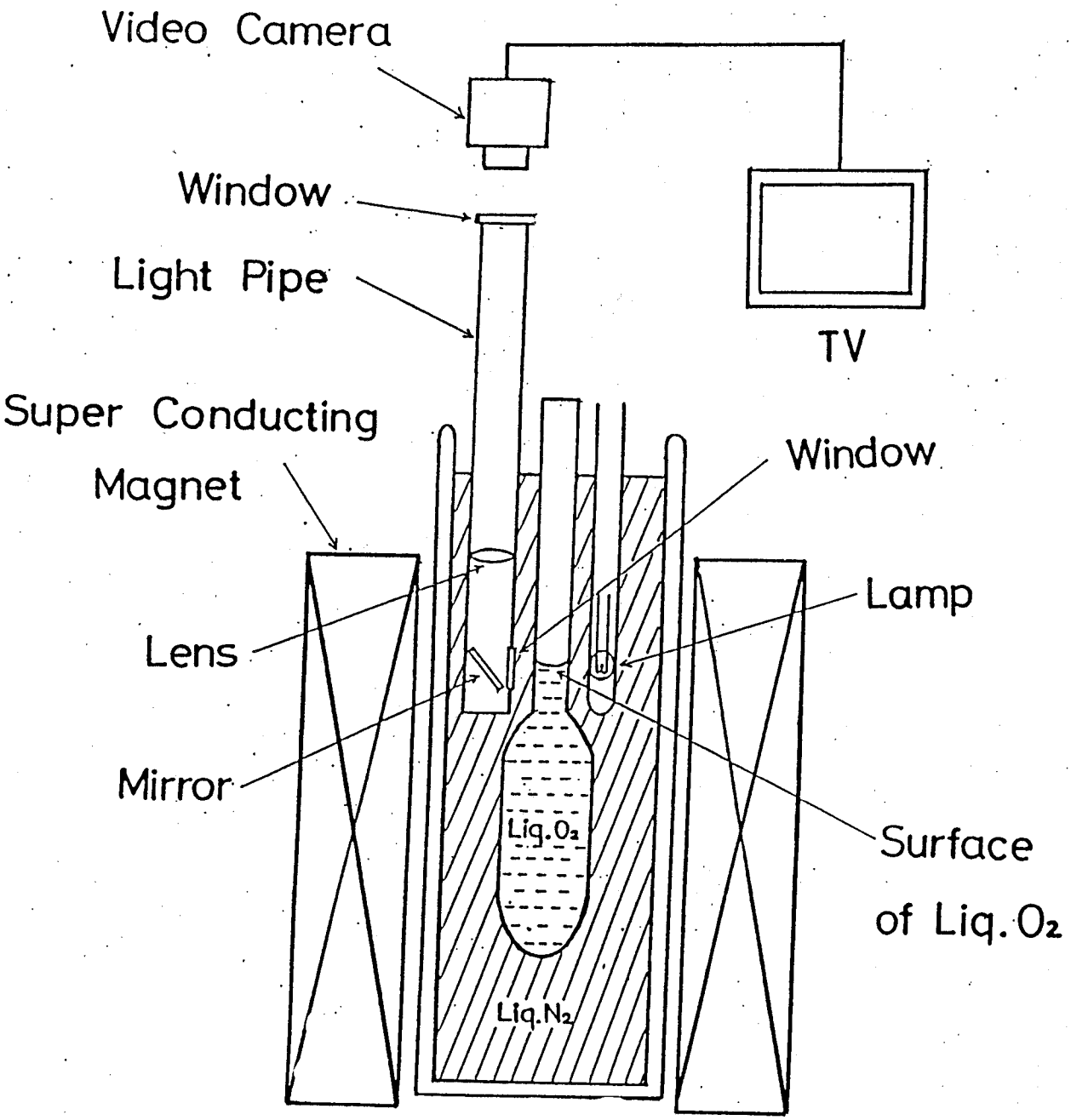

Fig.19 Experimental setup of the magneto-volume measurement.

the capillary is monitored by using a priscope and TV-camera system. The sample cell is cooled down by liquid nitrogen and liquid oxygen with 99.9% in purity is prepared in the cell by controlling the oxygen pressure.

The volume change of liquid oxygen is measured by sweeping the magnetic field with the speed of 8kOe per minute.

§4. DETERMINATION OF H_c IN POLYCRYSTALLINE ANTIFEROMAGNET

As it is mentioned in section one, the magnetizations of the three phases of solid oxygen are measured in the pulsed high magnetic field and a sharp peak appears in the dM/dH curve of the α-phase around H_0 = 70kOe, which comes from the spin flop transition expected in antiferromagnets. One should be careful to decide the spin flop critical field H_c from the dM/dH curve because the curves are measured results of powdered sample and there is no theory so far to identify the peak field to H_c. Therefore, it is necessary to calculate the powdered magnetization curve to compare with the experimental data.

The calculation was carried out at T=0K for the orthorhombic case, under the assumption that the anisotropy energies are small enough compared with that of the exchange interaction. The obtained curves are shown for various ratios of the orthorhombic anisotropy energies K_2/K_1 and compared with the high field magnetization data of some powder antiferromagnets.

Direction of the two sublattice moments M_+ and M_- under an external magnetic field H_0 with the direction cosines of α_H, β_H and γ_H are discussed. M_+ couples with M_- by an antiferromagnetic field parameter A with the energy of AM_+M_-, A>0. The orthorhombic anisotropy energy U_A is induced as

$$U_A = (K_1/2)(\beta_+^2+\beta_-^2) + (K_2/2)(\gamma_+^2+\gamma_-^2), \quad K_2>K_1>0, \quad (1)$$

where the spin axis is taken along the x-axis. β_+, γ_+ and β_-, γ_- are direction cosines of M_+ and M_-, respectively.

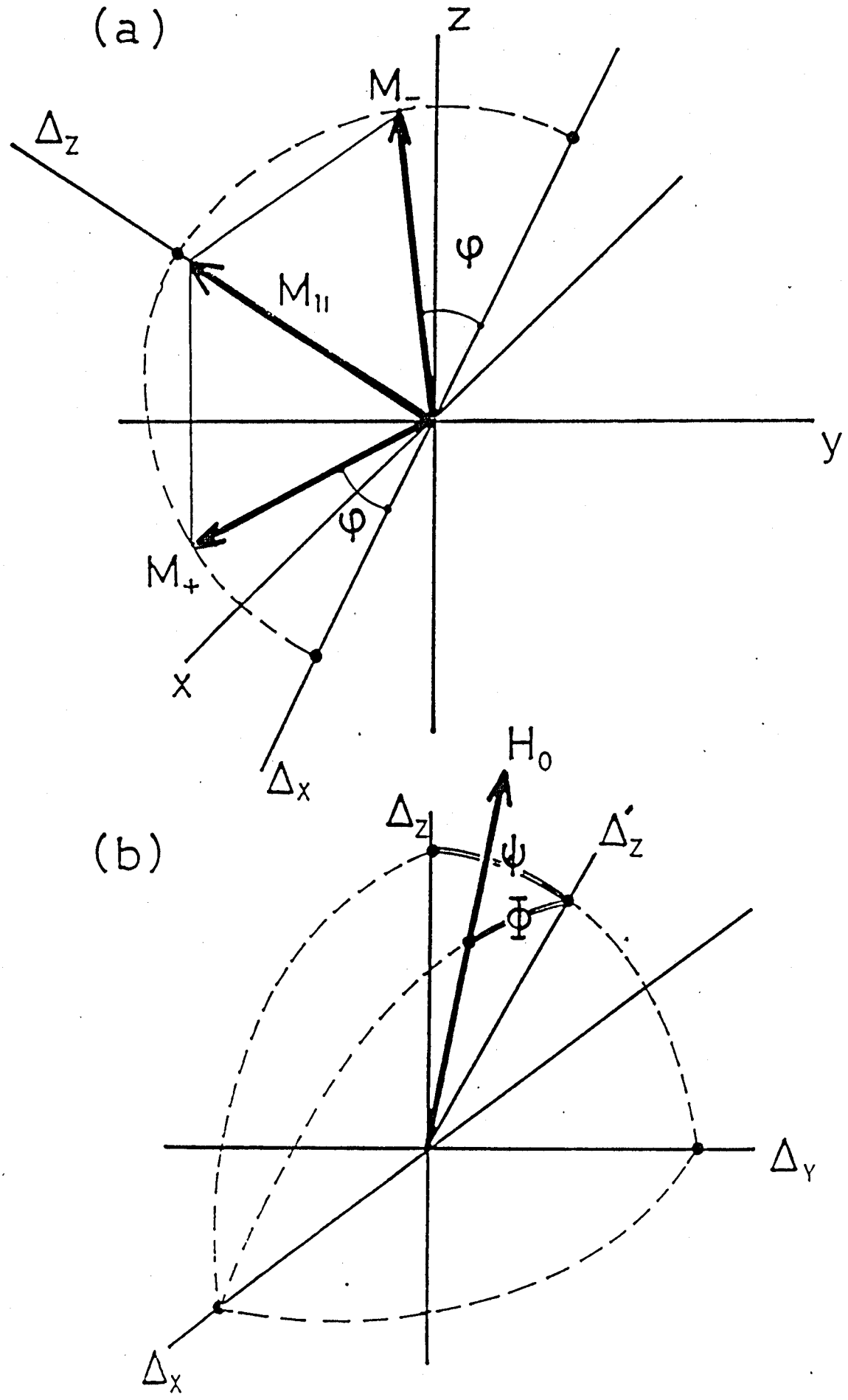

Fig.20 Relation of the magnetizations and an external magnetic field H_o with respect to various axes given in the text.

Various problems in this case are solved by Nagamiya[26] and it is referred as ref-26) hereafter.

Figure 20 shows the schematic view of the system where x-, y- and z-axes are taken along the spin easy-, second easy- and hard axes, respectively. New coordinates Δ_x, Δ_y and Δ_z are introduced. Δ_x is parallel to M_+-M_-, and Δ_z which is parallel to the net magnetization $M_{//} = M_+ + M_-$, is perpendicular to Δ_x. An angle φ in Fig.20-(a) expresses the moment canting. Figure 20-(b) shows the relation between the magnetic field H_o and the new coordinates. Angles Φ and ψ are defined as are given in (b). Φ is simply expressed by

$$\sin\Phi = \alpha\alpha_H + \beta\beta_H + \gamma\gamma_H, \qquad (2)$$

where α, β and γ denote the direction cosines of the Δ_X-axis.

Free energy of the system at T=0K is written by sum of the Zeeman, exchange and anisotropy energies as

$$F = -2H_oM\sin\varphi\cos\Phi\cos\psi - AM^2\cos2\varphi + (K_1\beta^2 + K_2\gamma^2)\cos^2\varphi + (K_1\beta'^2 + K_2\gamma'^2)\sin^2\varphi, \qquad (3)$$

where α', β', and γ' are the direction cosines of the Δ_z axis referred to the xyz-system. Many angular parameters in eq.(3) are arranged in the following way. As there are three relations, $\alpha^2 + \beta^2 + \gamma^2 = 1$, $\alpha'^2 + \beta'^2 + \gamma'^2 = 1$ and $\alpha\alpha' + \beta\beta' + \gamma\gamma' = 0$, the number of independent variables are three in $\alpha, \beta, \gamma, \alpha', \beta'$, and γ'. We tentatively remain

α, β, γ and ψ instead of these parameters. Then the free energy of eq.(3) has five parameters, $\alpha, \beta, \gamma, \varphi$ and ψ. Minimizing the free energy with respect to two angular parameters φ and ψ, Nagamiya obtained the relation given by

$$F=(1/2A)H_o^2\{(\alpha\alpha_H + \beta\beta_H + \gamma\gamma_H)^2 - 1\} + K_1\beta^2 + K_2\gamma^2. \quad (4)$$

φ and ψ should satisfy the following relations:

$$\sin\varphi = H_oM\cos\Phi\cos\psi/\{2AM^2 + K_1(\beta'^2-\beta^2) + K_2(\gamma'^2-\gamma^2)\}, \quad (5)$$

$$\tan\psi=(a\sin2\psi - b\cos2\psi)/(2AM^2 + a\cos2\psi + b\sin2\psi + c), \quad (6)$$

where a,b and c are given by

$$\begin{aligned} a &= K_1\{\beta''^2 - (\alpha\gamma'' - \gamma\alpha'')^2\} + K_2\{\gamma''^2 - (\beta\alpha'' - \alpha\beta'')^2\}, \\ b &= K_1\beta''(\alpha\gamma'' - \gamma\alpha'') + K_2\gamma''(\beta\alpha'' - \alpha\beta''), \\ c &= -(K_1\beta^2 + K_2\gamma^2), \end{aligned} \quad (7)$$

where α'', β'' and γ'' are direction cosines of the axis Δ_x' in Fig.20-(b). Detailed calculation of these parameters are omitted in this paper. As is seen in eqs.(5) and (6), $\sin\varphi$ is expressed mainly by H_o/AM term with the corrections of K_1/AM^2 and K_2/AM^2 while $\tan\psi$ is of the order of K_1/AM^2 and K_2/AM^2. It is noted that $\cos^2\psi$ can substantially be expressesd by 1 when higher order terms such as $(K_2/AM^2)^2$ are neglected. α, β and γ in eq.(4) are determind by the Lagrange method of undetermined multipliers as in ref-26) and the results are shown as follows:

$$\alpha = \sqrt{X/(X + Y + 1)},$$
$$\beta = \sqrt{1/(X + Y + 1)}, \qquad (8)$$
$$\gamma = \sqrt{Y/(X + Y + 1)},$$

with

$$X = \{(\kappa_1 - \lambda_m)\,\alpha_H/\,\lambda_m\beta_H\}^2, \qquad \kappa_1 = 2K_1A/H_o^2$$
$$Y = \{(\kappa_1 - \lambda_m)\,\gamma_H/(\kappa_2 - \lambda_m)\,\beta_H\}^2, \qquad \kappa_2 = 2K_2A/H_o^2 \qquad (9)$$

where λ_m is the minimum value of λ solved from the determinant equation

$$\begin{vmatrix} \alpha_H^2 - \lambda & \alpha_H\beta_H & \alpha_H\gamma_H \\ \beta_H\alpha_H & \beta_H^2 + (\kappa_1 - \lambda) & \beta_H\gamma_H \\ \gamma_H\alpha_H & \gamma_H\beta_H & \gamma_H^2 + (\kappa_2 - \lambda) \end{vmatrix} = 0 \qquad (10)$$

The desired magnetization of powdered antiferromagnetic specimen is obtained by summing up $M_{/\!/}\cos\Phi\cos\varphi$ which is the field projection of the induced moment. The sum is obtained by the volume integral,

$$M_P = \int M_{/\!/}\cos\Phi\cos\psi\,d\Omega/\int d\Omega \qquad (11)$$

Using eqs.(5) and (6) and neglecting the higher order terms such as $(K_2/\,AM^2)^2$, the induced magnetic moment is given by

$$M_{/\!/}\cos\Phi\cos\psi = 2M\sin\varphi\cos\Phi\cos\psi$$
$$= (H_o/A)\cos^2\Phi[1-\{K_1(\beta'^2-\beta^2)+K_2(\gamma'^2-\gamma^2)\}/2AM^2] \quad (12)$$

$\cos^2\Phi$ in eq.(12) is simply expressed by α, β and γ as seen in eq.(2). β' and γ' in the correction terms are expressed as

$$\beta' = (\beta_H - \beta\sin\Phi)/\cos\Phi,$$
$$\gamma' = (\gamma_H - \gamma\sin\Phi)/\cos\Phi, \quad (13)$$

where $\psi=0$ is used for the correction terms. Thus, the induced moment can explicity be expressed by α, β and γ, and M_p can be obtained by computer calculation. A BASIC program for the calculation is given in Appendix V.

Figure 21 shows the computer calculated field dependence of polycrystalline magnetization curve in the form of dM/dH for various ratios of K_2/K_1. The abcissa and ordinate are normalized by the spin flop field $H_c = \sqrt{2AK_1}$ and the perpendicular susceptibility $\chi_\perp = 1/A$, respectively. The ratio of exchange and anisotropy energies are taken as $K_2/AM^2 = 1/100$. It is evident that the field value at the peak of dM/dH curve coincides well with the spin flop critical field H_c independent of the ratio of orthorhombic anisotropy constants K_2/K_1. The profile of dM/dH at H_c becomes sharp as K_2/K_1 increases.

The calculated curves are compared with the experimental data for various K_2/K_1. All the experimental curves are obtained by using the pulsed magnet 150(1L)60 at High Magnetic Field Laboratory, Osaka University[22]. Figure 22 shows the

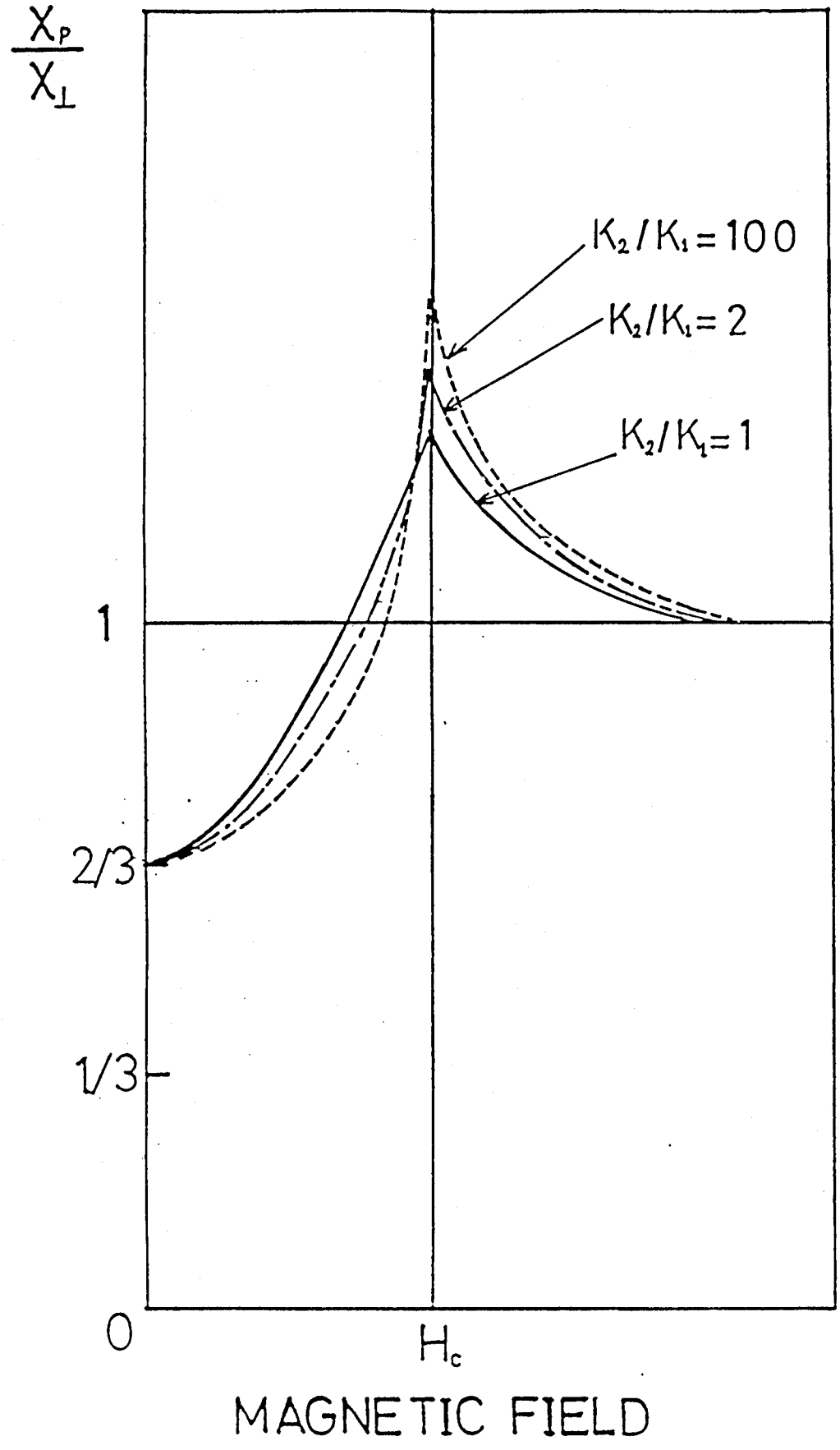

Fig.21 Calculated dM/dH curve for various ratio of anisotropic energies.

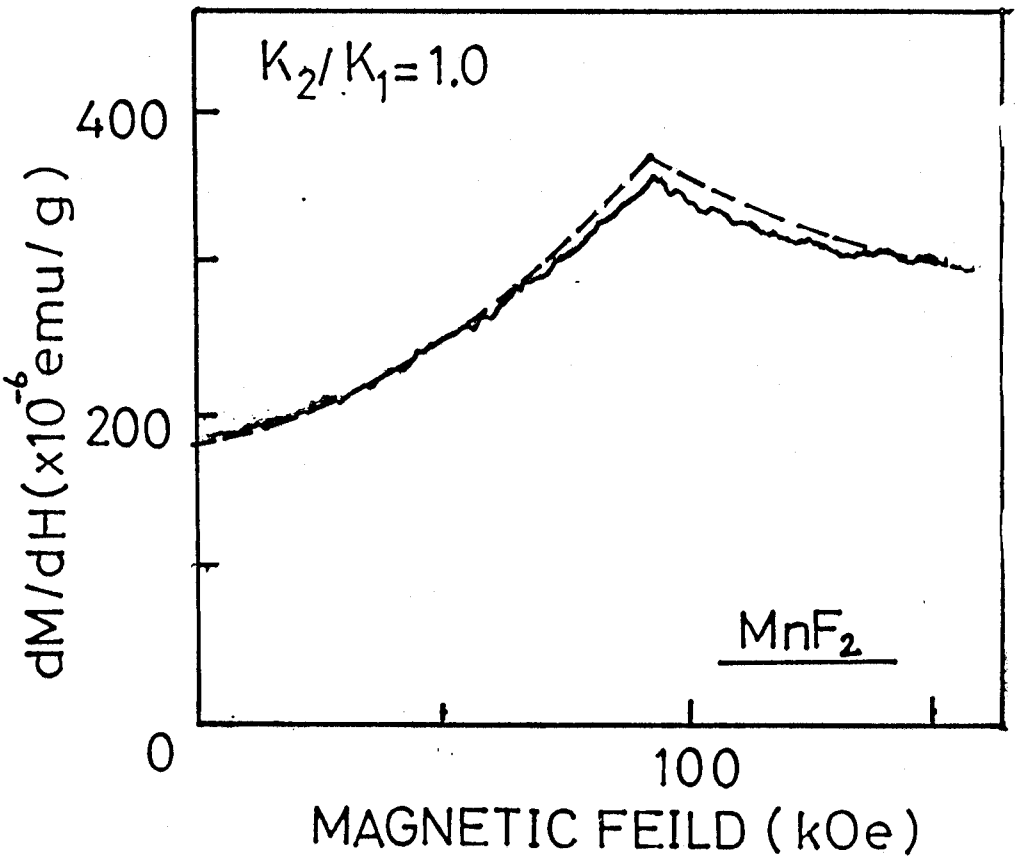

Fig.22 Comparison of theory and experiment of MnF_2.

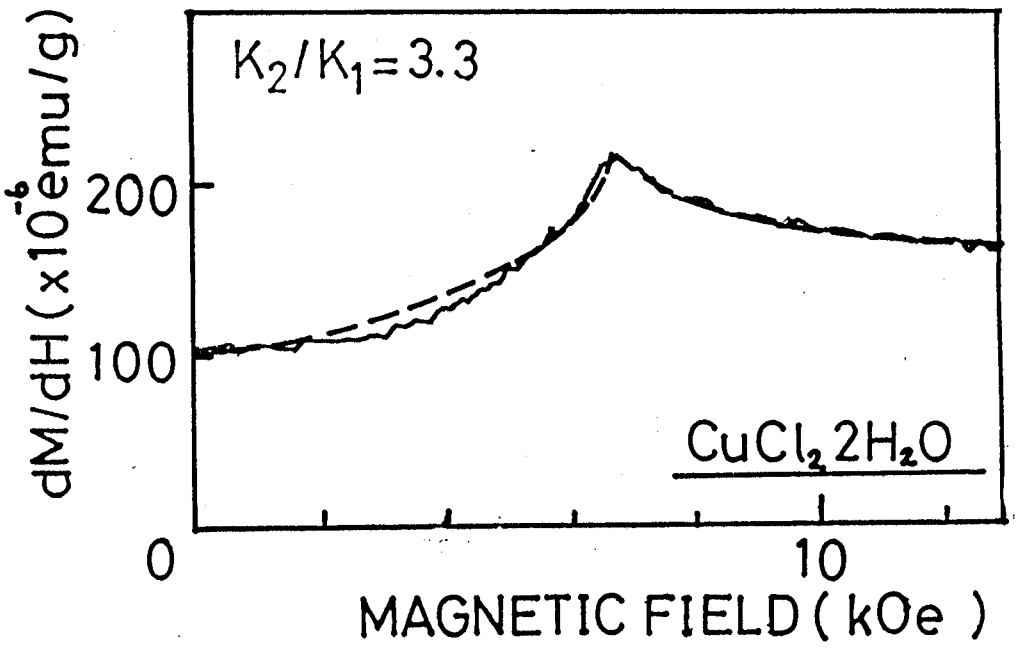

Fig.23 Comparison of theory and experiment for $CuCl_2 2H_2O$.

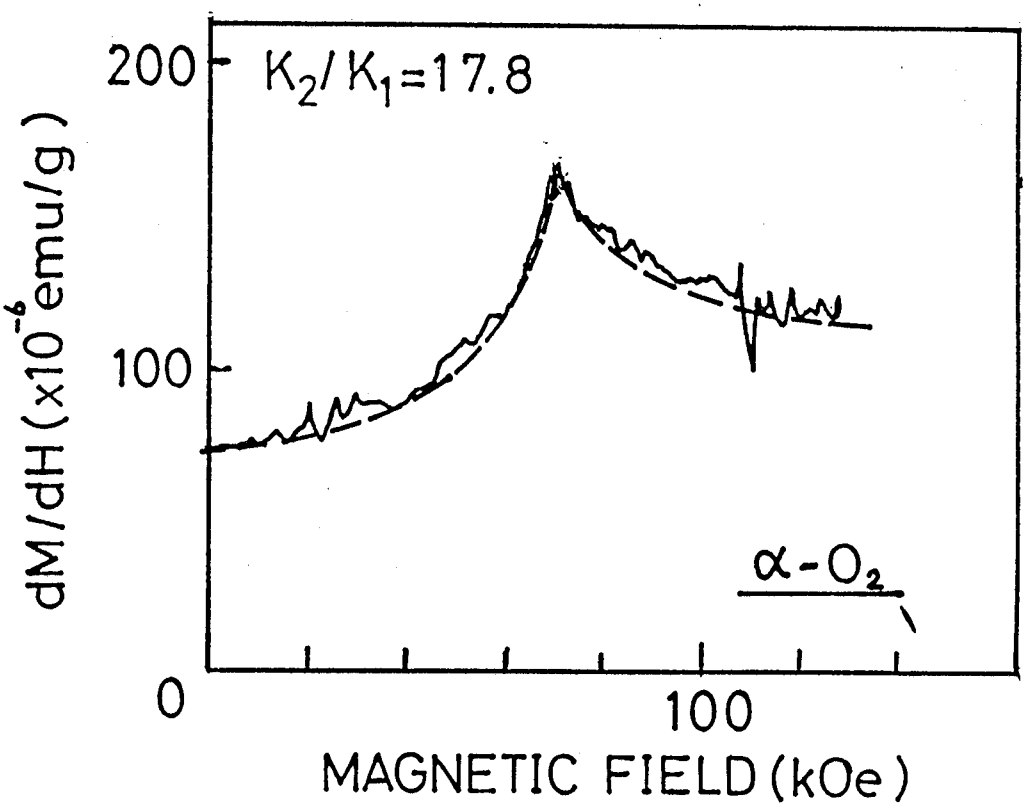

Fig.24 Comparison of theory and experiment of α-O_2.

experimental data for MnF_2 which is a typical uniaxial anisotropic antiferromagnet with $K_1=K_2$. Figure 23 shows the case of $CuCl_2 2H_2O$ with the ratio of $K_2/K_1=3.3$[26]. Figure 24 shows the case of solid oxygen(α-phase) with the ratio of $K_2/K_1=17.8$[13]. The calculated dM/dH curves for these materials are in good agreement with the experimental curves.

Similar problem was discussed by Ostrovskii[27] and Meier[28] for the solid oxygen. However, they assumed that K_2 is large compared with K_1. Therefore, the results are not applicable to general cases. It is also noticed that powdered specimen does not show a clear magnetization change at H_c while the differential magnetization dM/dH gives a sharp peak at H_c. This means that the critical field determination under a pulsed magnetic field is more effective than the static mesurements because dM/dH curve is easily obtained in the pulsed measurements.

§5. MAGNETISM IN SOLID OXYGEN

(a) Experimental Results

Typical magnetization curves are shown in Fig.25. All solid curves are linear except the low field region in the α-phase and the nonlinearlity below 100kOe comes from the spin flop phenomenon. The dM/dH curve of α-phase is given in Fig.26 for various temperatures. The peak in the dM/dH curve can be substantially observed at H_c, as is discussed in section four.

The observed temperature dependence of H_c is given in Fig.27-(a). H_c increases as temperature increases and no peak is found in the β-phase. dM/dH above H_c reflects the perpendicular susceptibility and one can determine the exchange field from the observed value. It is noted that the magnetization above H_c becomes nonlinear when the temperature is close to $T_{\alpha\beta}$. An example of the nonlinear magnetization at 22.0K is shown in Fig.25 by a broken line above 300kOe. The field induced phase transformation may be possible just below $T_{\alpha\beta}$ which may be the cause of the nonlinearity.

Temperature dependence of the observed magnetic susceptibility is shown in Fig.28. Powdered susceptibility χ_p is obtained from the low field data and perpendicular suscetibility is obtained from the data above H_c. The results suggest that the intrinsic T_N should be around 30K if the phase transition temperature $T_{\alpha\beta}$ were above 30K, which agrees with the conclusion by DeFotis[5].

(b). Magnetism in α-phase

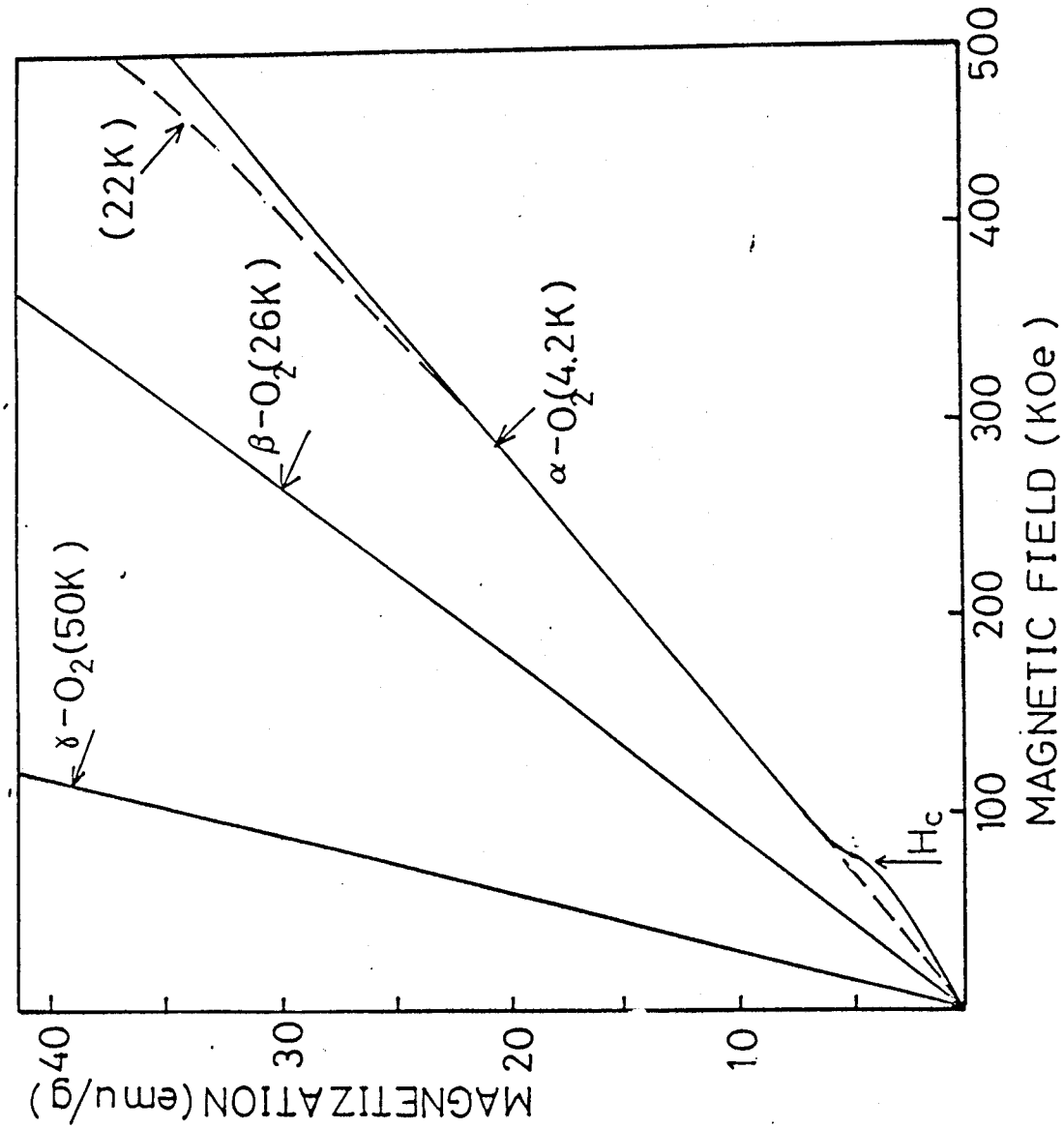

Fig.25. Magnetization curves of oxygen in three phases.

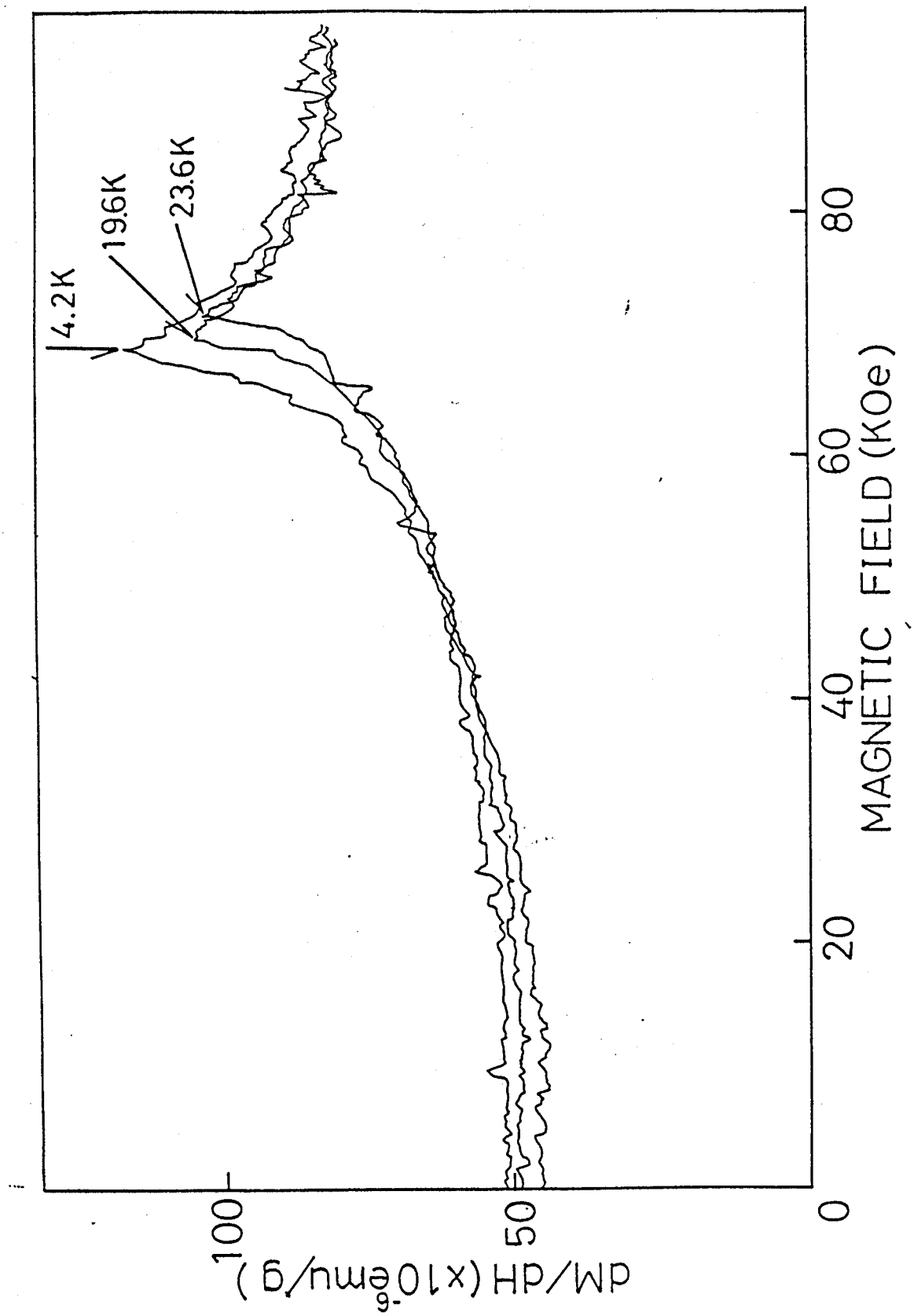

Fig.26. dM/dH curves of oxygen in the α-phase. Arrows show H_c in each temperature.

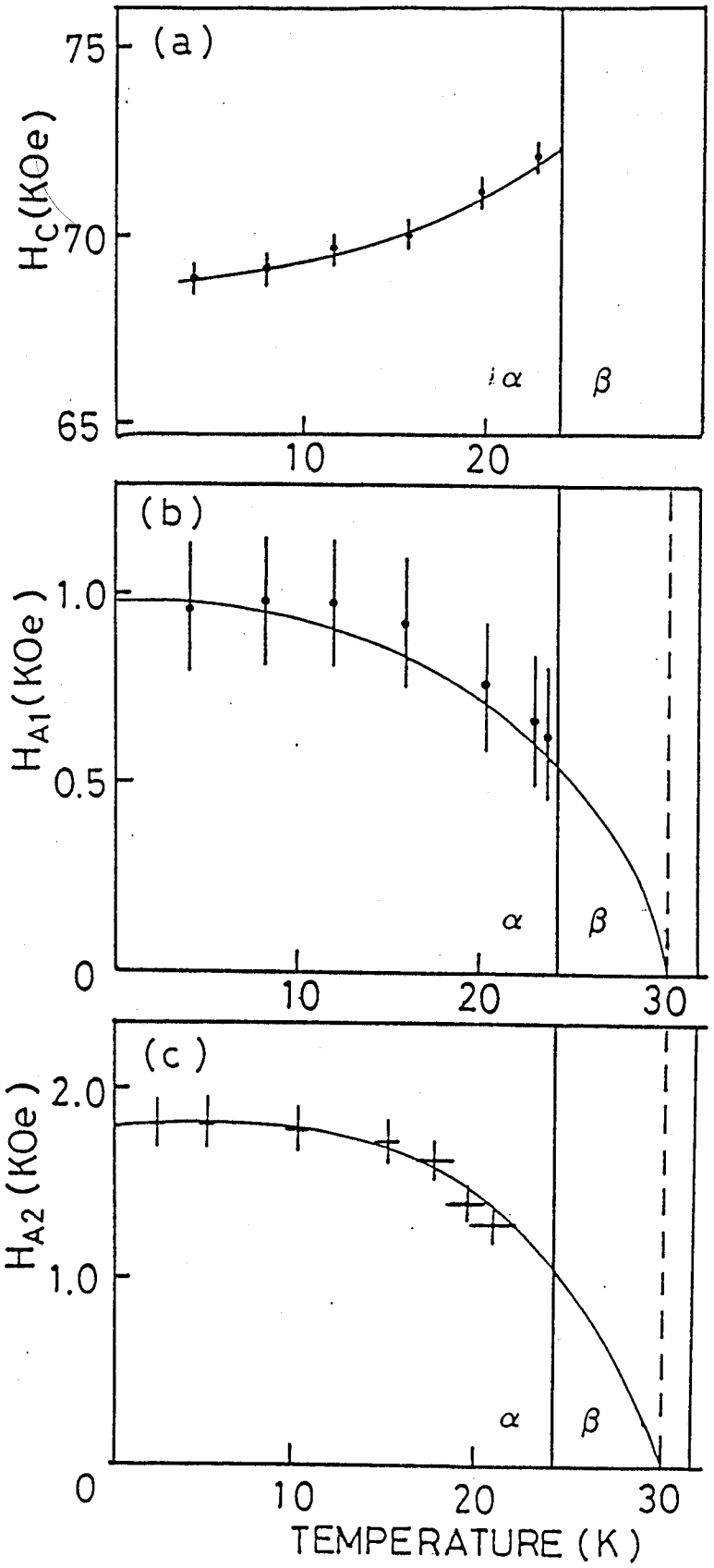

Fig.27. Temerature dependences of H_c, H_{A1} and H_{A2}.

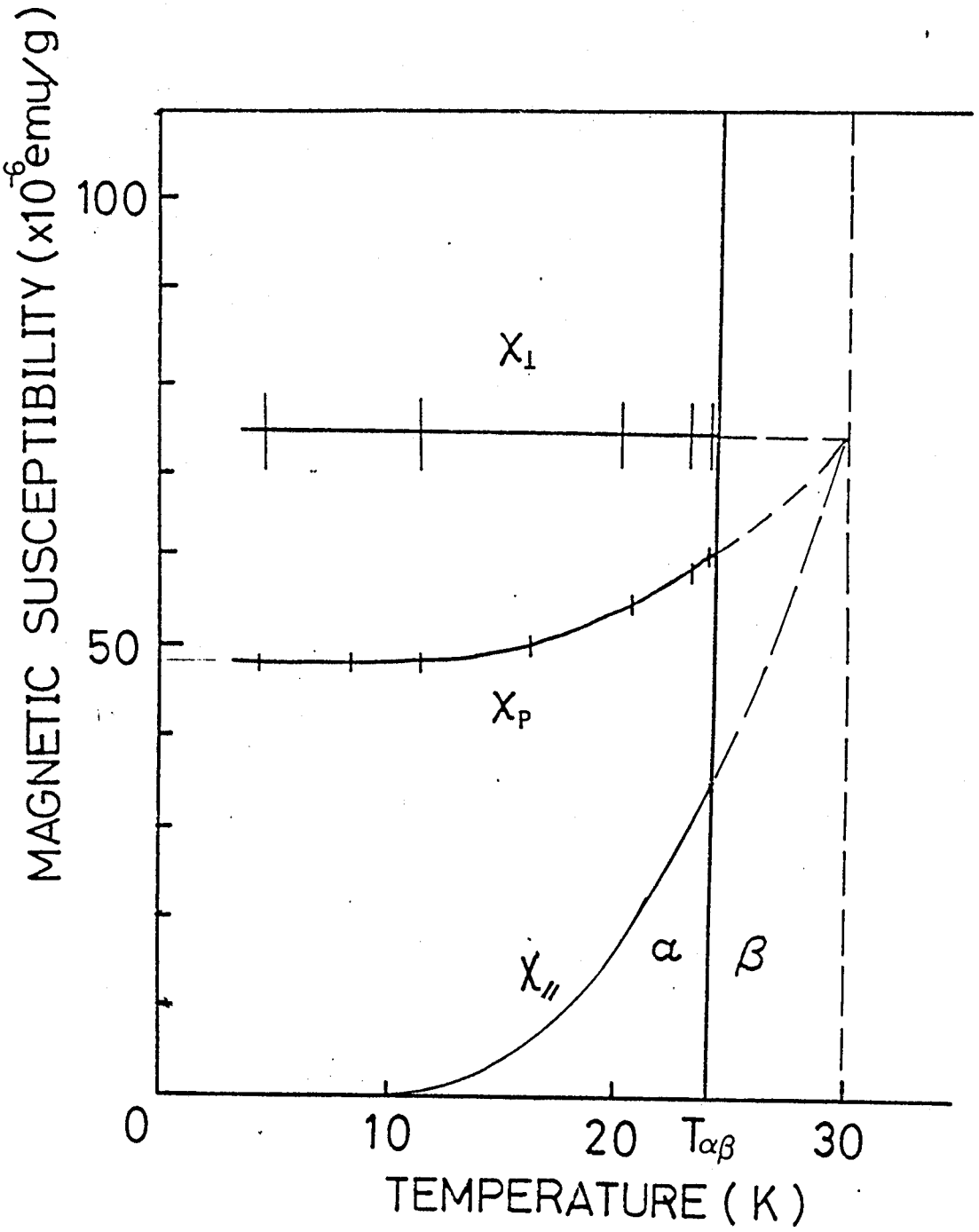

Fig.28. Temperature dependences of the perpendicular, parallel and powdered susceptibilities in the α-phase.

The exchange field H_E on each spin with S=1 is estimated by the following formula:

$$H_E = AM_o, \qquad (14)$$

where A is the molecular field constant which is obtained from the perpendicular susceptibility value as

$$\chi_\perp = 1/A = 75 \pm 5 \times 10^{-6} \text{ emu/g}. \qquad (15)$$

M_o in eq.(14) is the sublattice magnetization given by

$$M_o = Ng\mu_B S/2 = 175 \text{ emu/g}. \qquad (16)$$

using these values, H_E is determined as

$$H_E = 2.3 \times 10^3 \text{ kOe, or } 2.3\text{MOe}, \qquad (17)$$

which agrees with Meier`s result[12].
The anisotropy field H_{A1} is estimated from the critical field H_c using a standard treatment[26] as

$$H_c = 69 \text{ kOe}(4.2\text{K}) = (2H_E H_{A1})^{1/2}. \qquad (18)$$

Using value of H_E in eq.(17), H_{A1} is obtained as

$$H_{A1} = 1.0\text{kOe}. \qquad (19)$$

H_{A1} is also calculated from the antiferromagnetic resonance data.

Wachtel and Wheeler[11] obtained the low frequency mode of 6.4 cm^{-1} at zero magnetic field. As the corresponding field ω/γ is H_c in eq.(18)[13], one can calculate H_{A1} and the result is 1.0kOe which is just equal to eq.(19). It is noted that Meier et al [12]. obtained dM/dH peak corresponding to H_c at nearly right position but their evaluation of H_c is 30% higher than ours and their value is inconsistent with the antiferromanetic resonance data. H_c value estimated from neutron diffraction by Stephens et al.[21] is about three times larger than ours. Another anisotropy field H_{A2} is evaluated from the antiferromagnetic resonance frequency of the higher mode and H_E in eq.(17) as

$$H_{A2} = 18.0 \text{ kOe} . \qquad (20)$$

Temperature dependence of H_{A1} and H_{A2} are shown in Fig.27(b),(c) where H_{A1} is estimated from our experimental result and H_{A2} is obtained from the resonance data obtained by Blocker et al.[10] Both results indicate that T_N is around 30K. Origin of the anisotropy energies is considered in the following way: H_{A1} will come mainly from the dipoole energy while H_{A2} may come from the molecular origin. Estimation of H_{A2} is not so easy because up to now no reliable formula for the magnetic anisotropy of the molecular origin in the condensed phase is obtained. On the other hand, the dipolar anisotropy field can be obtained by calculating dipole sum. We calculated the sum using the standard formula and obtained the following result. The

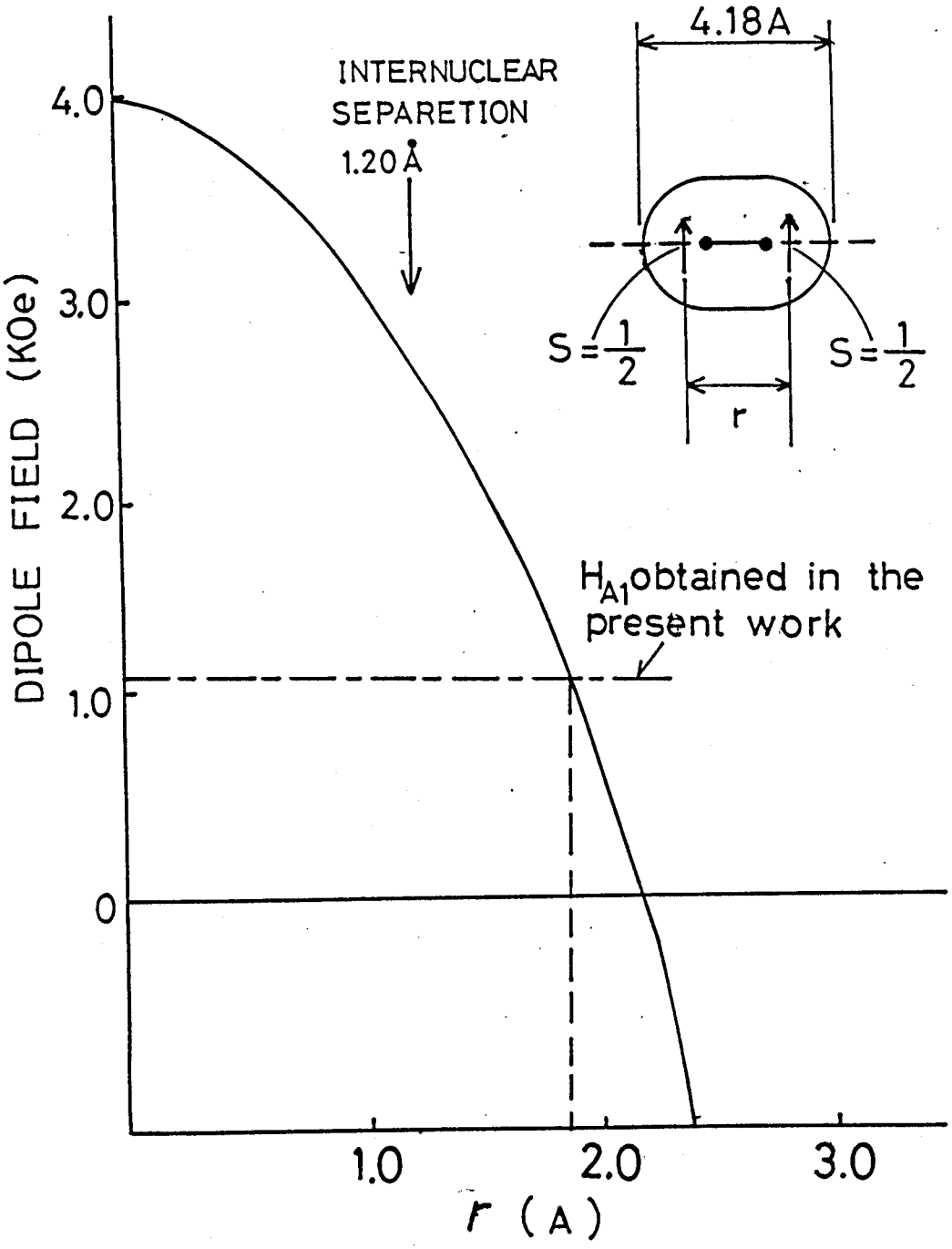

Fig.29 Calculated dipolar anisotropy field as a function of the spin-spin distance r.

experimental value of H_{A1} in eq.(19) is not obtained if the point dipole at the center of molecule is assumed. Therefore, the spin-distribution model shown in Fig.29 is introduced. Total magnetic moment is divided into two parts along the molecular axis with distance r. The dipole field is calculated as a function of r and the best agreement with experiment is obtained by putting r to be 1.9A which is a little larger than the internuclear distance. The result seems to be reasonable considering the distribution of antibonding magnetic orbital, $\pi^*_y 2p$ and $\pi^*_z 2p$.

The exchange constant J defined by Hamiltonian of $-2JS_iS_j$ is estimated from H_E value considering the crystal and spin structures of the α-phase. In the molecular field approximation, eq.(14) is written as $H_E = 2zJS/g\mu_B$, where z is number of nearest neighbors. Historically, there are some discussions about z in the α-phase. It seems to be natural to consider z = 4 in accord with the result of Burakhovich et al.[29] because the spin system can be regared as two-dimensional from the intermolecular separation. If the spin system were three dimensional i,e, the interlayer neighbors had the same exchange with the intraplane value, T_N would be around 200K but it is only about 30K as is shown before. So we assume that the α-phase is two-dimensional with main in-plane exchange interaction of z=4. The main exchange J_α is determined by considering the spin reduction in two-dimensional magnet[30,31]. $\chi_\perp$ in this case is given by

$$\chi_\perp = (N/2)(g^2\mu_B^2/2zJ)(1- \Delta S/S), \qquad (21)$$

where z=4 and S=1. ΔS reflects the effect of zero-point spin deviation and is 0.2 when H_{A1} is small enough compared with H_E. From eqs.(15) and (21), J_α is obtained as

$$J_\alpha/k = 30 \pm 2K \qquad (22)$$

The next neighbor intraplane exchange interaction J'_α is estimated by Etters et al[32] as the ratio $J'_\alpha/J_\alpha = 0.25$. This gives the value of J'_α as

$$J'_\alpha/k = 7.5 \pm 2\ K \qquad (23)$$

(C) Mgnetism in β-phase

Recent neutron diffraction study[9] suggests that the spin short range order may exist in the β-phase. As it is seen in Fig.5, the separation of inter c-plane nearest nighbors is 1A larger than the intra c-plane nearest neighobors. So, for a first order estimation, the spin system can be regarded as an two-dimensional magnet. The order of the main exchange interaction i.e. in-plane exchange interaction J_β can be estimated by comparing the susceptibility data in the β-phase with that of an ideal two-dimensional antiferromagnet with S=1 and Z=6 as is done by De Jongh and Miedema[31]. The obtained value is given by

$$J_\beta/k = 22 \pm 2K\ . \qquad (24)$$

The calculated theoretical curve for powdered χ is shown in Fig.30.

(d) Magnetism in γ phase

As it is seen in Fig.8, the magnetic susceptibility of γ-phase shows a paramagnetic behavior, although a discontinuous drop is observed at the melting point and the increase of χ in the low temperature regions seem to be surpressed. This deviation from Curie-Weiss law may be due to the spin short range ordering along the linear chain system mentioned in §3-(b). Then the intra-linear chain exchange J_γ is estimated by the Bonner-Fisher model[33] while the exchange on the corner site is estimated from the Curie Weiss constant Θ of the liquid phase with the formula $\Theta = 4zJ/3k$. The J-values estimated from χ-T curve are

$$J_\gamma/k = 14 \pm 2K, \tag{25}$$

and

$$J'_\gamma/k = 2\sim3\ K, \tag{26}$$

for chain and corner site,respectively.

(e) Exchange interaction

The estimated exchange interactions of each phases are summarized in Fig.31. Meier et al.[12] measured the pressure dependence of the magnetic susceptibility and found that J(r) in the α-phase shows r^{-14} dependnce. The dependence can be considered as a part of

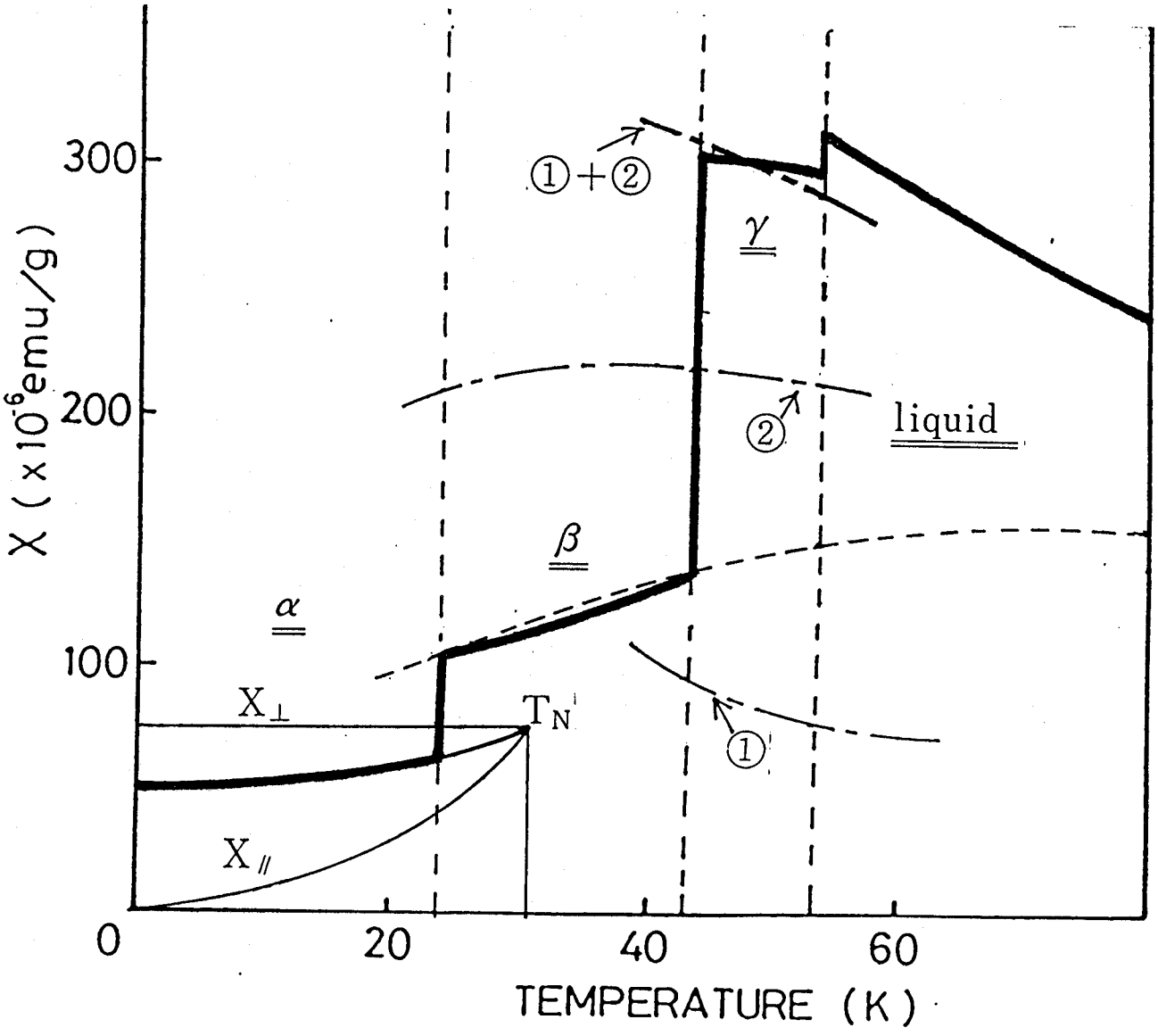

Fig.30 Experimental and theoretical χ-T curve of solid oxygen. Experimental data are shown in broad solid lines. Fine solid, dotted and dash-dotted lines show the theoretical curves of α, β and γ phase, respectively. Curve ① and ② in the γ-phase are the corner and linear chain site, respectively.

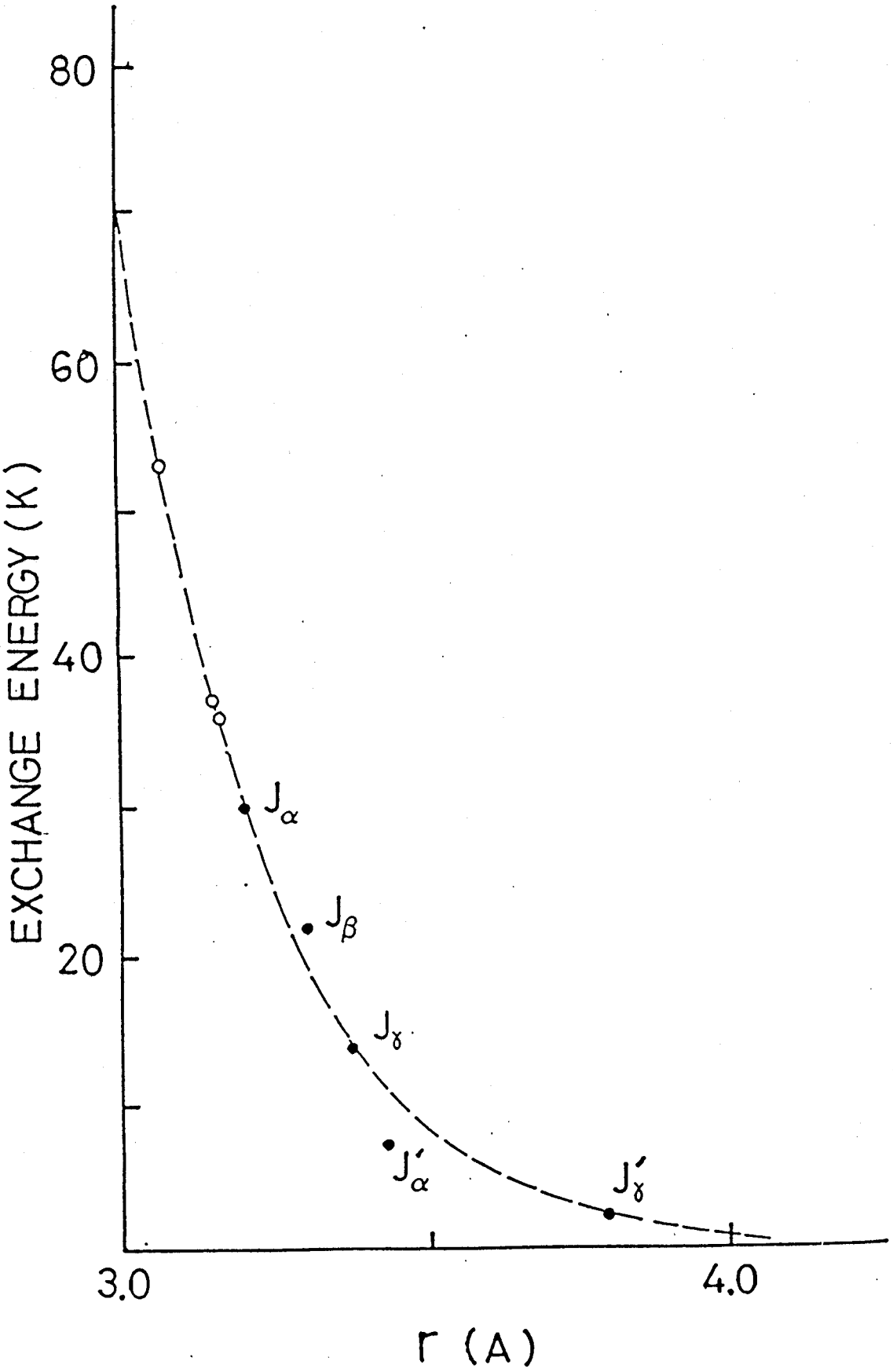

Fig.31 . Antiferromagnetic exchange interaction J as a function of intermolecular distance r. Upper three points refered from reference 12) are the high pressure data normalized by J_α in the present paper.

$$J(r) = J_o \exp\{\epsilon(r-r_o)\} \qquad (27)$$

with J_o=-30K, ϵ=-4.3A^{-1} and r_o =3.2A [13]. The values of the exchange interactions of each phases which is approximately evaluated as equations (22)-(26) show statisfactory agreement with J(r) as is shown in Fig.31. This fact also suggests that the assumptions adopted for low dimensionalities in three phases may be reasonable at least for the first order.

(f) Phase Transition at $T_{\alpha\beta}$

As is mentioned before, the phase change observed at $T_{\alpha\beta}$ has been believed as magnetically induced martensitic phase transformation and comparison of the ground state energies of the α- and β-phases is done by Etters et al.[32]. Stimulated by a reliable determination of exchange interactions in three phases as in Fig.31, the formation energies in α- and β-phases are calculated using Kihara potential[34,35] which is regarded as the best expression for nonpolar dimer molecules. Usually, Lennard-Jones potential is used to estimate the binding energy of molecular crystals[32]. However, the potential is not accurate for solid phases of dimer molecules such as O_2 or N_2 because the binding energy depends on mutual angular relation of the molecular axes. The Kihara potential is expressed as

$$U = U_o(\rho_o/\rho_1)^{12} - W_o F(\theta)\, \rho_2^{-6} + (3Q^2/4r^5) f(\theta),$$

$$F(\theta) = 3.90\,(9\cos^4\theta - 8\cos^2\theta + 1) + 10.9(3\cos^2\theta - 1) + 45.5$$

$$f(\theta) = 35\cos^4\theta + 30\cos^2\theta + 3 \qquad (28)$$

where U_0 and W_0 are constants concerned with the binding energies and Q is the quadrupole moment[34,35]. ρ_0 is 3.2 A in this case and ρ_1 and ρ_2 are defined by

$$\rho_1 = \{ l^2 - 2lr\cos\theta + r^2 \}^{1/2}, \quad l/r < \cos\theta < 1,$$

$$\rho_1 = r\sin\theta, \quad l/r > \cos\theta > 0, \qquad (29)$$

$$\rho_2 = \{ r^2 - l^2(3\cos^2\theta - 1)\}^{1/2}$$

where, l and θ are intermolecular paremeters defined in the insert of Fig.32. Lattice sum of eq.(28) is done within a sphere of radius ρ = 33A. Contributions out of the sphere is less than 1 K per molecule. The calculated results are shown in Fig.32 by dash dotted lines. The Van der Waals energy increases about 10K in the α-phase from 0K to $T_{\alpha\beta}$ [36]. The energy in the β-phase show a large temperature dependence reflecting large lattice change[36]. It is noted that the energy of the α-phase at $T_{\alpha\beta}$ is 5K higher than that of the β-phase, so the phase transition at the temperature $T_{\alpha\beta}$ can not be expained by the Van der Waals potential alone.

The magnetic energies in two phases are evaluated by the exchange interactions in these phases and the spin reduction effect is also taken into account. -84 ± 10 K at 0 K for the α-phase and -53 ± 10 K for the β-phase at $T_{\alpha\beta}$ are obtained. Errors in these value mainly come from the ambiguity in the spin reduction.

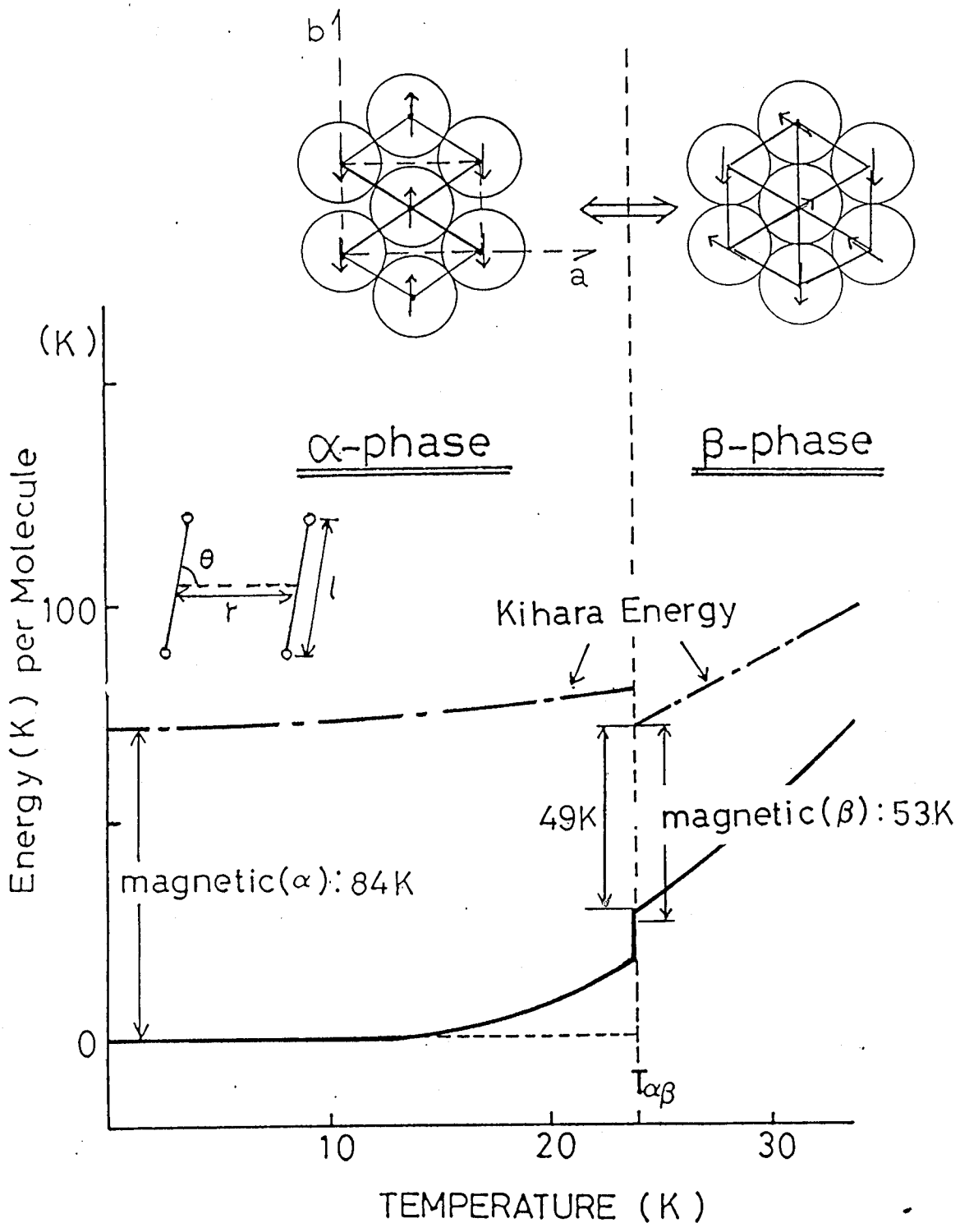

Fig.32. Temperature dependence of the formation energy of solid oxygen in the α- and β-phases.

The temperature dependence of the ground state energy is calculated by integrating the specific heat curve[36] and the results are shown in full lines in Fig.32 . The ground state energy gradually rises about 20 K in the α-phase up to $T_{\alpha\beta}$ and jumps about 20 K there.

Asuming that the gap between Van der Waals energy and the ground state energy at T=0K is equal to the magnetic energy -84 ± 10K, the energy gap at $T_{\alpha\beta}$ is calculated as 84K + 10K - 5K - 20K - 20K = 49K. This value agrees fairly well with the magnetic energy of the β-phase at $T_{\alpha\beta}$,-53 ± 10K. Thus, the ground state energy in α- and β-phases are well understood by considering the van der Waals and magnetic interactions. The result supports the assumption that the phase transition occurs from β- to α-phase in order to change the relatively unstable spin state of the β-phase into the stable 2-sublattice long range order state of the α-phase.

§6. MAGNETO-VOLUME EFFECT IN LIQUID OXYGEN

Equation 27 shows that the value of intermolecular exchange interaction decreases with the molecular distance r. Under an external magnetic field, therefore, r is expected to increase because of the antiferromagnetic repulsion between the magnetically polarized spins. This causes a considerable amount of volume expansion[15]. The effect is expected to reduce the absorption coefficient of the bimolecular transition $2(^3\Sigma_g^-)$ - $2(^1\Delta_g)$, because the volume expantion should reduce J. Details are discussed in §7.

The experimental test of the effect is measured using the static field magnet up to 80kOe. Details of experimental set up are shown in §3-(c). An experimental result of the magneto-volume effect is shown in Fig.33. The liquid volume increases with the magnetic field as is expected. The measured volume change $\Delta V/V_0$ under an increasing field agrees well with the decreasing field value.

The quantitative analysis of the result is done by considering the magnetic field dependence of the O_2-O_2 potential.

As is discussed in §5-(f) the intermolecular potential is written by both the Van der Waals potential and a magnetic energy. The potential U depends on the intermolecular distance r and an external field H_0 and is written as

$$U(r,H_0) = U_0\{(\rho/r)^{12} - 2(\rho/r)^6\} - 2J(r)\langle S_z\rangle^2 \qquad (30)$$

The first term represents the Van der Waals energy and U_0 is the

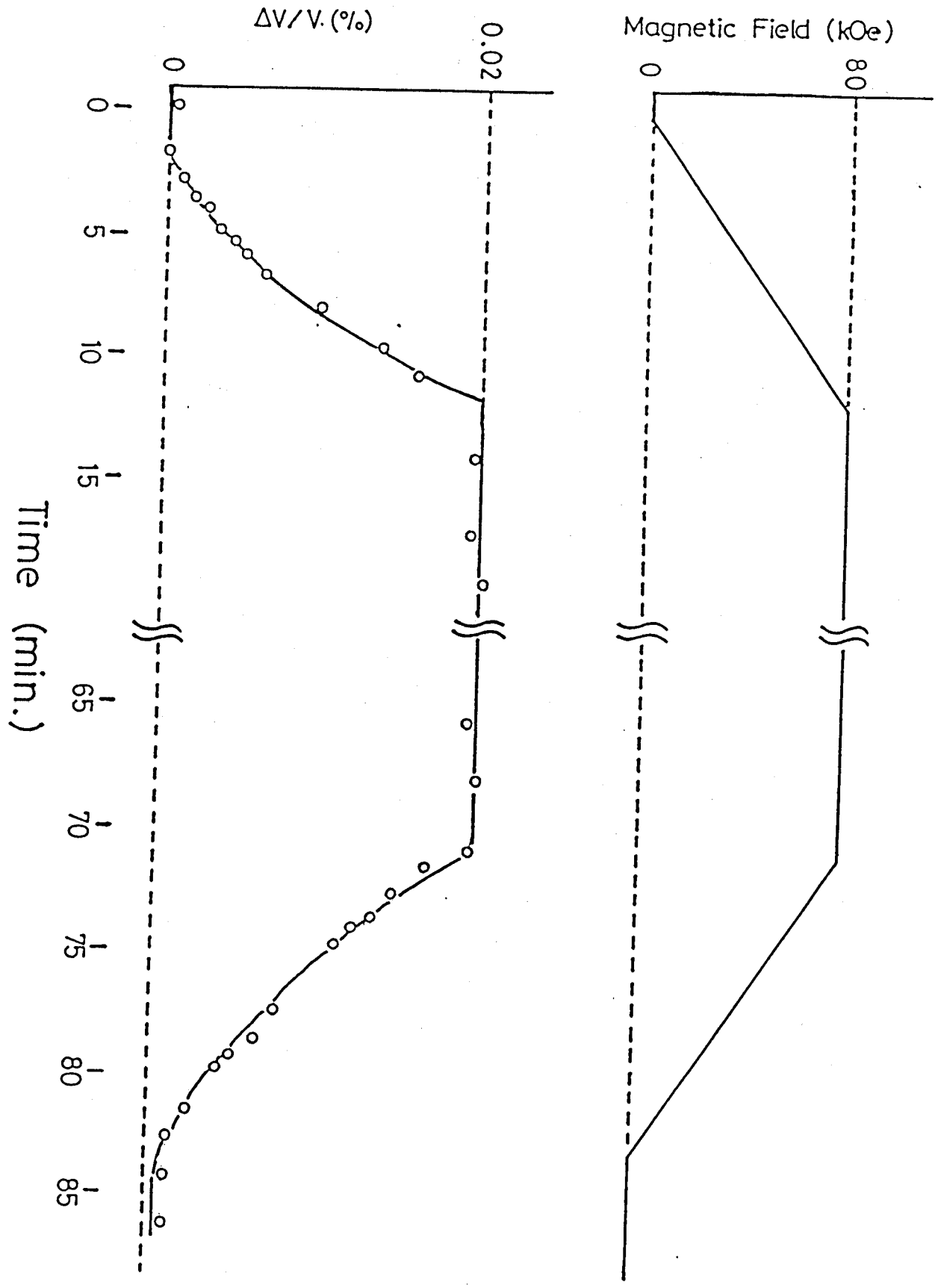

Fig.33 . Rate of volume enhancement and the value of magnetic field as a fuction of time.

zero field energy at the minimum point where the intermolecular distance r is ρ. The parameters U_o and ρ can be evaluated by using the thermal expansion coefficient[37] and liquid density[37] and U_o is between 80 and 120K while ρ is in the range of 3.5~3.9A around 77K. The second term in Eq.(30) shows the exchange energy where $\langle S_z \rangle$ is the mean value of spins under magnetic field. J(r) is the antiferromagnetic intermolecular exchange interaction given in eq.(27). The intermolecular distance $\rho + \Delta r(H_o)$ under magnetic field H_o is obtained from $\partial U/\partial r = 0$ and $\Delta r(H_o)$ is given by

$$\Delta r(H_o) = (J_o \epsilon \rho^2/36U_0)\langle S_z \rangle^2 \exp\{\epsilon(\rho - r_o)\} \qquad (31)$$

$\langle S_z \rangle$ is obtained from the Curie Weiss law as

$$\langle S_z \rangle = 2g\mu_B H_o/3k(T-\Theta), \qquad (32)$$

where the g-value is 2.0 for O_2 molecule and μ_B and k are the Bohr magneton and the Bolzmann constant, respectively. The Curie Weiss constant Θ is -40.6K at 77K[5]. Thus the volume expansion ratio $\Delta V(H_o)/V_o$ is given by

$$\Delta V(H_o)/V_o = 3(\Delta r/\rho) = \beta H_o^2 , \qquad (33)$$

with

$$\beta = (J_o \epsilon \rho/12U_o)[2g\mu_B/3k(T-\Theta)]^2 \exp\{\epsilon(\rho - r_o)\}, \qquad (34)$$

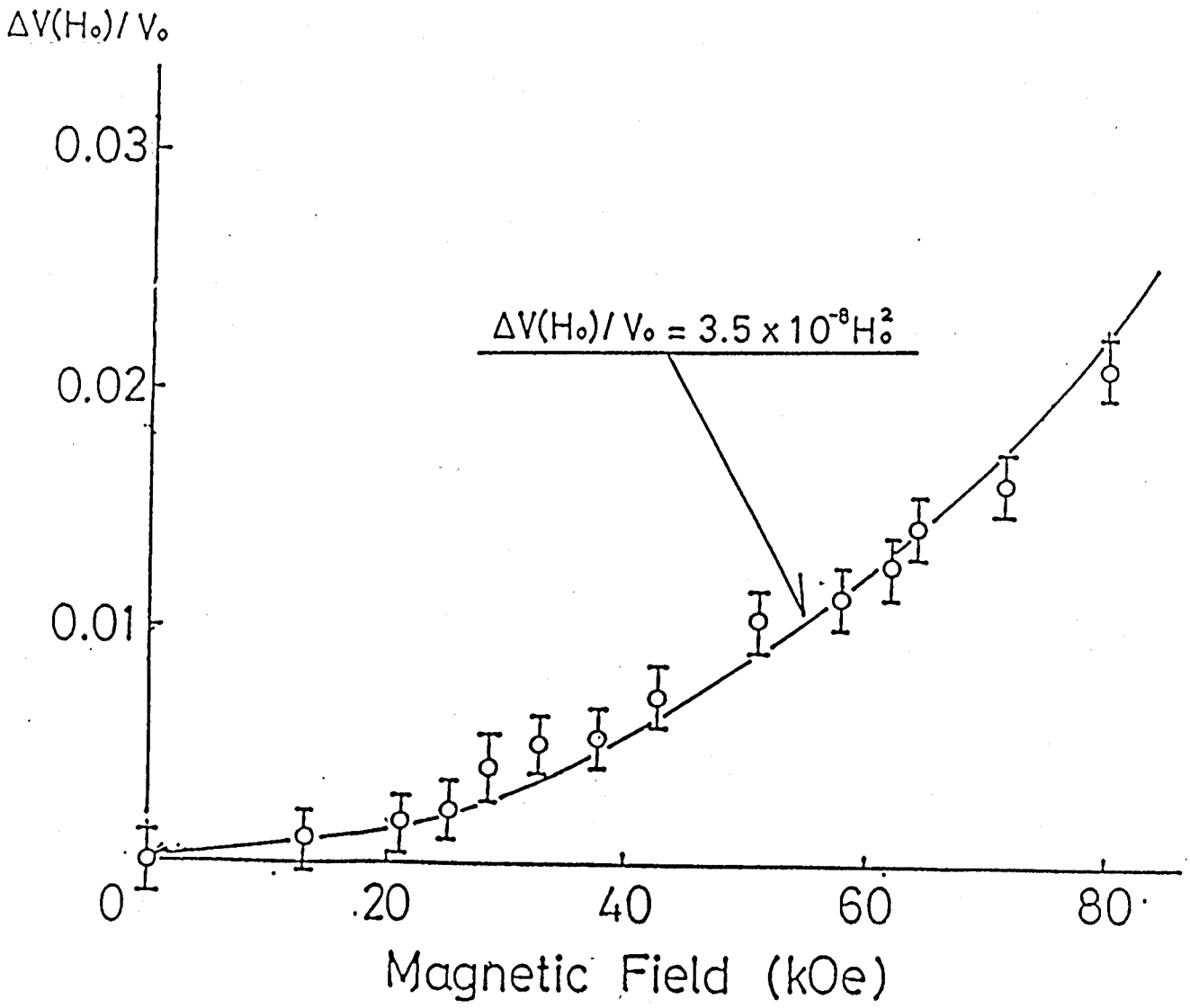

Fig.34 . Magneto-volume effect as a function of field intensity. Open curcles show the observed values of Fig.33. The solid line is written by $\beta=3.5 \times 10^{-8}$ kOe^{-2}

Using values of U_0 and ρ as 100K and 3.7A, respectively, β is evaluated as 2.7 X 10^{-8} kOe^{-2} where ϵ and r_0 are assumed to have value of eq.(27). The experimentally determind β is 3.5 X 10^{-8} kOe^{-2} which shows a fairly good agreement with the calculated value(Fig.34).

It is interesting to compare the observed volume change with those in ferromagnetic Fe, Co and Ni. The magneto-volume increase in Fe, for example, is 4 X 10^{-5} [38] at 80kOe which is much smaller than the value of 2.2 X 10^{-4} in liquid oxygen. This means that liquid oxygen is a unique soft magnetic material with large magneto-volume effect.

§7. FIELD INDUCED TRANCEPARENCY EFFECT IN LIQUID OXYGEN BY HIGH MAGNETIC FIELD

It is shown in §2 that the light blue color of liquid O_2 comes from the bimolecular absorption transition $2(^3\Sigma_g^-) - 2(^1\Delta_g)$. It is noticed that the total spin angular momentum of $2(^1\Delta_g)$ pair should be conserved before and after the photon absorption. As the final state of each molecule is spin singlet, two molecule spins in the ground state should be antiparallel to keep the spin conservation rule. The relation is illustrated in Fig.35. Under a strong magnetic field therefore, the transition will be suppressed because the process becomes forbidden in the spin-polarized liquid. The effect should be temperature dependent since the magnetic susceptibility of liquid O_2 changes with the Curie-Weiss law.

The experimental test of the effect was done by observing the magnetic field dependence of the light absorption in liquid oxygen at the High Magnetic Field Laboratory, Osaka University[16]. Details are given in §3-(b). The whole view of the field dependent absorption spectra is observed using the optical multichannel analyser(OMA) and the result is shown in Fig.36 for λ_1=5760A line. It is clear that the absorption coefficient under external magnetic field of 505kOe is about two thirds of that at H_0=0kOe. On the other hand, monochromatic He-Ne laser is used as light source in order to obtain a quantitative ratio of the reduction of absorption coefficient $\alpha(H_0)/\alpha(0)$ where $\alpha(H_0)$ means the absorption coefficient of light under magnetic field H_0. A typical example of the experimental result is given in Fig.37 and the obtained ratio is

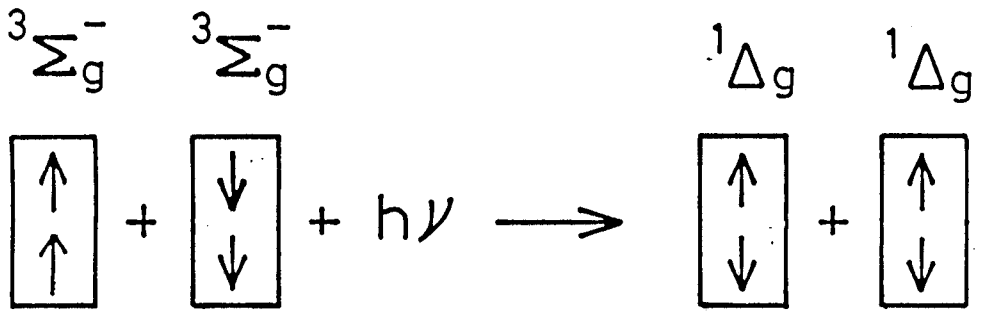

Fig.35 Model of bimolecular transition the one-photon absorption process in O_2 pair. Arrows show spin directions .

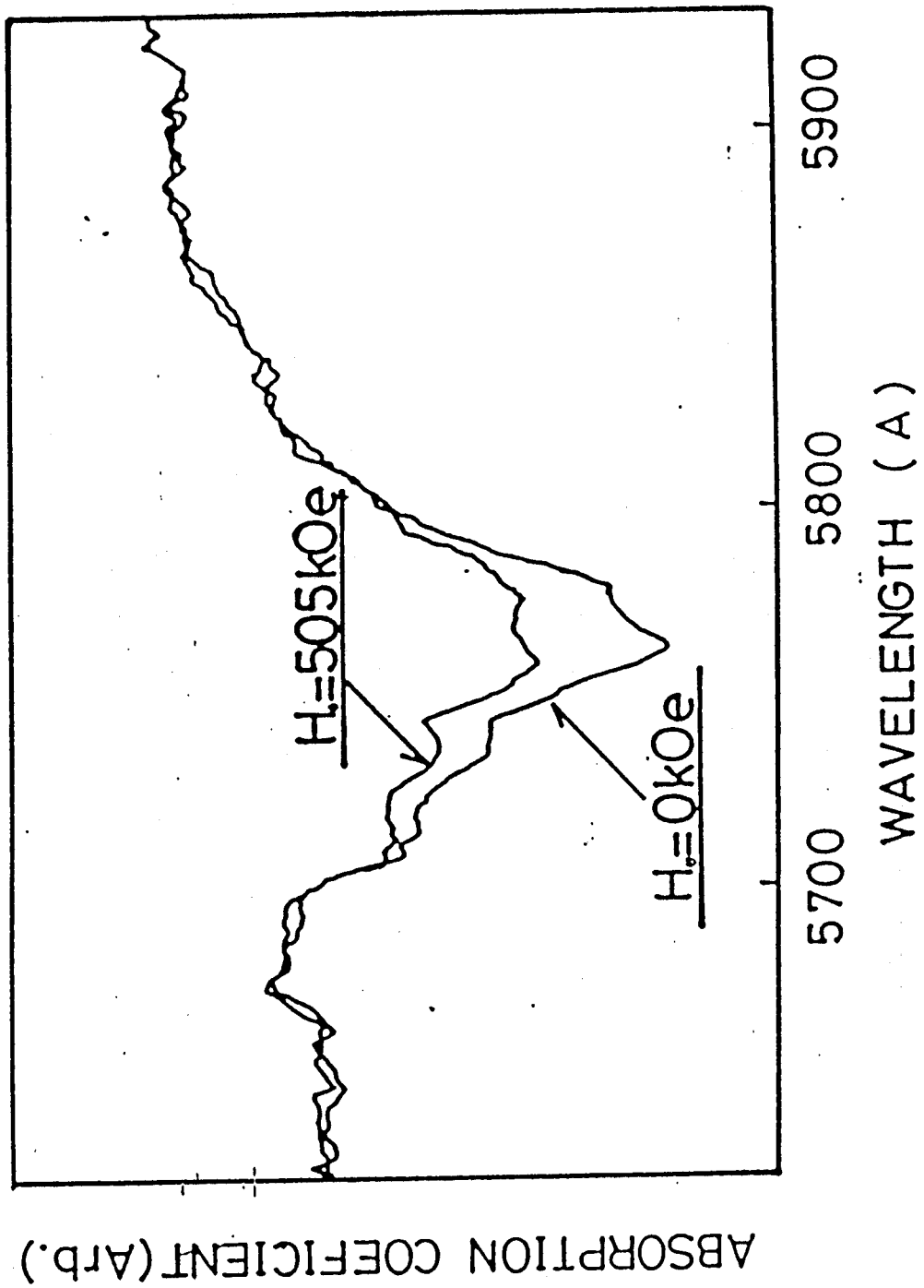

Fig.36 Magnetic field dependence of absorption spectrum.

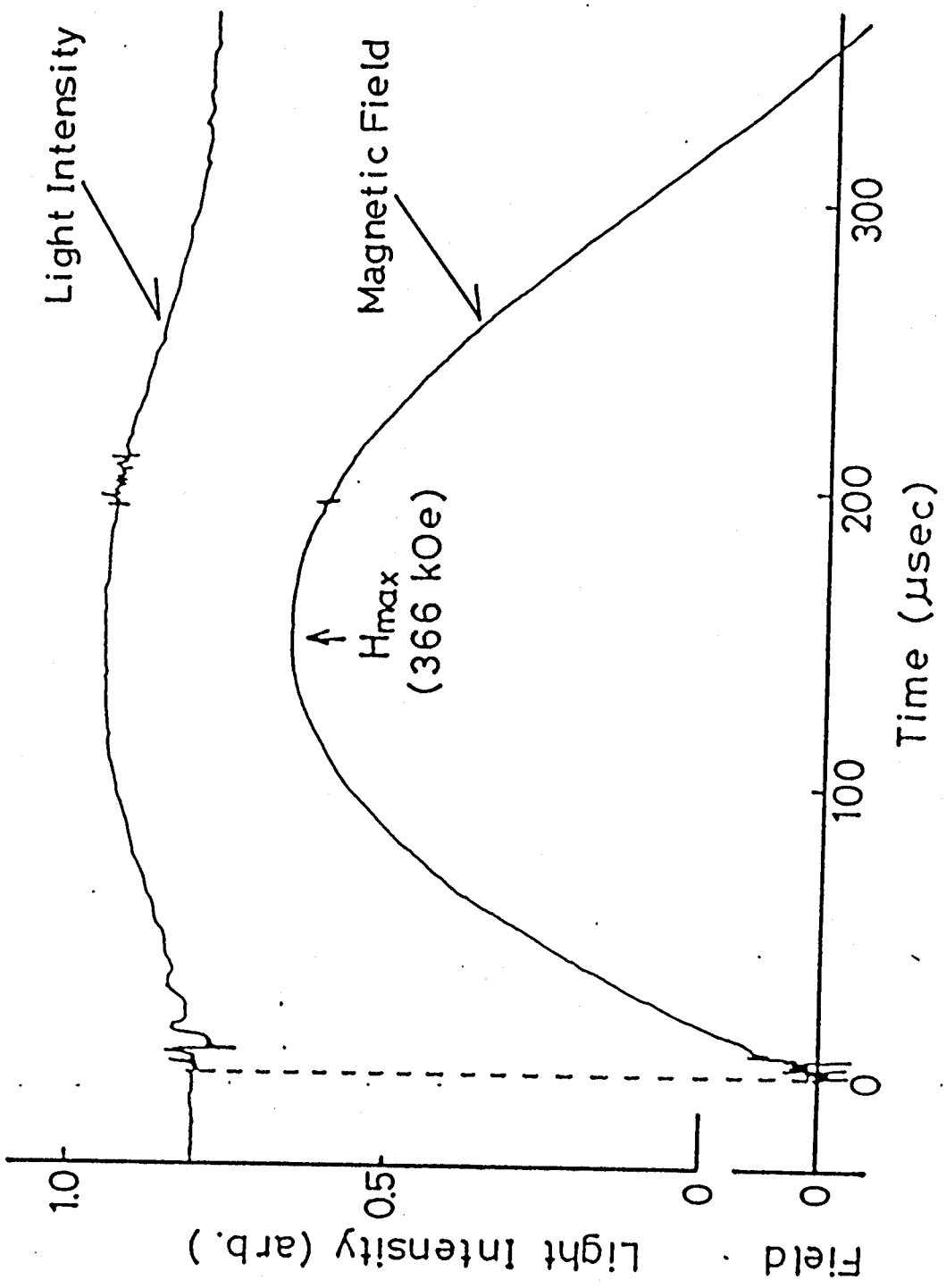

Fig.37 Magnetic field dependence of bimolecular absorption spectrum. The He-Ne laser is used as the light source.

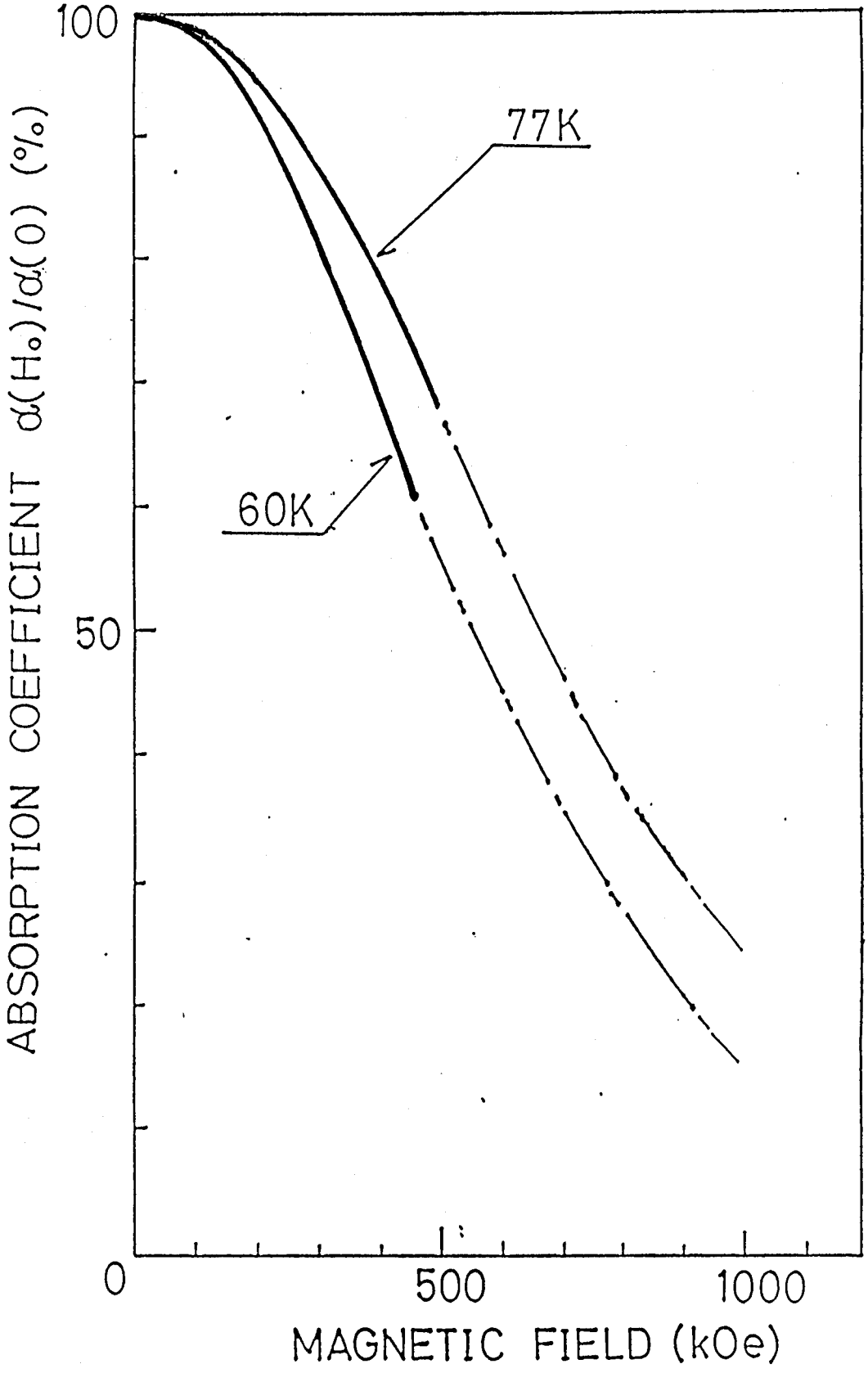

Fig.38 Magnetic field dependence of the normalized absorption coefficient. Broad solid lines show the experimental results. Dash dotted lines show the results of calculation based on spin pair model with J'=-15K.

given in Fig.38 for T=60K and 77K. Thick solid lines show the experimental results. The quantitative analysis of the results are done by evaluating the contribution of the effective exchange interaction on the spin pair and also the magneto-volume effect described in §6.[18] Here the experimentalily obtained absorption coefficient which is observed in values for unit volume $\{\alpha(H_0)/\alpha(0)\}_V$, are transformed to values for unit mass $\{\alpha(H_0)/\alpha(0)\}_M$ in order to exclude the apparent decrease due to density reduction by the magneto-volume effect. $\alpha(H_0)/\alpha(0)$ increases about 1% at 500kOe by this transformation. Details of the calculation is given in APPENDIX III.

First of all, O_2 liquid with no exchange interaction is considered. Under a external magnetic field the ground state with S=1 splits into three levels of m=+1,0 and -1 with population of N_+, N_0 and N_-, respectively. They are calculated as

$$N_+ = Ne^x/(e^x + e^{-x} + 1),$$

$$N_0 = N/(e^x + e^{-x} + 1), \qquad (35)$$

$$N_- = Ne^{-x}/(e^x + e^{-x} + 1),$$

where

$$x = g\mu_B H_0 S/kT. \qquad (36)$$

N is the total number of oxygen molecule per unit mass, and x is

the Zeeman energy normalized by kT. The bimolecular absorption occurs for the pairs of N_+N_- and N_0N_0 because the resultant spin of these pairs are zero. Thus the absorption coefficient $\alpha(H_0)$ per unit mass normalized by the zero field value $\alpha(0)$ is given by

$$\{\alpha(H_0)/\alpha(0)\}_M = \{2N_+(H_0)N_-(H_0)+N_0(H_0)^2\}/\{2N_+(0)N_-(0)+N_0(0)^2\}$$
$$= 9/(e^x + e^{-x} + 1)^2 \qquad (37)$$

Equation (37) is plotted by a dotted line in Fig.39 and 40 for T=60K and T=77K, respectively. The experimental curve is shown in thick solid line for comparison. It is clear that the curve of eq.(37) is too small compared with the experimental results.

Next, the exchange interaction is considered as the correction term in this system. · The exchange term is taken into account in the molecular field manner where x is rewritten as

$$x = (H_0 + 2zJ\langle Sz\rangle/g\mu_B)g\mu_B/kT = g\mu_BH_0/kT + (3/2)(\Theta/T)\langle Sz\rangle \qquad (38)$$

The second term in the braket is the correction due to molecular field. z is the nearest neighbor spin number and the mean value of spin polarization $\langle Sz\rangle$ is calculated as

$$\langle Sz\rangle=(N_+ - N_-)/N= \sinh x/(\cosh x + 1/2) \qquad (39)$$

Inserting eq.(39) in eq.(38), x is numerically calculated for arbitrary H_0 with a relation $\Theta= (2/3)S(S+1)zJ/k=46.5K$. Details

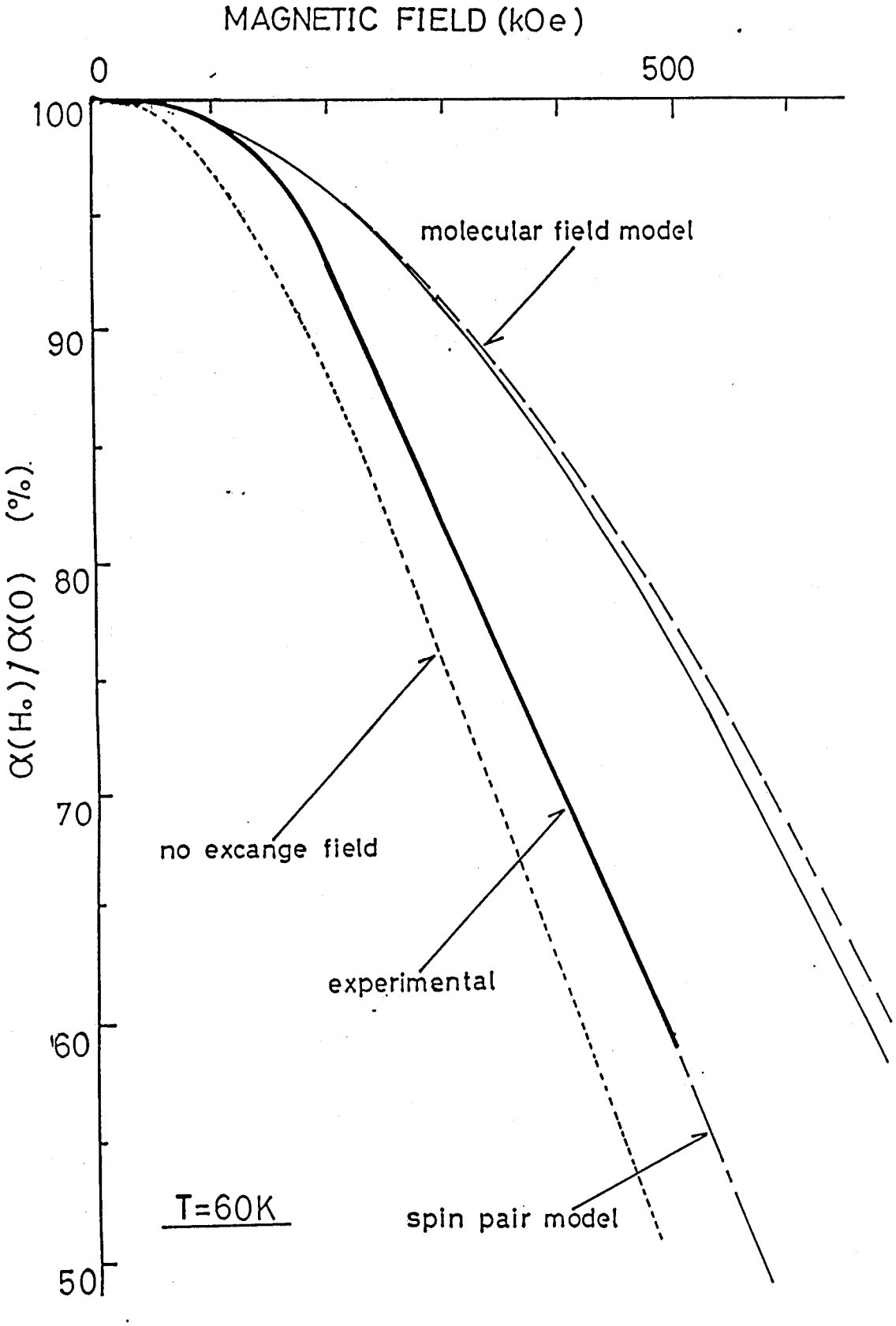

Fig.39 Field dependence of the absorption coefficient for various types of exchange field at T=60K.

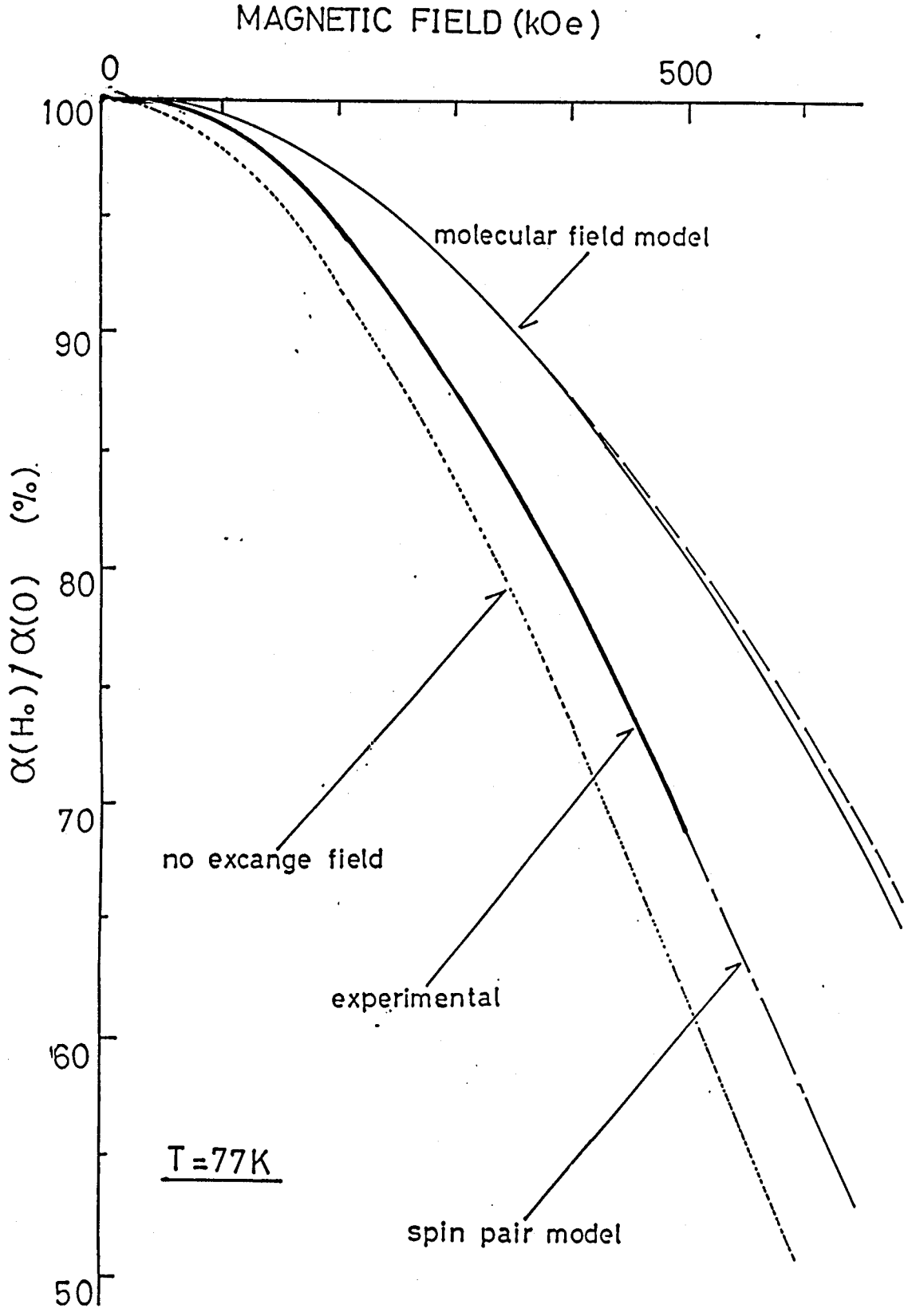

Fig.40 Field dependence of the absorption coefficient for various types of exchange field at T=77K.

are shown in Appendix II. The result is shown in Fig.39 and 40 with a broken line. The obtained value is too large compared with the experimental results for both temperatures T=60K and T=77K. This means that the mean molecular field is too large to account for the experimental results.

As is mentioned in §6, the magneto-volume effect is expected to reduce the discrepancy between the experimental and broken line because the volume expantion reduces the intermolecular exchange interaction J(r). The Curie Weiss constant Θ_H under external magnetic field is obtained from eq.(27) as

$$\Theta_H=[\exp\{\epsilon(\rho+\Delta r(H_0)-r_0)\}/\exp\{\epsilon(\rho-r_0)\}]\,\Theta=\{1+(\epsilon\rho v/3)\langle Sz\rangle^2\}\Theta \tag{40}$$

where v is the ratio of volume expantion obtained from eq.(31)as

$$v=\{\Delta V(H_0)/V_0\}/\langle Sz\rangle^2=3\{\Delta r(H_0)/\rho\}/\langle Sz\rangle^2$$
$$=(J_0\epsilon\rho/12U_0)\exp\{\epsilon(\rho-r_0)\}. \tag{41}$$

Inserting eq.(40) in eq.(38), x is calculated as

$$x=g\mu_B H_0/kT + (3/2)(\Theta/T)\langle Sz\rangle + (3/2)(\Theta/T)(\epsilon\rho v/3)\langle Sz\rangle^3 \tag{42}$$

where the third term is the correction due to volume expantion and the numerically calculated $\{\alpha(H_0)/\alpha(0)\}_M$ is given in solid line in Fig.39 and 40. The reduction of the absorption coefficient due to this change is only about 1% at H_0=500kOe for both T=60K and T=77K, which is far too small to account for the

gap between the experimental and broken line.

Finally, contribution of exchange field is evaluated based on the spin pair model where the antiferromagnetic exchange coupling between the two S=1 spins of the $2(^3\Sigma_g^-)$ states are treated exactly.

The energy levels of the spin pair are calculated by solving the following spin Hamiltonian:

$$\mathcal{H} = -2J' S_1 \cdot S_2 + \mu_B (S_1 + S_2) \cdot \hat{g} \cdot H_0 , \qquad (44)$$

The first and second term represent the exchange and Zeeman energy, respectively. J' is the exchange constant between the two spins of $2(^3\Sigma_g^-)$ pair. S_1 and S_2 are the spin operators for the two spins. Assuming that H_0 is parallel to the z-axis, and that the g tensor $\hat{g}$ is isotopic, the eigen values for eq.(44) is easily solved as

$$\left.\begin{array}{ll} E_{2,-2} = -2J' + 2g\mu_B H_0 & \left.\begin{array}{ll} E_{1,-1} = 2J' + g\mu_B H_0, & \\ E_{1,0} = 2J', & \\ E_{1,1} = 2J' - g\mu_B H_0, & \end{array}\right\} \\ E_{2,-1} = -2J' + g\mu_B H_0, & \\ E_{2,0} = -2J', & \\ E_{2,-1} = -2J' - g\mu_B H_0, & \\ E_{2,-2} = -2J' - 2g\mu_B H_0, & E_{0,0} = 4J', \end{array}\right\} \qquad (45)$$

Details of the calculation are given in Appendix IV . The calculated energy levels are shown in Fig.41 with the definition

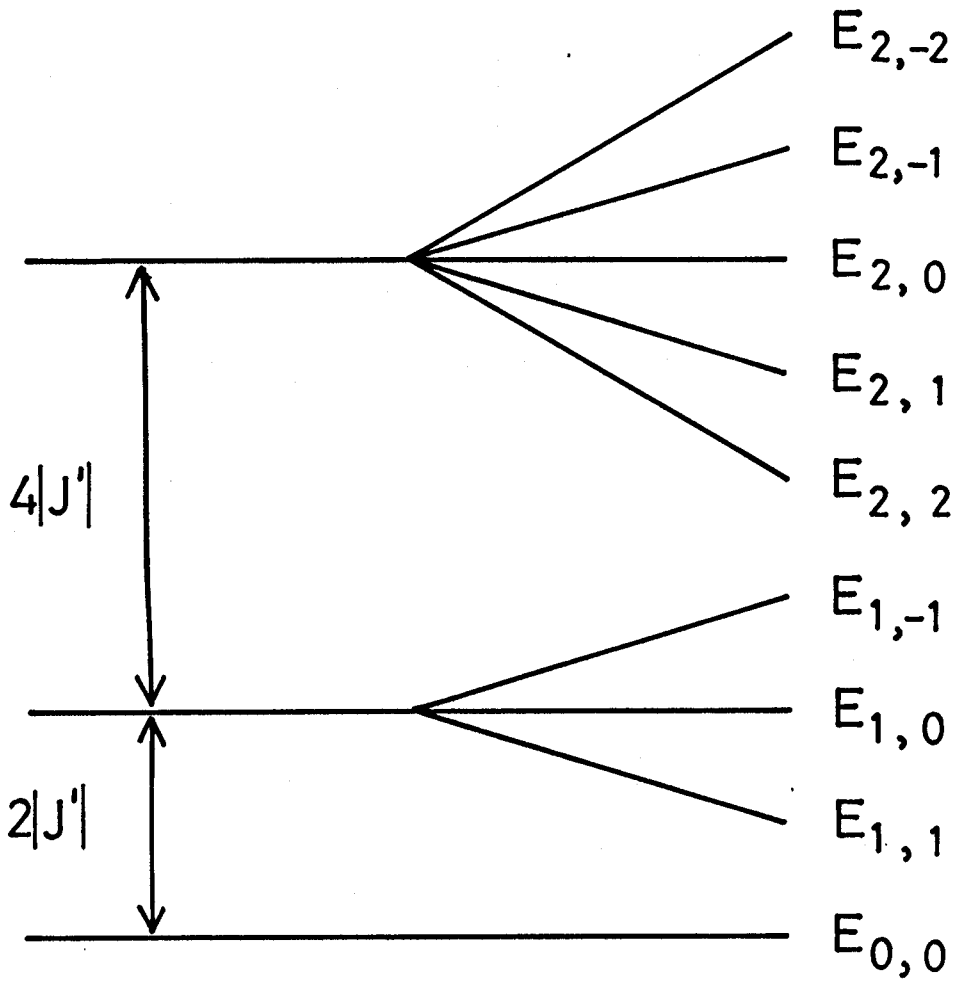

Fig.41 S=1 spin pair energy levels under external magnetic field. $E_{m,n}$ denotes the energy of each level.

of $E_{m,n}$. The wave functions of these levels are

$$\left.\begin{array}{ll}
\psi_{2,-2}=|-1,-1\rangle & \psi_{1,-1}=(1/\sqrt{2})(|0,-1\rangle-|-1,0\rangle) \\
\psi_{2,-1}=(1/\sqrt{2})(|-1,0\rangle+|0,-1\rangle) & \psi_{1,0}=(1/\sqrt{2})(|1,-1\rangle-|-1,1\rangle) \\
\psi_{2,0}=(1/\sqrt{6})(|1,-1\rangle-2|0,0\rangle+|-1,1\rangle) & \psi_{1,1}=(1/\sqrt{2})(|0,1\rangle-|1,0\rangle) \\
\psi_{2,1}=(1/\sqrt{2})(|1,0\rangle+|0,1\rangle) & \\
\psi_{2,2}=|1,1\rangle & \psi_{0,0}=(1/\sqrt{3})(|1,-1\rangle-|0,0\rangle \\
 & \quad +|-1,1\rangle)
\end{array}\right\} \quad (46)$$

The population number for each level is given as

$$\left.\begin{array}{ll}
N_{2,-2} = N_0 e^{-(-6I+2G)}, & N_{1,-1} = N_0 e^{-(-2I+G)} \\
N_{2,-1} = N_0 e^{-(-6I+G)}, & N_{1,0} = N_0 e^{-(-2I)} \\
N_{2,0} = N_0 e^{-(-6I)}, & N_{1,1} = N_0 e^{-(-2I-G)}, \\
N_{2,1} = N_0 e^{-(-6I-G)}, & N_{0,0} = N_0 \\
N_{2,2} = N_0 e^{-(-6I-2G)}, &
\end{array}\right\} \quad (47)$$

where $G=g\mu_B H_0/kT$, $I = J'/kT$ and

$$N_0 = N/\{e^{6I}(2\cosh 2G + 2\cosh G + 1) + e^{2I}(2\cosh G + 1) + 1\}, \quad (48)$$

The bimolecular absorption occurs for level $E_{0,0}$ because the total spin of the $2(^3\Sigma_g^-)$ pair is zero only for this level under external magnetic field. Thus,the absorption coefficient is calculated as

$$\{\alpha(H_0)/\alpha(0)\}_s = N_{0,0}(H_0)/N_{0,0}(0)$$
$$= (5e^{6I} + 3e^{2I} + 1)/\{2(e^{6I} + e^{2I})\cosh G + 2e^{6I}\cosh 2G + 1 + e^{2I} + e^{6I}\} \quad (49)$$

The numerically calculated results of $\{\alpha(H_0)/\alpha(0)\}_s$ with various values of J' is shown in Fig.42 and Fig.43 for T=60K and 77K, respectively. It is found that the experimental result given by a thick line shows a good coincidence with theory when J'=-15K, for both T=60K and 77K. The J' value used here seems to be reasonable because of the following point of view. The used value -15K means that the effective intermolecular distance of optically active pair is 3.36A as is seen from Fig.31. The distance is a little smaller than the molecular distance d_1 of the γ-phase. This fact suggests that the photon absorption occurs with the mean distance of r=3.36A which is smaller than the mean molecular distance of 3.7A in liquid, which is consistent with the scheme of one-photon-two-molecular absorption process.

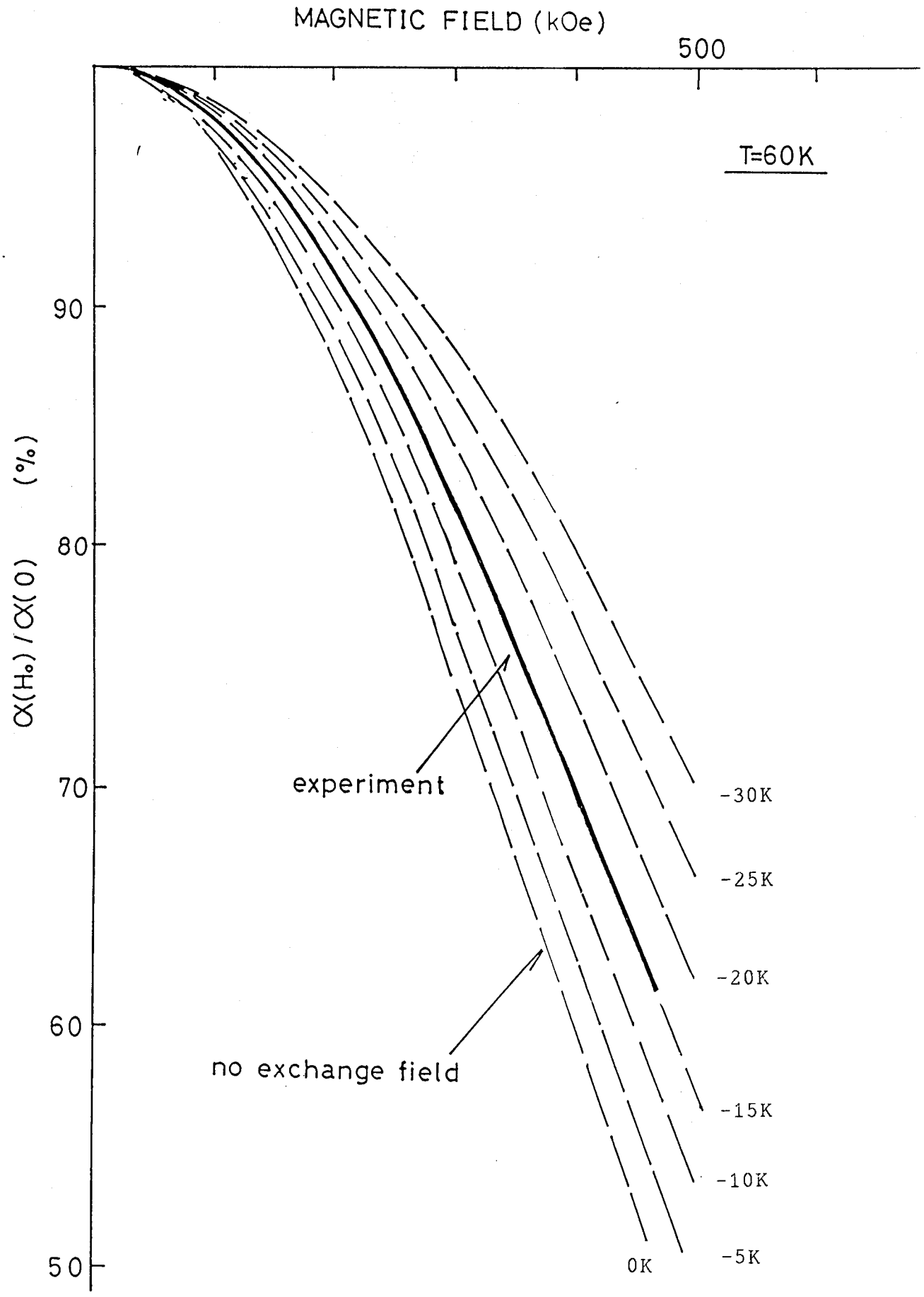

Fig.42 Calculated results of $\alpha(H_0)/\alpha(0)$ based on spin pair model for various values of J'. The temperature is T=60K.

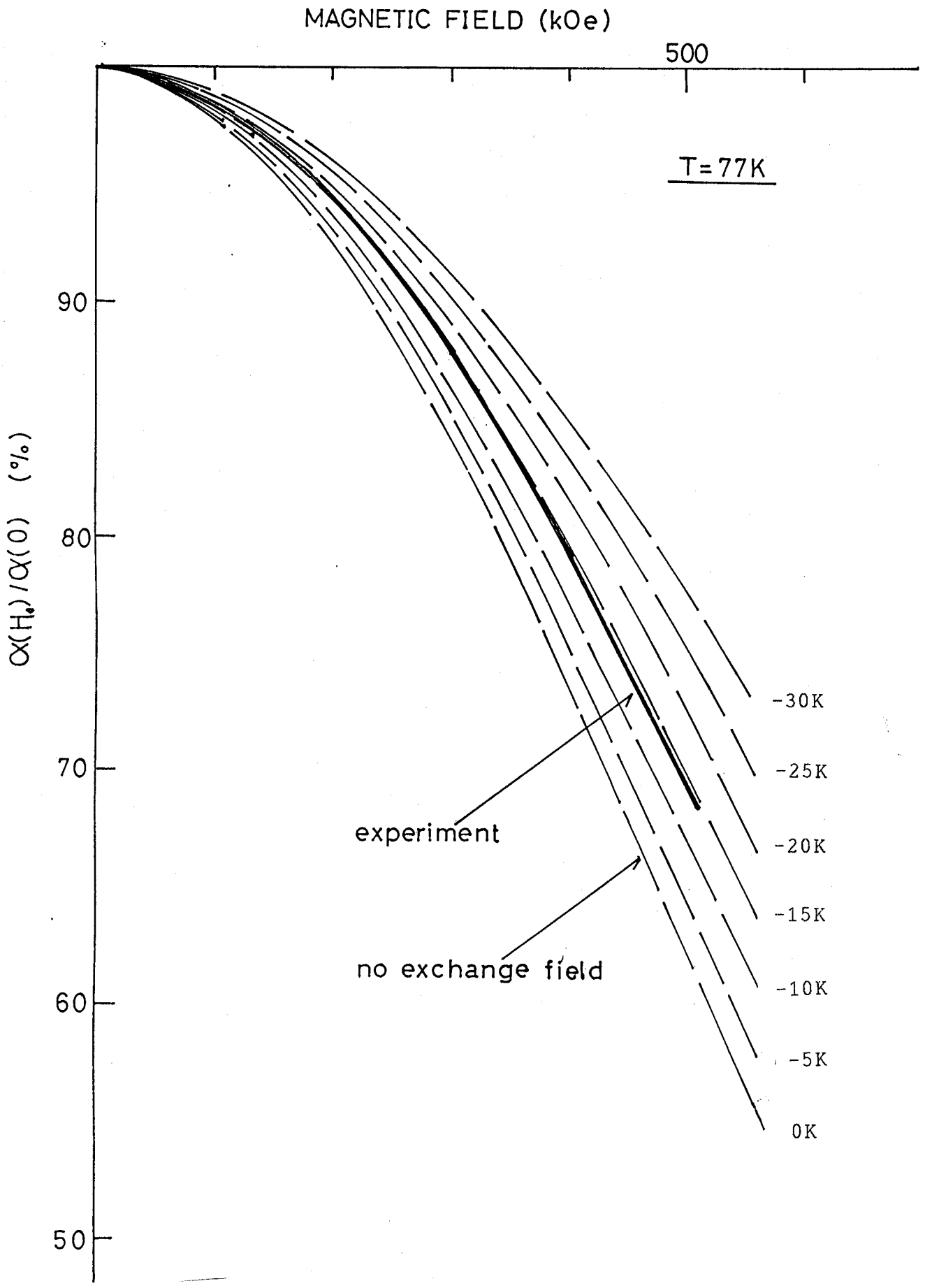

Fig.43 Calculated results of $\alpha(H_0)/\alpha(0)$ based on the spin pair model with various values of J'. The temperature is T=77K.

References

1) P.Curie: Annales de Chimie de Physique 7^{e} serie, t V, (1895).

2) H.Kamerlingh Onnes and A.Perrier: Leiden Comm.139c (1914) 25.

3) G.N.Lewis: J. Am. Chem. Soc. 46 (1924) 2031.

4) E.Kanda, T.Haseda, and A.Ohtsubo: Physica 20 (1954) 131.

5) G.C.Defotis: Phys. Rev. B23 (1981) 4714.

6) T.H.Jordan, W.E.Streib, H.W.Smith and W.N.Lipcomb: Acta. Cryst. 17 (1964) 777.

7) A.E.Curson and A.T.Pawlowitz: Proc. Phys. Soc. London: 85 (1965) 375.

8) C.S.Barrett, L.Meyer and J.Wasserman: J. Chem. Phys. 47 (1967) 592.; C.S.Barrett and L.Mayer: Phys. Rev. 160 (1969) 694.

9) R.J.Meier and R.B.Helmholdt: Phys. Rev. B29 (1984) 1387.

10) T.G.Blocker,M.A.Kinch and F.G.West: Phys.Rev. Letters 22 (1969) 853.

11) E.J.Wachtel and R.G.Wheeler: Phys. Rev. Letters 24 (1970) 233.

12) R.J.Meier, C.J.Schinkel and A.deVisser: J. Phys. C15 (1982) 1015.

13) C.Uyeda, K.Sugiyama and M.Date: J. Phys. Soc. Jpn. 54(1984) 1107.

14) C.Uyeda and M.Date: J. Phys. Soc. Jpn. 55 (1986) 2830.

15) C.Uyeda, A.Yamagishi and M.Date: J. Phys. Soc. Jpn. 56 (1987) 3444

16) C.Uyeda, A.Yamagishi and M.Date: J. Phys. Soc. Jpn. 55 (1986) 468.

17) V.I.Dianov-Klokov: Opt. Spectroscopy 16 (1964) 409.

18) C.Uyeda, A.Yamagishi and M.Date: to be published.

19) For example, G.Herzberg: "Spectra of Diatomic Molecules" van Nostrand (1950)

20) M.L.Klein, D.Levesque and J.J.Weis: Phys. Rev. B21 (1980) 5785.

21) P.W.Stephens, R.J.Birgeneau, C.F.Majkrzak and G.Shirane: Phys. Rev. B28 (1983) 452.

22) A.Yamagishi and M.Date: High Field Magnetism, ed. M.Date, North-Holland Publishing Co. (1983) 289.

23) T.Sakakibara, H.Mollymoto, M.Motokawa and M.Date: ibid. 299.

24) K.Okuda and M.Date: J. Phys. Soc. Jpn. 27 (1969) 839.

25) H.Hori, H.Mollymoto and M.Date: J. Phys. Soc. Jpn. 46 (1979) 908.

26) T.Nagamiya, K.Yoshida and R.Kubo: Advance in Phys. 4 (1955) 1; T.Nagamiya: Prog. Theor. Phys. 11 (1954) 309.

27) V.S.Ostrovskii: Sov. J. Low. Temp. Phys. 9 (1983) 329.

28) R.J.Meier: thesis (Universiteit van Amsterdam, 1984)

29) I.A.Burakhovich, I.N.Krupskii, A.I.Prokhvatilov, Yu.A.Freiman and A.I.Erenburg: JETP Letters 25 (1977) 32.

30) M.E.Lines: J. Phys. Chem. Solids 31 (1970) 101.
J.H.Colpa, E.G.Sieverts and van der Linde: Physics 51 (1971) 573.

31) L.J.De Jongh and A.R.Miedema: Advances in Phys. 23 (1974) 1.

32) R.D.Etters, A.A.Helmy and K.Kobashi: J. Quantum Chem. 17 (1983) 491.

33) J.C.Bonner and M.E.Fisher: Phys. Rev. 135 (1964) A 640.

34) T.Kihara: Rev. Mod. Phys. 25 (1953) 831.

35) T.Kihara and A.Koide: Advances in Chem. Phys. 33 (1975) 51.

36) I.N.Krupskii, A.I.Prophvarilov, Yu.A.Freiman and A.I.Erenburg:

Sov. J. Low Temp. Phys. 5

37) For example, International Critical Tables of Numetrical Data Physics, Chemistry and Technology, ed. E.W.Washburn, McGraw-Hill Book Co. (1926) Vol.1 p102

38) J.L.Snoek: Physica 4 (1937) 853.

ACKNOWLEDGEMENTS

The author wishes to express his sincere gratitude to Professor Muneyuki Date for suggesting this problem and for continuous encouragement and enlighting discussions throughout the present work.

He is indepted to Professor Akio Yamagishi for his cooperation and variable suggestions throughout the experiment of liquid oxygen under high magnetic field.

He is greatful to Professor Mitsuhiro Motokawa of Department of Physics, Faculty of Science, Kobe University for his variable suggestions in the course of analysis.

He would like to thank Professor Hidenobu Hori for the optical measurements using the OMA system. He also would like to thank Dr.Tatsuru Yosida for measurments using the superconducting magnet.

He is greatful to Dr.Kiyohiro Sugiyama for the cooperation and experimental suggestion in the high field magnetization measurementsof solid oxygen.

He wishes to thank Professor Jun Okano of College of General Education for his continuous encouragement in the present problem.

Thanks are also due to the Glass Shop of Osaka University for their prompt and skilful work in making various kinds of sample cells used in the present work.

Finally, the author wishes to thank all the members of the Date laboratory.

APPENDIX I

HYDRO-STATIC DYNAMICS OF LIQUID OXYGEN UNDER HIGH MAGNETIC FIELD

Figure A-1 shows the external field dependence of the O_2 liquid surface inside a capiraly of ϕ6mm. It is clearly seen that the liquid surface is metamorphosed into a coned shape by the external field, which is caused by the balance of demagnetic and gravitational energy. The apical angle of the cone decreases with H_0 and amounts to 30° at maximum field of 80kOe.
This effect is found during the vidual observation of the magneto-volume effect, using the set up of Fig.19.

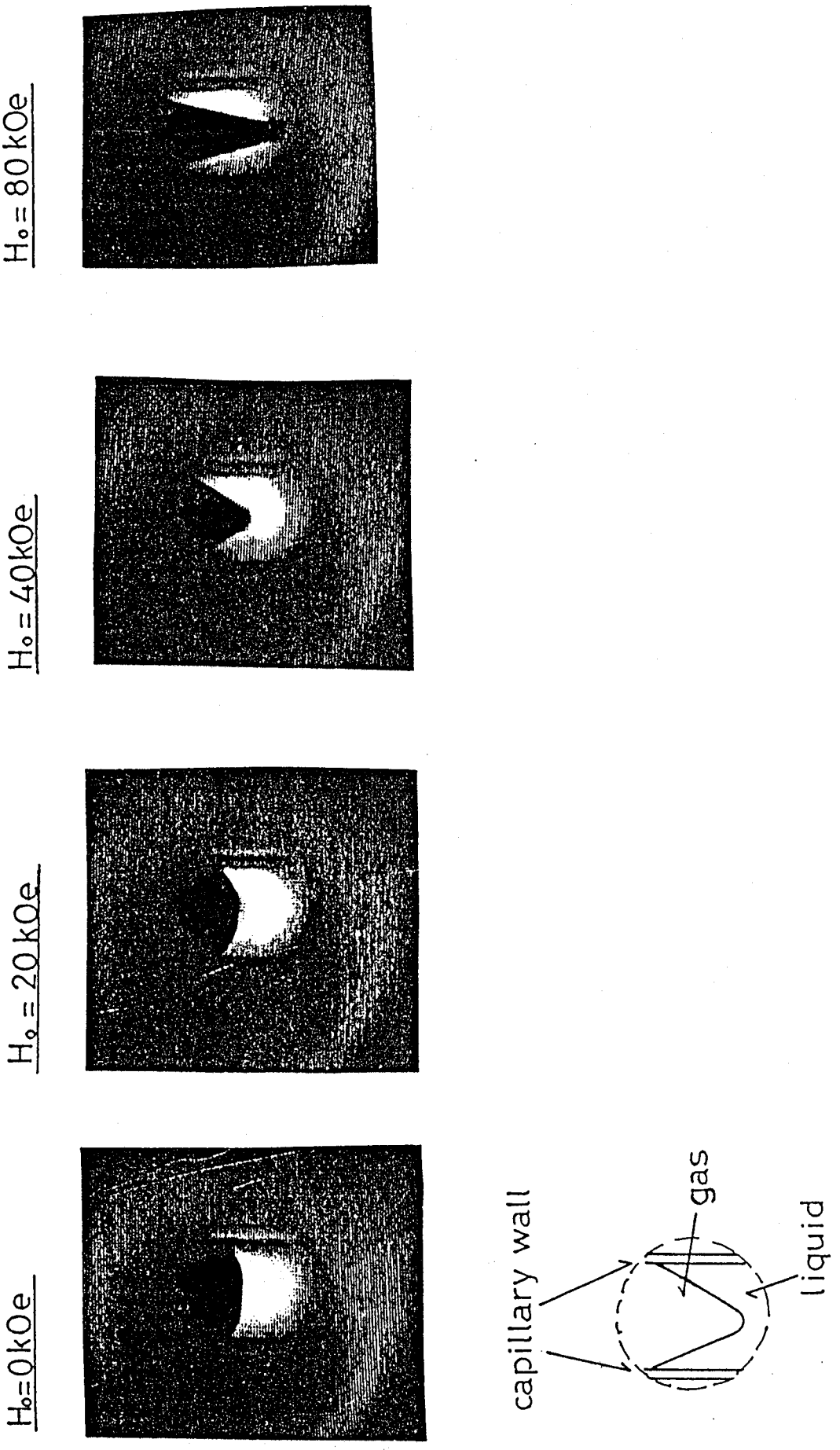

Fig. A-1 Magnetic field dependence of the surface of liquid O_2.

APPENDIX II

CALCULAIONS OF <Sz> AND X IN SECTION 7

The mean value of spin polarization <Sz> and the Zeeman energy x which is normalized by kT are obtained graphically. Figure A-2 shows the relation of <Sz> and x in eqs.(38),(39) and (42) which are shown in solid, dash-dotted and broken lines, respectively. When the magneto-volume effect is neglected in the mean field collection term of x, x and <Sz> are obtained from the intersection of eqs.(38) and (39). The values are listed in Table A-1. When the contribution of the magneto-volume effect is taken into account, x and <Sz> are obtained from the intersections of eqs.(42) and (39). The higher order term $\langle Sz\rangle^3$ in eq.(42) which is the correction term due to magneto-volume effect is substituded with $\{(2/3)x-(1/9)x^3\}^3$. The error due to this substitution is less then 1% when H_0 is around 1000kOe. The values are listed in Table A-2.

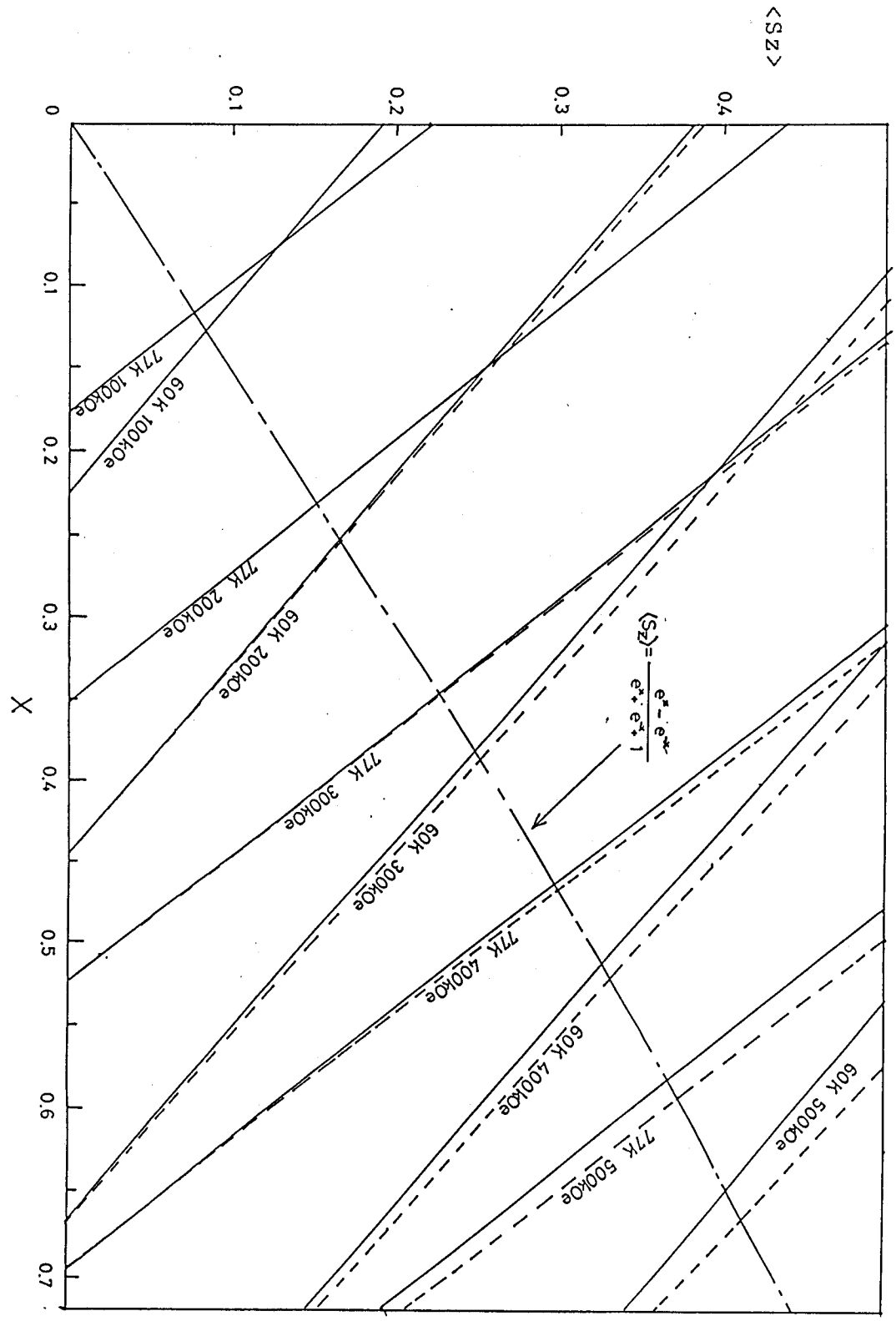

Fig A-2 Relation of <Sz> and x. Equation (39) is written in dash-dotted line. Equations (38) and (42) are written in solid and broken lines, respectively, for various H_0 and T.

Table A-1

H_0	T=60K x	T=60K <Sz>	T=77K x	T=77K <Sz>
0	0	0	0	0
100	.125	.084	.115	.076
200	.253	.166	.229	.151
300	.381	.248	.345	.225
400	.531	.327	.463	.298
500	.647	.403	.583	.368
600	.786	.475	.704	.434
700	.929	.544	.828	.497
800	1.08	.608	.956	.556
900	1.23	.665	1.09	.611
1000	1.27	.718	1.22	.661

Table A-2

H_o	T=60K		T=77K	
	x	<Sz>	x	<Sz>
0	0	0	0	0
100	.126	.084	.115	.076
200	.254	.168	.230	.151
300	.385	.250	.347	.227
400	.521	.332	.467	.301
500	.663	.412	.591	.371
600	.813	.489	.717	.442
700	.97	.562	.851	.508
800	1.13	.629	.988	.570
900	1.30	.688	1.13	.627
1000	1.47	.738	1.27	.677

APPENDIX III

TRANSFROMATION OF $\{\alpha(H_0)/\alpha(0)\}_v$ TO $\{\alpha(H_0)/\alpha(0)\}_M$

The absorption coefficient per unit mass $\{\alpha(H_0)/\alpha(0)\}_M$ is transformed from $\{\alpha(H_0)/\alpha(0)\}_v$, which is the coefficient per unit volume using the following equation.

$$\{\alpha(H_0)/\alpha(0)\}_M=\{1+\Delta V(H_0)/V_0\}\times\{\alpha(H_0)/\alpha(0)\}_v$$
$$=(1+v\langle Sz\rangle^2)\{\alpha(H_0)/\alpha(0)\}_v \qquad (A-1)$$

v is given in eq.(41), and is assumed to be independent with temperature. $\langle Sz\rangle^2$ is obtained from Table A-2. The result is listed in Table A-3.

TABLE A-3

H_0	$\{\alpha(H_0)/\alpha(0)\}_v$	$\{\alpha(H_0)/\alpha(0)\}_M$
T=60K		
0	1.0	1.0
100	.99	.99
200	.92	.92
300	.82	.82
400	.69	.69
500	.58	.59
T=77K		
0	1.0	1.0
100	.99	.99
200	.94	.94
300	.88	.88
400	.78	.78
500	.68	.69

APPENDIX IV

CALCULATION OF THE ENERGY LEVELS OF FIGURE 41

The matrix elements of eq.(44) is calculated in Table A-7.

Table A-7

	$\|1, 1\rangle$	$\|1, 0\rangle$	$\|1,-1\rangle$	$\|0, 1\rangle$	$\|0, 0\rangle$	$\|0,-1\rangle$	$\|-1, 1\rangle$	$\|-1, 0\rangle$	$\|-1,-1\rangle$
$\|1, 1\rangle$	-2J+2G								
$\|1, 0\rangle$		G		-2J'					
$\|1,-1\rangle$			2J'		-2J'				
$\|0, 1\rangle$		-2J'		G					
$\|0, 0\rangle$			-2J'				-2J'		
$\|0,-1\rangle$						-G		-2J'	
$\|-1, 1\rangle$					-2J'		-2J'		
$\|-1, 0\rangle$						-2J'		-G	
$\|-1,-1\rangle$									2J'-2G

Table A-7 is diagonalized as,

Table A-8

	$\psi_{2,2}$	$\psi_{2,1}$	$\psi_{2,0}$	$\psi_{2,-1}$	$\psi_{2,-2}$	$\psi_{1,1}$	$\psi_{1,0}$	$\psi_{1,-1}$	$\psi_{0,0}$
$\psi_{2,2}$	-2J'+2G								
$\psi_{2,1}$		-2J'+G							
$\psi_{2,0}$			-2J'						
$\psi_{2,-1}$				-2J'-G					
$\psi_{2,-2}$					-2J'-2G				
$\psi_{1,1}$						2J'+G			
$\psi_{1,0}$							2J'		
$\psi_{1,-1}$								2J'-G	
$\psi_{0,0}$									4J'

LISTS FOR COMPUTER CALCULATION PROGRAMS

LIST 1 Program for the polycrystalline antiferromagnetic magnetization curve. (Fig.21)

```
 20 CLS 3
 30 HC=SQR(2*K1/X):LINE(100,10)-(600,180),3,B:LINE(300,10)-(300,180).
 40 LINE(100,80)-(600,80),2
 50 FOR I=1    TO 200
 60 H=I*HC/100
 70 FOR J=0 TO 8
 80 TH=J*3.1416/18+.5*3.1416/18
 90 FOR W=0 TO 8
 91 PH=W*3.1416/18+.5*3.1416/18
100 KA=2*K1/(X*H^2):KB=2*K2/(X*H^2)
120 AH=SIN(TH)*COS(PH):BH=SIN(TH)*SIN(PH):CH=COS(TH)
140 P=KA+KB+1:Q=(KA+KB)*AH^2+KB*BH^2+KA*CH^2+KA*KB:R=KA*KB*AH^2
160 L=R/Q:LL=0
180 FF=L^3-P*L^2+Q*L-R:DF=3*L^2-2*P*L+Q
182 LS=LL-L
200 IF ABS(LS)<.001 GOTO 240
210 LL=L
220 L=L-FF/DF:GOTO 180
240 A=AH^2-L:B=AH*BH:C=AH*CH:D=BH^2+KA-L:E=BH*CH:F=CH^2+KB-L
260 BO=1/(((B*E-D*C)/(A*E-B*C))^2+((D*C-B*E)/(C*E-F*B))^2+1)
280 CO=((D*C-B*E)/(E*C-F*B))^2*BO
300 DO= 1+KA*BO+KB*CO-L:M=H*X*DO*SIN(TH)*(3.1416/18)^2*2/3.14
320 MS=MS+M
330 NEXT W
340 NEXT J
350 Y=(MS-TS)*100/HC:PSET(I*2+100,180-Y*100/X)
360 TS=MS:MS=0:PRINT Y
370 NEXT I
380 STOP
```

LIST 2 Program for calculating the dipolar anisotropy field of α-O_2 (Fig.29)

Notes: The total lattice sum is obtained by the summention of the result of (a) and (b) for various internuclear distances. The temperature is asuumed to be T=OK, and the lattice constants a,b,c and β are inserted in A,B,C and D of line 20.The internuclear distance is inserted in V.

(a) Sum over the same sublattice

```
20 A=5.403:B=3.429:C=5.086:D=47.47:UX=0:UY=0:UZ=0:W=0:V=1.9:UP=0:UO=0
30 R=A
40 G=D*3.14159/180:E=SIN(G):F=COS(G)
50 H=INT(R/(A*E))+1:I=INT(R/(C*E))+1:J=INT(R/B)+1
51 PRINT  H;I;J
60 L=-H-1:M=-I:N=-J
80 IF L^2+M^2+N^2=0 GOTO 130
90 Q=SQR((L*A+M*C*F)^2+(M*C*E+V)^2+(N*B)^2)
95 IF Q>R  GOTO 130
100 X=(1-3*((L*A+M*C*F)/Q)^2)/Q^3
101 Y=(1-3*((M*C*E+V)/Q)^2)/Q^3
102 Z=(1-3*(N*B/Q)^2)/Q^3
103 P=-3*(L*A+M*C*F)*(N*B)/Q^5
104 O=-3*(L*A+M*C*F)*(M*C*E+V)/Q^5
110 SX=SX+X:SY=SY+Y:SZ=SZ+Z:SP=SP+P :SO=SO+O
120 W=W+1
130 L=L+1
140 IF  L>H GOTO 150 ELSE 80
150 M=M+1:L=-H
160 IF M>I GOTO 170 ELSE 80
170 N=N+1:M=-I
180 IF N>J GOTO 190 ELSE 80
190 TX=SX-UX:TY=SY-UY:TZ=SZ-UZ:TP=SP-UP:IO=SO-UO
200 PRINT TAB(1);R;TAB(10);W;TAB(20);SX;TAB(30);SY;TAB(40);SZ:TAB(50):TX
:TY;TAB(70);TZ
201 PRINT SP;TAB(20);TP;TAB(40);SO;TAB(20);IO
210 UX=SX:UY=SY:UZ=SZ:UP=SP:UO=SO
211 SX=0:SY=0:SZ=0:SP=0:SO=0
220 R=R+A:W=0
230 IF R<6*A GOTO 40
240 STOP
250 END
```

(b) Sum over the adjacent sublattice

```
20 A=5.403:B=3.429:C=5:086:D=47.47:UX=0:UY=0:UZ=0:W=0:V=1.9:UP=0:UO=0
30 R=A
40 G=D*3.14159/180:E=SIN(G):F=COS(G)
50 H=INT(R/(A*E))+1:I=INT(R/(C*E))+1:J=INT(R/B)+1
51 PRINT  H;I;J
60 L=-H-1/2:M=-I:N=-J-1/2
80 IF L^2+M^2+N^2=0 GOTO 130
90 Q=SQR((L*A+M*C*F)^2+(M*C*E+V)^2+(N*B)^2)
95 IF Q>R  GOTO 130
100 X=(1-3*((L*A+M*C*F)/Q)^2)/Q^3
101 Y=(1-3*((M*C*E+V)/Q)^2)/Q^3
102 Z=(1-3*(N*B/Q)^2)/Q^3
103 P=-3*(L*A+M*C*F)*(N*B)/Q^5
104 O=-3*(L*A+M*C*F)*(M*C*E+V)/Q^5
110 SX=SX+X:SY=SY+Y:SZ=SZ+Z:SP=SP+P :SO=SO+O
120 W=W+1
130 L=L+1
140 IF  L>H GOTO 150 ELSE 80
150 M=M+1:L=-H-1/2
160 IF M>I GOTO 170 ELSE 80
170 N=N+1:M=-I
180 IF N>J GOTO 190 ELSE 80
190 TX=SX-UX:TY=SY-UY:TZ=SZ-UZ:TP=SP-UP:IO=SO-UO
200 PRINT TAB(1);R;TAB(10);W;TAB(20);SX;TAB(30);SY;TAB(40);SZ;TAB(50);TX
;TY;TAB(70);TZ
201 PRINT SP;TAB(20);TP;TAB(40);SO;TAB(20);IO
210 UX=SX:UY=SY:UZ=SZ:UP=SP:UO=SO
211 SX=0:SY=0:SZ=0:SP=0:SO=0
220 R=R+A:W=0
230 IF R<6*A GOTO 40
240 STOP
250 END
```

LIST 3 Program for calculating the formation energy of α- and β-O_2

Notes: The lattice constants at various temperatures are reffered from refference 36 and inserted in A,B,C and D of line 20 in (a) and (b). A,B,C and D corespond to constants a,b c and β of Fig.6, respectively. Thetotal lattice sum is obtained by the summention of the results of (a) and (b) for each temperature. Theresults are shown in broken lines in Fig.30.

(a) Sum over the same sublattice.

```
20 A=5.403:B=3.429:C=5.086:D=47.47:UX=0:UY=0:UZ=0:W=0:V=0 :UP=0
30 R=A
40 G=D*3.14159/180:E=SIN(G):F=COS(G)
50 H=INT(R/(A*E))+1:I=INT(R/(C*E))+1:J=INT(R/B)+1
51 PRINT  H;I;J
60 L=-H-1/2:M=-I:N=-J-1/2
80 IF L^2+M^2+N^2=0 GOTO 130
90 Q=SQR((L*A+M*C*F)^2+(M*C*E-V)^2+(N*B)^2)
95 IF Q>R  GOTO 130
101 Y=(1-3*((M*C*E-V)/Q)^2)/Q^3
103 P=-1/Q^6
110 SP=SP+P
120 W=W+1
130 L=L+1
140 IF  L>H GOTO 150 ELSE 80
150 M=M+1:L=-H-1/2
160 IF M>I GOTO 170 ELSE 80
170 N=N+1:M=-I
180 IF N>J GOTO 190 ELSE 80
190 TP=SP-UP
201 PRINT SP;TAB(20);TP
210 UP=SP
211 SP=0
220 R=R+A:W=0
230 IF R<6*A GOTO 40
240 STOP
```

(b) Sum over the differrent sublattice.

```
20 A=5.4:B=3.43:C=5.09:D=47.47:UX=0:UY=0:UZ=0:W=0 :UP=0
30 R=A
40 G=D*3.14159/180:E=SIN(G):F=COS(G)
50 H=INT(R/(A*E))+1:I=INT(R/(C*E))+1:J=INT(R/B)+1
51 PRINT  H;I;J
60 L=-H:M=-I:N=-J
80 IF L^2+M^2+N^2=0 GOTO 130
90 Q=SQR((L*A+M*C*F)^2+(M*C*E)^2+(N*B)^2)
95 IF Q>R  GOTO 130
103 P=-1/Q^6
110 SP=SP+P
120 W=W+1
130 L=L+1
140 IF  L>H GOTO 150 ELSE 80
150 M=M+1:L=-H
160 IF M>I GOTO 170 ELSE 80
170 N=N+1:M=-I
180 IF N>J GOTO 190 ELSE 80
190 TP=SP-UP
201 PRINT SP;TAB(20);TP
210 UP=SP
211 SP=0
220 R=R+A:W=0
230 IF R<120 GOTO 40
240 STOP
250 END
```